

Non-Parametric Cell-Based Photometric Proxies for Galaxy Morphology: Methodology and Application to the Morphologically-Defined Star Formation – Stellar Mass Relation of Spiral Galaxies in the Local Universe

M. W. Grootes^{1*}, R. J. Tuffs¹, C. C. Popescu², A. S. G. Robotham^{3,4}, M. Seibert⁵, L. S. Kelvin^{3,4,6}

¹Max-Planck Institut für Kernphysik, Saupfercheckweg 1, 69117 Heidelberg, Germany

²Jeremiah Horrocks Institute, University of Central Lancashire, Preston PR1 2HE, UK

³ICRAR, The University of Western Australia, 35 Stirling Highway, Crawley, WA 6009, Australia

⁴SUPA School of Physics & Astronomy, University of St. Andrews, North Haugh, St. Andrews KY16 9SS, UK

⁵Observatories of the Carnegie Institution for Science, 813 Santa Barbara Street, Pasadena, CA 91101, USA

⁶Institut für Astro- und Teilchenphysik, Universität Innsbruck, Technikerstrasse 25, 6020 Innsbruck, Austria

Accepted ??? Received ???; in original form ???

ABSTRACT

We present a non-parametric cell-based method of selecting highly pure and largely complete samples of spiral galaxies using photometric and structural parameters as provided by standard photometric pipelines and simple shape fitting algorithms. The performance of the method is quantified for different parameter combinations, using purely human-based classifications as a benchmark. The discretization of the parameter space allows a markedly superior selection than commonly used proxies relying on a fixed curve or surface of separation. Moreover, we find structural parameters derived using passbands longwards of the g band and linked to older stellar populations, especially the stellar mass surface density μ_* and the r band effective radius r_e , to perform at least equally well as parameters more traditionally linked to the identification of spirals by means of their young stellar populations, e.g. UV/optical colours. In particular the distinct bimodality in the parameter μ_* , consistent with expectations of different evolutionary paths for spirals and ellipticals, represents an often overlooked yet powerful parameter in differentiating between spiral and non-spiral/elliptical galaxies. We use the cell-based method for the optical parameter set including r_e in combination with the Sérsic index n and the i -band magnitude to investigate the intrinsic specific star-formation rate - stellar mass relation ($\psi_* - M_*$) for a morphologically defined volume limited sample of local universe spiral galaxies. The relation is found to be well described by $\psi_* \propto M_*^{-0.5}$ over the range of $10^{9.5}M_\odot \leq M_* \leq 10^{11}M_\odot$ with a mean interquartile range of 0.4 dex. This is somewhat steeper than previous determinations based on colour-selected samples of star-forming galaxies, primarily due to the inclusion in the sample of red quiescent disks.

Key words: galaxies:fundamental parameters – galaxies:spiral – galaxies:structure – galaxies:photometry.

1 INTRODUCTION

With the advent of large optical photometric ground and space-based surveys which are ongoing, commencing (The Sloan Digital Sky Survey (SDSS; York et al. 2000; Abazajian et al. 2009, The Galaxy And Mass Assembly Survey

(GAMA; Driver et al. 2011), SKYMAPPER (Keller et al. 2007), The VST Atlas, The Kilo Degree Survey (KiDS; de Jong et al. 2012), The Dark Energy Survey (DES; The DES collaboration 2005)) or scheduled to commence in the next years (e.g., EUCLID; Laureijs et al. 2011), the number of extragalactic sources with reliable, uniform data is increasing dramatically, further opening the door to statistical studies of the population of galaxies, both at

* E-mail: meiert.grootes@mpi-hd.mpg.de

local and intermediate redshifts.

To first order, the visible matter distributions of galaxies may be classified as being best described either as an exponential disk, i.e. a largely rotationally-supported system, or a spheroid, i.e. a largely pressure-supported system. This dichotomy forms the basis of the standard morphological categorization of galaxies into late-types/spirals and early-types/ellipticals, introduced by Hubble (1926) and in widespread use ever since. This basic morphological bimodality of the galaxy population appears to be mirrored in a range of physical properties, with late-type/spiral galaxies having blue UV/optical colours and showing evidence of star formation, on average, while early-type/elliptical galaxies appear red on average, and mostly only display a low level of star formation, if any at all (e.g. Strateva et al. 2001; Baldry et al. 2004; Balogh et al. 2004). However, a wide variety of exceptions to this rule exist. For example, spiral galaxies may appear red due to the attenuation of their emission by dust in their disks, or a spiral may truly have very low star formation and red colours whilst maintaining its morphological identity, while, on the other hand, an elliptical galaxy may appear blue due to a localized recent burst of star-formation.

It is assumed that different modes of assembly of the stellar populations of these galaxy categories are responsible for the distinction. This in turn, necessitates the ability to reliably identify and distinguish between the types of galaxies when investigating the physical processes determining galaxy formation and evolution on the basis of large statistical samples of galaxies. Furthermore, it is clear that in any investigation of galaxy properties for a given morphological class, the classification itself should not introduce a bias into the property being investigated. For example, a pure sample of spiral galaxies used to investigate star-formation as a function of galaxy environment must include the population of red, passively star-forming spiral galaxies.

Visual classifications of galaxy morphology by professional astronomers therefore remain the method of choice and the benchmark for robustly identifying the morphology of a galaxy. However, such classifications may suffer from biases arising from the individual performing the classification, and the uncertainty/robustness of the classification is difficult to quantify. Furthermore, in the case of marginally resolved data, even the ability of the human eye to identify morphological structure may be limited, so that the decreasing linear resolution as a function of redshift may introduce systematic biases. In such cases, quantitative photometric measures of the light-profile may be at least as reliable as human classifications. The overriding fact which immediately stymies the visual classification by professionals of all sources in modern imaging surveys such as SDSS, however, is the size of the galaxy samples provided by the surveys, and accordingly the time required for classification. Thus, one is forced to develop alternative schemes for obtaining morphological classifications of large samples of galaxies.

Recently, in an attempt to circumvent the limitations in sample size, reduce the possibility of bias, and provide an objective measure of robustness, Lintott et al. (2008) have enlisted the help of 'citizen scientists in visually classifying a large fraction of SDSS DR7 galaxies in the GALAXY ZOO project (Lintott et al. 2008, 2011), releasing a catalogue

of probability-weighted visual classifications into spirals and ellipticals. Although demonstrably feasible, such an approach is nevertheless very time consuming, especially on large data-sets.

The often adopted alternative is to attempt an automatic classification of galaxies based on some proxy for a galaxy's morphology. These automatic classification schemes can be roughly divided into three categories: i) those relying on a detailed analysis of the full imaging products, ii) those using a wide variety of photometric and spectroscopic proxies, in combination with a sophisticated algorithmic decision process, and iii) those using one or two simple, usually photometric, parameters and a fixed or simply parameterized separator. Of course, hybrids between these categories also exist.

Examples of the first category include the Concentration, Asymmetry, and Clumpiness (CAS, Conselice 2003) parameters, derived directly from the data reduction and model fitting of the imaging data, as well as the Gini coefficient (Gini 1912; Abraham, van den Bergh & Nair 2003; Lotz, Primack, & Madau 2004) and the M_{20} coefficient (Lotz, Primack, & Madau 2004). Forming a hybrid between this and the second category, Scarlata et al. (2007) have introduced the *Zurich Estimator of Structural Types (ZEST)* based on a principle component analysis of these and other model-independent quantities, which has been applied to various data sets. Examples of the second category are given by classification schemes based on neural networks (e.g. Banerji et al. 2010) and making use of support vector machines (Huertas-Company et al. 2011). Finally, the third category, which finds widespread use, includes, for example, the concentration index (Strateva et al. 2001; Stoughton et al. 2002; Kauffmann et al. 2003), the location in colour-magnitude space (Baldry et al. 2004), the Sérsic index (Blanton et al. 2003; Bell et al. 2004; Jogee et al. 2004; Ravindranath et al. 2004; Barden et al. 2005), the location in the $NUV - r$ resp. $u - r$ vs. $\log(n)$ plane (Kelvin et al. 2012; Driver et al. 2012), the location in the space defined by the SDSS f_{dev} parameter (i.e., the fraction of a galaxy's flux which is fit by the de Vaucouleurs profile (de Vaucouleurs 1948) in the best fit linear combination of a de Vaucouleurs and an exponential profile) and the axis ratio of the best fit exponential profile, q_{exp} (Tempel et al. 2011), and, in the case of high- z galaxies the location in the $(U - V) - (V - J)$ restframe colour-colour plane (Patel et al. 2012).

Overall, the advantages and disadvantages of the automatic schemes can also be categorized in a similar manner. Schemes in the category i) ideally require well resolved imaging, which may be difficult to obtain for faint galaxies in wide field imaging surveys, even in the local universe. Furthermore they require detailed imaging products, often including intermediate data reduction products which are not archived, making an independent morphological classification very time consuming and/or computationally expensive, especially for large data sets. Schemes in category ii), on the other hand, require the implementation of a complex analysis algorithm in addition to the existence of a training set of objects with known morphologies, and may require assumptions about the nature of the statistical distribution of the parameters considered. Finally, for the third category, the simple parameterization must

limit either the degree to which the selection recovers all members of a given morphological category, or the level at which the classification is robust against contamination, even for proxies which make use of structural information. Furthermore, it should be noted that the majority of the methods considered make use of parameters linked directly to ongoing star-formation, and as such may introduce a bias into the star-formation properties of a selected galaxy sample. For example in category i), the clumpiness parameter in the CAS scheme traces localized current star formation in spirals, while in category ii) both the methods of Banerji et al. (2010) and Huertas-Company et al. (2011) make use of galaxy colours, and Banerji et al. (2010) uses texture of the imaging as well. Finally in category iii) a range of simple proxies make use of the colour bimodality, linked to star-formation, of the galaxy population.

In the following we present a non-parametric method for selecting spirals based on the combinations of two and three photometric and simple structural parameters. The method is based on a discretization of the parameter space spanned by the parameter combination performed using an adaptive grid which increases the resolution in regions of high galaxy parameter space density. The division of the discretized parameter space into a spiral and a non-spiral subvolume is calibrated using the morphological classifications of GALAXY ZOO Data Release 1 (DR1; Lintott et al. 2011). We quantify the performance of each parameter combination in terms of completeness and purity, identifying those with the best performance, also investigating parameter combinations which make no use of properties directly linked to ongoing star-formation. This approach can be considered formally analogous to the classifications of stars in discrete spectral classes as discussed in the review of Morgan & Keenan (1973).

We describe the data used in Sect. 2 and the method in Sect. 3. We then investigate the performance of the parameter combinations in Sect. 4 and compare the performance of our selection with other methods in Sect. 5. We discuss our results and the applicability of the method in Sect. 6, and apply the selection method to obtain a reliable sample of spirals as a basis for investigating the intrinsic scatter in the stellar mass - specific star-formation rate relation of this class of galaxies in Sect. 7. Finally, we close by summarizing our results in Sect. 8. Throughout the paper we assume an $\Omega_M = 0.3$, $\Omega_\lambda = 0.7$, $H_0 = 70 \text{ kms}^{-1} \text{ Mpc}^{-1}$ cosmology.

2 DATA

Within this work we aim to investigate the efficacy and performance as proxies of various combinations of UV/optical photometric parameters for the morphological selection of spiral galaxies. To facilitate this comparison and broaden the range of possible proxies we have endeavored to create an unbiased sample of galaxies with as much available data as possible. We have selected all spectroscopic objects with `SpecClass= 2` (Galaxies) from the seventh data release (DR7) of SDSS (Abazajian et al. 2009) which lie within the GALEX MIS depth (1500s; Martin et al. 2005; Morrissey et al. 2007) footprint. We have matched this sample to the catalogue of the MPA/JHU analysis of SDSS DR7 spectra

(providing emission line fluxes) and to the catalogue of single Sérsic fits recently published by Simard et al. (2011) using the SDSS unique identifiers, and to the preliminary NUV GALEX MIS depth unique NUV source galaxy catalogue GCAT MSC (Seibert et al., 2013 in prep.) using a 4 arcsec matching radius¹. Given the uncertainties involved with flux redistribution (e.g., Robotham & Driver 2011), we have chosen to treat only one-to-one matches between SDSS and GALEX as possessing reliable UV data.

Where multiple spectra are available for a single photometric object, we have used the spectrum corresponding to the the MPA/JHU entry. Where multiple spectra form the MPA/JHU reductions are available, we have chosen the spectrum with the smallest redshift error. In order to obtain a reliable benchmark morphological classification, we have matched the sample to the GALAXY ZOO data release 1 (DR1) (Lintott et al. 2008, 2011) catalogue of visual, red-shift debiased morphological classifications (Bamford et al. 2009; Lintott et al. 2011) using the photometric SDSS `ObjId`, limiting ourselves to local universe sources (redshift $z \leq 0.13$). This selection provides a sample of 166429 galaxies (referred to as the *Opticalsample*), with a subsample of 114047 NUV detected, uniquely matched sources (referred to as the *NUVsample*). Finally we have cross-matched these samples to the catalogue of $\sim 14\text{k}$ bright SDSS DR4 (Adelman-McCarthy et al. 2006) galaxies with detailed morphological classifications of Nair & Abraham (2010). This results in a subsample of 6220 sources with two independent morphological classifications (which we refer to as the *NAIRsample*). 4470 sources in the *NAIRsample* have NUV detections, and we refer to this subsample as the *NUVNAIRsample*.

2.1 SDSS and GALEX photometry

We have retrieved Petrosian magnitudes, the foreground extinction, the f_{dev} and q_{exp} parameters from the SDSS photometric pipeline, and the petrosian 50th (R_{50}) and 90th (R_{90}) percentile radii in the u , g , r , and i pass-bands from the SDSS database using CasJobs. To obtain total (Sérsic) magnitudes we use the algorithms for converting SDSS petrosian magnitudes to total Sérsic magnitudes derived by Graham et al. (2005). The obtained magnitudes have been corrected for foreground extinction using the extinction values supplied by SDSS (derived from the Schlegel, Finkbeiner, & Davis (1998) dust maps). K-corrections to $z = 0$ have been performed using `kcorrect_v4.2` (Blanton & Roweis. 2007).

GALEX sources with NUV artifact flag indicating window or dichroic reflections have been removed from the sample. The FUV and NUV magnitudes of the matched GALEX sources have been corrected for foreground extinction using the Schlegel, Finkbeiner, & Davis (1998) dust maps and $A_{FUV} = 8.24 E(B - V)$ and $A_{NUV} = 8.2 E(B - V)$ following Wyder et al. (2007).

Photometric stellar mass estimates have been calculated

¹ We note that the GCAT MSC includes a cut on $S/N > 3$

from the extinction and k-corrected magnitudes using the $g - i$ colour and the i -band absolute magnitude M_i as

$$\log(M_*) = -0.68 + 0.7 \cdot (g - i) - 0.4M_i + 0.4 \cdot 4.58, \quad (1)$$

where the factor 4.58 is identified as the solar i -band magnitude, following the prescription provided by Taylor et al. (2011).

2.2 Emission line data

We make use of the emission line fluxes from the $H\alpha$, $H\beta$, [NII]6584, and [OIII]5007 emission lines, and of the underlying continuum flux for the $H\alpha$ emission line. Using these data we calculate the $H\alpha$ equivalent width, and the Balmer Decrement. We use the $H\alpha$ equivalent width as an independent observable in the investigation of possible biases in the morphological proxies for spiral galaxies and the Balmer Decrement in the correction of observed UV photometry for the effects of attenuation due to dust using the prescription of Calzetti et al. (2000) (cf. section 7). The ratios of $H\alpha$ to [NII]6584 and $H\beta$ to [OIII]5007 are used to identify galaxies hosting an AGN following the prescription of Kewley et al. (2006). The emission line data is taken from the MPA/JHU analysis of the SDSS DR7 spectra² (performed by Stephane Charlot, Guineverre Kauffmann, Simon White, Tim Heckman, Christy Tremonti, and Jarle Brinchmann). We calculate the $H\alpha$ EQWs as the ratio of emission line to continuum flux. As the listed uncertainties are formal we multiply the uncertainties on the emission line fluxes by the factors listed on the website, in particular by 2.473 for $H\alpha$, 2.039 for [NII]6584, 1.882 for $H\beta$, and 1.566 for [OIII]5007. These factors have been determined by the MPA/JHU group using comparisons of duplicate spectra of objects within the sample. For sources with $S/N < 3$ we use three times the uncertainty as an upper limit. For details on the data and catalogues we refer the reader to the MPA/JHU website.

2.3 Single Sérsic Profile Fits

In constructing the parameter combinations for use as proxies, we have made use of the structural information supplied by the simultaneous fits in the g - and r -band of single Sérsic profiles to SDSS photometry made available by Simard et al. (2011), performed using GIM2D. In particular, we have used the Sérsic index n , the single Sérsic effective radius r_e (half-light semi-major axis) in the r -band, and the ellipticity e . Simard et al. (2011) find that multiple component fits are not justified for most SDSS sources given the resolution of the imaging, and similar issues will afflict other surveys as well. Therefore we have chosen to use the largely robust single Sérsic profile fits in this work. We note, however, that Bernardi et al. (2012) have recently argued that for the brightest sources two component fits are preferable over single Sérsic fits and that for these sources the sizes derived by Simard et al. (2011) are systematically too small. This will not affect the analysis presented here, as these sources form a minority of the population considered

and the effect will be accounted for in the calibration of the proxies.

2.4 GALAXY ZOO DR1

The GALAXY ZOO DR1 (Lintott et al. 2008; Bamford et al. 2009; Lintott et al. 2011) represents the largest and faintest sample of galaxies with morphological classifications based on visual inspection. We have employed these morphological classifications, specifically those of the sources with redshift debiased classifications as provided by Bamford et al. (2009), as a benchmark morphological classification. Such a debiased estimate is only possible for sources with spectroscopic redshifts. Rather than a binary classification, GALAXY ZOO DR1 provides a probability for the source being an elliptical ($P_{E,DB}$) or a spiral ($P_{CS,DB}$ (CS denotes the combined spiral class, i.e summed over the sub-classes available in GALAXY ZOO DR1, i.e clockwise spiral, anti-clockwise spiral, spiral edge-on/other), based on the outcome of all classifications of the object³. It is then up to the user to decide where to place the threshold for assuming a classification is reliable. After eyeballing a selection of galaxies we have chosen to treat a debiased probability of 0.7 or greater as being a reliable classification in the context of this work. Such a choice results in three populations: i) spirals, ii) ellipticals, and iii) undefined. We will show that this choice leads to highly pure samples of spirals.

2.5 The Sample of Nair & Abraham (2010)

Nair & Abraham (2010) have provided detailed visual morphological classifications of 14,034 galaxies in the SDSS DR4 (Adelman-McCarthy et al. 2006), with $0.01 \leq z \leq 0.1$ and $g' < 16\text{mag}$. They provide T-types for each source as follows: (c0, E0, E+): -5; (S0-): -3; (S0, S0+): -2; (S0/a): 0; (Sa): 1; (Sa/b): 2, (Sb): 3, (Sb/c): 4; (Sc): 5; (Sc/d): 6; (Sd): 7; (Sdm): 8; (Sm): 9; (Im): 10; (unknown/?): 99. In the context of this work we have treated the T-types 1-10 as late-types/spirals. We note, however, that this sample does not extend to the depth of the GALAXY ZOO sample, and that, in spite of its size, independent visual classifications are only available for ~ 6000 of the galaxies in our sample. As such the population of faint and/or marginally resolved galaxies which dominate the source counts of current wide-field blind optical surveys, is only marginally sampled.

3 A NON-PARAMETRIC, CELL-BASED CLASSIFICATION SCHEME

In order to obtain reliable morphological selections of galaxies based upon photometric parameters, the parameter chosen must ideally display a distinct separation into two populations corresponding to the different morphological

² The data and catalogues are available from <http://www.mpa-garching.mpg.de/SDSS/>

³ It should be noted that due to the debiasing procedure, $P_{CS,DB} + P_{E,DB}$ for a given galaxy is not necessarily equal to unity.

categories. Prominent examples of such one parameter separation criteria are the concentration index $C_{idx} = R_{90}/R_{50}$ (e.g., Strateva et al. 2001) and the Sérsic index n (e.g., Blanton et al. 2003).

Other schemes make use of combinations of two or more parameters such as the $u - r$ colour and r -band absolute magnitude (Baldry et al. 2004), or the q_{exp} and f_{dev} parameters, possibly in combination with $u - r$ colour information (Tempel et al. 2011). Recently, Kelvin et al. (2012) and Driver et al. (2012) have suggested the use of a UV/optical colour ($u - r$, resp. $NUV - r$) and the Sérsic index n in separating spiral and elliptical galaxies, and a variant of the $NUV - r$, n selection has been used by Grootes et al. (2013) to select spiral galaxies for the purpose of a radiation transfer analysis and has proven to be efficient.

Common to all these approaches is the difficulty of selecting a curve/surface of separation between the two populations, which includes as large a fraction of the desired category as possible, whilst simultaneously keeping the level of contamination as low as feasible. In addition, this choice may be influenced by further requirements upon the recovery fraction and purity of the sample, which can be envisioned to vary with application.

The functional form of the curve or hypersurface providing the optimal separation of the two populations is not known a priori, and an appropriate choice can be non-trivial, even if the population of spiral galaxies is easily separable from the non-spiral population by eye. Furthermore, the sharp division between the two is generally not exhibited by the galaxy populations which show a more gradual transition. Accordingly, sharp transitions in combination with simple parameterizations where the functional form may be ill-suited can give rise to large contaminations.

3.1 Discretizing Parameter Space

Rather than making assumptions about the functional form of the separation, we discretize the space spanned by the parameters used into individual cells. For each cell we can, using the Galaxy Zoo classifications measure the fraction of the galaxies residing therein which are spirals (i.e. $P_{CS,DB} \geq 0.7$), and define a subvolume of the total parameter space composed of cells with a fraction greater than some desired threshold fraction. This subvolume can then be associated with a population of spiral galaxies.

As further discussed in sections 3.2 and 4 the discretization is performed using a random subsample of 50k (respectively 30k for the NUV sample) galaxies. Since the density of galaxies in parameter space is highly non-uniform, the discretization is performed using an adaptive scheme, with the number of divisions along each axis increasing by a power of 2 with each level of refinement. Cells at each level are further refined to a maximum of 3 refinement steps, i.e., to 16 subdivisions per axis, if they contain more than 200 galaxies. This adaptive refinement allows the resolution of the grid to adapt to the density of sources in parameter space, and ensures that the dividing hypersurface is both well-defined and well-resolved in regions of high and low source density. The value of the refinement threshold has little impact on the result of the classification, provided the

calibration sample is large enough that sufficient refinement is achievable. A high threshold in combination with a small calibration sample will lead to a low level of resolution and a potential increase in the level of contamination. Choosing the threshold for refinement at 200 galaxies is found to allow for sufficient resolution, whilst maintaining bin populations at such a level that the relative uncertainties of the spiral fraction for the most finely subdivided cells are less than 0.3 on average. Fig. 1 shows the resultant grid for a possible combination of three parameters (the grids will differ for different parameter combinations).

In each of the cells we calculate the the fraction of spirals F_{sp} as

$$F_{sp} = \frac{N_{GZ,sp}}{N_{cell}}, \quad (2)$$

where $N_{GZ,sp}$ is the number of GALAXY ZOO spirals (i.e., $P_{CS,DB} \geq 0.7$) in the cell and N_{cell} is the total number of galaxies in the cell. The associated relative error $\Delta F_{sp,rel}$ is calculated using Poisson statistics and error propagation. We then define those cells with $F_{sp} \geq \mathcal{F}_{sp}$ (where \mathcal{F}_{sp} is the threshold spiral fraction) and $\Delta F_{sp,rel} \leq 1$. to be spiral cells, i.e., we treat every object in the cell as a spiral galaxy, and thus obtain a decomposition of the parameter space into a spiral and a non-spiral subvolume. The choice of $\Delta F_{sp,rel} \leq 1$. has little effect in terms of the total population, as large values of $\Delta F_{sp,rel}$ correspond to scarcely populated cells. The population is obviously more sensitive to the choice of the limiting fraction \mathcal{F}_{sp} , with lower values leading to larger recovery fractions but lower purity. Here we have experimented with different values of \mathcal{F}_{sp} and find $\mathcal{F}_{sp} = 0.5$ to result in a very pure, yet nevertheless largely complete, sample of spirals. In this work, we continue with the choice $\mathcal{F}_{sp} = 0.5$, however, note that if a larger recovery fraction or an even greater purity is desired this choice can be altered.

In this work we focus on combinations of two and three parameters. While the approach is theoretically applicable to higher dimensional parameter spaces, the requirements on resolution and cell population impose an effective limit of three dimensions for the calibration sample available. We provide a decomposition of the parameter space for three combinations of three parameters in appendix A, which also provide the values of F_{sp} and $\Delta F_{sp,rel}$ for all cells. We emphasize that any reader wanting to use the discretizations provided must check for systematic differences between his/her data/parameters and those used in this work, and refer the reader to Sect. 6.3 for a further discussion of the application of the results presented here to other surveys.

3.2 Sensitivity to the Calibration Sample

In order to provide a robust and reliable decomposition of the parameter space, the calibration sample must adequately sample the parameter space and the galaxy population, i.e. it must contain sufficient galaxies to achieve the required level of resolution and to sufficiently populate the individual cells, as well as be representative of the galaxy population as a whole. On the other hand, as the calibration sample must be visually classified, it is desirable to understand how the

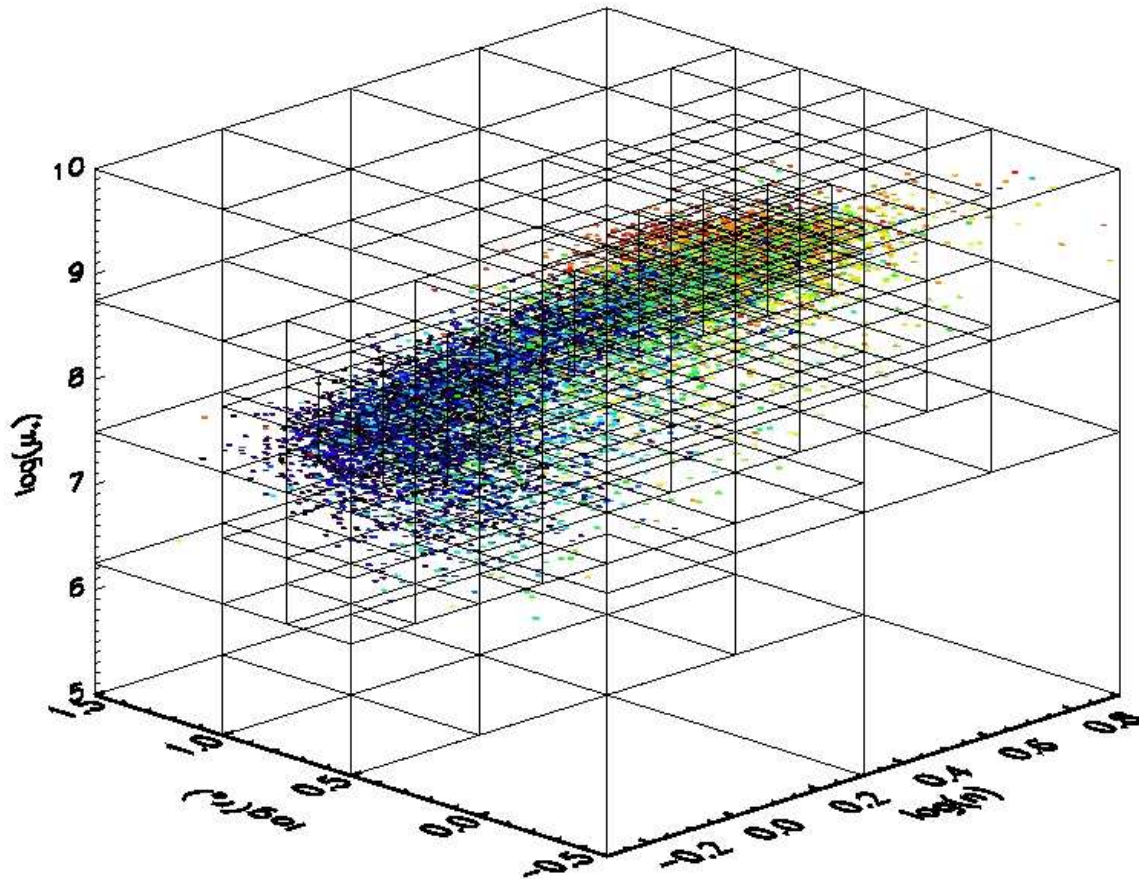


Figure 1. Cell grid obtained for the parameter combination $(\log(n), \log(r_e), \log(\mu_*))$ using a calibration sample of 10000 galaxies. The 10k galaxies of the calibration sample are overplotted with colour-coding according to the probability of being a spiral (blue : spiral, red: non-spiral).

performance of the method relies on the size of the calibration sample. In particular, it is of interest how the purity, completeness, and contamination by ellipticals of the sample depend on the size of the calibration sample.

We define the purity fraction P_{pure} as

$$P_{\text{pure}} = \frac{N_{\text{sel,SP}}}{N_{\text{sel}}}, \quad (3)$$

where N_{sel} is the number of galaxies selected as spirals by the cell-based method, and $N_{\text{sel,SP}}$ is the number of those galaxies which are visually classified as being spiral galaxies. Analogously the contamination fraction P_{cont} is defined as the fraction of the selected galaxies which are visually classified as ellipticals, i.e.

$$P_{\text{cont}} = \frac{N_{\text{sel,E}}}{N_{\text{sel}}}. \quad (4)$$

The completeness fraction of the sample P_{comp} is defined as

$$P_{\text{comp}} = \frac{N_{\text{sel,SP}}}{N_{\text{SP}}}, \quad (5)$$

where N_{SP} is the total number of visually classified spirals in the sample being classified by the cell-based method.

Fig. 2 shows the fractional purity, completeness, and contamination by elliptical galaxies for samples selected using a combination of the parameters Sérsic index $(\log(n))$, effective radius in the r -band $(\log(r_e))$, and stellar mass surface

density $(\log(\mu_*))$, as a function of the size of the calibration sample (this parameter combination is found to perform well in selecting simultaneously pure and complete samples of spirals; for further details on the parameters, the parameter combinations, and their performance we refer the reader to Sect. 4). The values at each sample size correspond to the mean obtained from 5 random realizations of a calibration sample of that size, with the error bars corresponding to the $1-\sigma$ standard deviation. In each case, the calibration sample is drawn from the whole of the GALAXY ZOO sample.

The figure shows the performance in classifying three test samples: i) the entire optical galaxy sample using the visual classifications of spirals provided by GALAXY ZOO (solid), ii) the optical galaxy sample with independent morphological classifications provided by Nair & Abraham (2010) making use of these to define which galaxies really are spirals (dash-dotted), and iii) the optical galaxy sample with morphological classifications provided by Nair & Abraham (2010), but making use of the visual classifications provided by GALAXY ZOO (dashed). When calculating the contamination by ellipticals for GALAXY ZOO-based definitions we assume all sources with $P_{\text{E,DB}} \geq 0.5$ to be ellipticals. For each of the test samples contamination decreases while the completeness and purity increase markedly with increasing size of the calibration sample. However, calibration sample

sizes greater than $\sim 50k$ galaxies no longer lead to a large improvement of the performance. The improvement in performance with increasing size of the calibration sample is particularly striking for the optical sample matched to the bright galaxy sample of Nair & Abraham (2010). The increasing sample size enables a higher resolution, thus increasing purity and decreasing contamination by allowing regions of parameter space to be excluded, while simultaneously allowing the full extent of the parameter space occupied by spiral galaxies to be sufficiently sampled, increasing completeness by including other sections of the parameter space.

Even for the smallest sample sizes the performance of the method does not appear to depend strongly on the specific realization of the calibration sample, as shown by the errorbars. However, there is nevertheless a notable decrease in the $1-\sigma$ uncertainty around the mean with increasing sample size from $\sim 1 - 1.5\%$ to $\lesssim 0.5\%$, i.e calibration with a larger sample leads to a more robust and reliable discretization.

In light of these results, we have chosen a calibration sample of 50k galaxies for discretizations of the parameter space for the optical sample (i.e., without the requirement of an NUV detection), and a subsample of 30k of these galaxies for the discretizations of the parameter space for the NUV sample (i.e., with the requirement of an NUV detection). This allows the rest of the sample to be used as a semi-independent test population with which to investigate the performance of a given parameter combination. As we desire the method to be applicable over the full redshift range considered $z \leq 0.13$ we randomly select the calibration sample from this redshift range.

4 PARAMETER COMBINATIONS

In the context of this work we focus on a suite of directly observed and derived parameters for the purpose of identifying spiral galaxies which consists of a UV/optical colour ($u-r$, respectively $NUV-r$ for the NUV matched sample), the Sérsic index n , the effective radius r_e (half-light semi-major axis), the i -band absolute magnitude, the ellipticity e , the stellar mass M_* , and the stellar mass surface density μ_* calculated as

$$\mu_* = \frac{M_*}{2\pi r_e^2}. \quad (6)$$

The usefulness of the $u-r$ colour and the Sérsic index in selecting spirals is well documented (e.g., Baldry et al. 2004 respectively Barden et al. 2005). Similarly, as spiral galaxies are often assumed to be largely star-forming, the $NUV-r$ colour may be assumed to be of use. We have chosen to include the i -band magnitude M_i (a directly observable tracer of stellar mass) and the derived parameter stellar mass M_* , as early-type galaxies are, on average, more massive than late-types. Furthermore, at a given stellar mass, it appears likely that a rotationally-supported spiral will be more radially extended than a pressure-supported early-type galaxy, hence we make use of the effective radius. This also implies that the stellar mass surface density of sources may be useful in separating spirals from non-spirals. While for a spiral the value of μ_* derived using Eq. 6

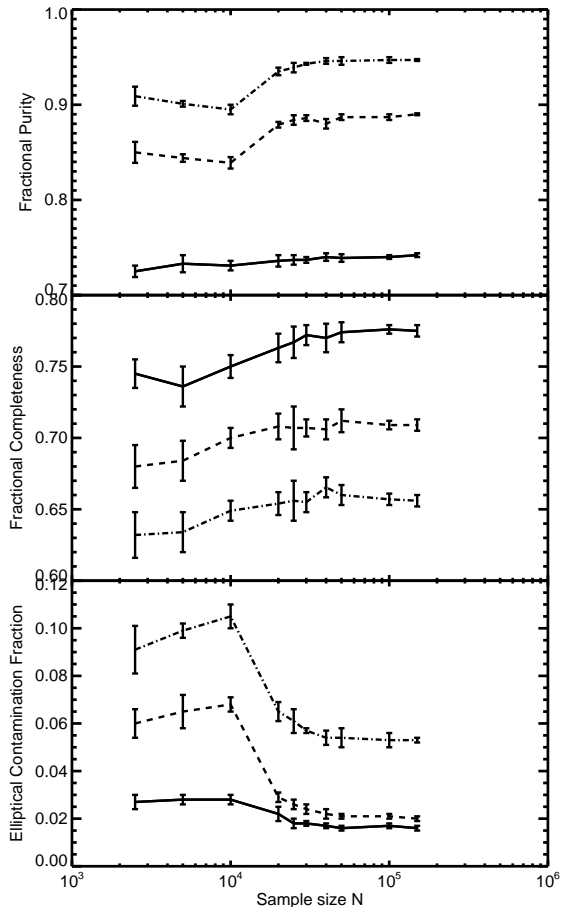


Figure 2. Fractional purity (top), fractional completeness (middle), and fractional contamination by ellipticals (bottom) for a selection of spirals obtained using the Sérsic index (i.e. $\log(n)$), the effective radius in the r -band (i.e. $\log(r_e)$), and the stellar mass surface density (i.e. $\log(\mu_*)$), as a function of the size of the calibration sample. The solid line corresponds to the results obtained when classifying the optical sample (i.e without the requirement of an NUV detection), while the dash-dotted line corresponds to the results obtained when classifying the optical sample with morphological classifications by Nair & Abraham (2010) defining spirals using these detailed classifications, and the dashed line corresponds to the optical sample matched to the Nair & Abraham (2010) catalogue but using the GALAXY ZOO visual classifications. The data points correspond to the mean of 5 random realizations of the calibration sample drawn from the optical galaxy sample with the error bars corresponding to the $1-\sigma$ standard deviation about the mean.

is readily interpretable in a physical sense⁴, the value derived in this manner for a true ellipsoid will tend to underestimate the actual surface density of the object, as the approximation of the surface area using r_e as in Eq. 6 will tend to overestimate the projected surface area. Hence, any observed separation of the spiral and non-spiral populations in this parameter will represent a lower limit

⁴ As a spiral galaxy can be assumed to be circular to first order, the effective radius can be used to derive a reasonable estimate of the surface area and consequently of the stellar mass surface density.

to the actual separation. Finally we have included the observed ellipticity e , as the objects on the sky which appear most elliptical are likely to be spirals observed at a more edge-on orientation. We note, however, that the use of ellipticity as a parameter will bias any selection of spirals towards sources seen edge-on.

Our goal is to identify (multiple) optimal sets of parameters which can be used as morphological proxies in the selection of highly pure and largely complete samples of spiral galaxies. As NUV data is only available for a subset of the total sample we perform the investigations in parallel both for the *OPTICALsample*, as well as the *NUVsample*.

For the *OPTICALsample* we perform the discretization of the parameter space using a sample of 50k galaxies randomly drawn from the *OPTICALsample* (the same sample is used for all parameter combinations) and classify the performance using the *OPTICALsample* and the *NAIRsample* (i.e. the subsample with morphological classifications from Nair & Abraham (2010)). For the NUV preselected sample (the *NUVsample*) we perform the discretizations using a sample of 30k galaxies with NUV detections (randomly sampled from the sample of 50k galaxies used for the *OPTICALsample*), and in this case classify the performance using the entire *NUVsample*, and the *NUVNAIRsample* (i.e., the subsample of galaxies with morphological classifications from Nair & Abraham (2010) and NUV detections.)

Fig. 3 shows the distributions of the parameters for the entire *OPTICALsample* (dashed), as well as for the randomly selected subset of 50k galaxies in the calibration subsample (solid). As expected, the distributions for the two samples are so similar as to be indistinguishable in Fig. 3 with the differences being smaller than the line width⁵ The figure shows the distributions for the galaxies in the samples classified as spirals ($P_{CS,DB} \geq 0.7$, blue), ellipticals ($P_{E,DB} \geq 0.7$, red), non-spirals ($P_{CS,DB} < 0.7$, green), and undefined ($P_{CS,DB} < 0.7$ and $P_{E,DB} < 0.7$, orange) using GALAXY ZOO.

As expected, the spiral and elliptical populations are reasonably separated in terms of UV/optical colour and Sérsic index. However, the overlap between the spiral and undefined populations is nevertheless large for these parameters. Furthermore, the distribution of μ_* notably also displays a distinct separation of the two populations, and even shows a separation between the spiral and undefined populations. The parameters stellar mass, effective radius, and i -band absolute magnitude show the expected trends in the populations as previously discussed. The distribution of ellipticities, however, is noteworthy. As expected, the spiral sample dominates the largest values of ellipticity and displays a separation from the undefined population at high ellipticity. However, at intermediate and lower values of e there is considerable overlap with the other populations. Furthermore, the population of spirals as defined by GALAXY ZOO appears biased towards high values of

ellipticity, i.e. galaxies seen edge-on⁶. As a consequence a discretization of parameter space using this calibration sample and e in the parameter combination will also be biased towards high values of ellipticity (even more so, than due to the intrinsic overlap of the spiral and non-spiral sample at low and intermediate values of e). However, the bias will not affect the discretization of the parameter space for combinations of parameters which are, to first order, independent of the orientations of the galaxies with respect to the observer (e.g. $\log(r_e)$, $\log(M_*)$, $\log(\mu_*)$, M_i , $\log(n)$ ⁷. In such cases, the distribution of ellipticities of spiral galaxies in each of the cells may be expected to be similar to that of the entire calibration sample, hence the bias towards edge-on systems will have no effect.

The bias of the GALAXY ZOO spiral sample must also be taken into account when quantifying the performance of different combinations of parameters. When using samples relying on the GALAXY ZOO classifications as test samples, the bias in e can give rise to spuriously complete samples in combination with e as a selection parameter. In spite of this bias, we nevertheless choose to use the GALAXY ZOO sample for calibration and testing purposes, as it represents the only large and faint sample of visually classified galaxies with a wide range of homogeneous ancillary data available. We check for effects arising from the ellipticity bias using the bright subsample of galaxies with independent visual classifications by Nair & Abraham (2010), which does not display an ellipticity bias.

Fig. 4 shows the same for the parameter distributions of the *NUVsample* and the randomly selected subset of 30k galaxies constituting the NUV calibration sample.

Comparing the parameter distributions between the *OPTICALsample* and the *NUVsample* shown in Figs. 3 & 4, the samples appear remarkably similar. Nevertheless, Kolmogorov-Smirnov and χ^2 tests indicate that, in spite of their similar appearance, the null hypothesis that the parameter distributions in these samples are the same has low probability ($p \leq 0.03$). However, if one considers only the subsamples of spirals and ellipticals, the tests find no statistically significant difference in the parameter distributions for the *OPTICALsample* and the *NUVsample* ($p \geq 0.37$), with the exception of the $u-r$ and $NUV-r$ colours ($p \leq 8 \cdot 10^{-4}$), indicating that the NUV pre-selection mainly affects the undefined population and its size relative to the spiral and elliptical populations. Despite of these differences, overall, the use of UV-preselection only has a small effect on the parameter distributions, in comparison with the large shift in the distributions between the morphological categories. This qualitative impression is confirmed for the optical properties of spirals and ellipticals, the null hypothesis being supported with $p \geq 0.37$. A might

⁶ For an unbiased sample one would expect a flat distribution in ellipticity

⁷ A bias in ellipticity can potentially give rise to a slight bias towards redder UV/optical colours, as edge-on spirals appear redder on average. However, we have found no significant evidence of such a bias. Recent work by Pastrav et al. (2013a) has also found that fully resolved dust rich galaxies seen edge-on may appear larger than when seen face-on, however, the strength of this effect remains to be quantified for marginally resolved sources.

⁵ This is quantitatively supported by the fact that Kolmogorov-Smirnov tests (and two sample χ^2 -tests for similarity for the discrete distributions in e, n , and r_e) support the null hypothesis that the samples have the same distribution ($p \geq 0.49$).

be expected, the null hypothesis is, however, rejected for the $NUV - r$ and $u - r$ colors ($p \leq 8 \cdot 10^{-4}$). The NUV pre-selection also appears to affect the undefined population and its size relative to the spiral and elliptical distributions, even in the optical parameters, the null hypothesis being rejected for this class for all parameters.⁸

Our goal in this work is to identify parameter combinations which provide a pure, but also largely complete sample of spiral galaxies. As such an additional important figure of merit in quantifying the performance of the different parameter combinations is the bijective discrimination power P_{bij} which we define as the product of P_{pure} and P_{comp} as defined in Eqs. 3, 5, i.e.

$$P_{\text{bij}} = P_{\text{pure}} \cdot P_{\text{comp}}. \quad (7)$$

This provides a measure of the efficacy of the parameter combination at simultaneously selecting a pure and complete sample of spirals from the test samples. P_{bij} can take on values between 0 and 1, with 1 corresponding to a perfectly pure and complete sample. As a reference, a selected sample with $P_{\text{pure}} = 0.75$ and $P_{\text{comp}} = 0.7$ (good values of completeness and purity) would have $P_{\text{bij}} = 0.525$. Applying this metric to the GALAXY ZOO classifications as used in this work of the Nair & Abraham (2010) sample, one finds that the GALAXY ZOO classifications attain $P_{\text{pure}} = 0.984$ and $P_{\text{comp}} = 0.732$, resulting in $P_{\text{bij}} = 0.720$ for the Nair & Abraham (2010) sample of bright galaxies. In the case of test samples using the visual classifications provided by GALAXY ZOO, the purity refers to the subsample of reliable spirals (i.e. with $P_{\text{CS,DB}} \geq 0.7$). However, not all galaxies which do not fulfill this criterion will be ellipticals. Rather, a fraction may be spirals with a less certain classification. In order to quantify the extent to which the sample is contaminated by ellipticals we also provide the value of P_{cont} as defined in Eq. 4, where we define all sources with $P_{\text{E,DB}} \geq 0.5$ to be ellipticals.

4.1 Application to optical samples

In the following we investigate the performance of selections using parameters which can be applied to samples without the requirement of UV data, i.e. $u - r$ colour, $\log(n)$, $\log(r_e)$, $\log(M_*)$, $\log(\mu_*)$, M_i , and e . The figures of merit involving completeness P_{comp} and P_{bij} are given in relation to the *OPTICALsample* and the *NAIRsample*.

4.1.1 Two parameter cells applied to optical samples

Tables 1 and 2 show the figures of merit achieved when testing using the *OPTICALsample* and the *NAIRsample*, respectively, for all 21 unique combinations of two parameters drawn from the suite applicable to optical samples.

Testing the performance of different parameter combinations using the *OPTICALsample*, we find that the parameters $\log(\mu_*)$ and $\log(r_e)$ are efficient at selecting complete samples, with all samples with $P_{\text{comp}} \geq 0.7$ involving combinations including at least one of these parameters. These parameters also perform well in selecting pure samples, as most combinations involving them attain values of $P_{\text{pure}} > 0.7$. In concert with either $\log(\mu_*)$ or $\log(r_e)$, the parameter $\log(n)$ also leads to pure and complete samples of spirals (in particular $(\log(n), \log(r_e))$ attains the highest value of $P_{\text{bij}} = 0.529$). Using e in parameter combinations leads to selections which are highly pure on average ($P_{\text{pure}} \gtrsim 0.71$), but have comparably low values of completeness ($P_{\text{comp}} < 0.6$), and accordingly have low bijective discrimination power. A notable exception to this is the combination $(\log(\mu_*), e)$ with $P_{\text{pure}} = 0.710$, $P_{\text{comp}} = 0.744$, and $P_{\text{bij}} = 0.528$, the second highest value of P_{bij} overall. However, this may be influenced by the ellipticity bias in the test sample (see the previous discussion in Sect. 4).

Interestingly, use of the $u - r$ colour does not of itself lead to very pure samples, as the purity of, e.g., the combinations $(u - r, \log(M_*))$ and $(u - r, M_i)$ is only ~ 0.6 , while similar combinations (e.g., $(\log(r_e), \log(M_*))$) attain much greater values. In addition, the completeness attained by using the $u - r$ colour is strongly dependent upon the second parameter used. If the second parameter is more bimodal, e.g. $\log(\mu_*)$, the combination provides good purity and completeness, while the completeness drops for parameters with less separation of the populations (e.g. M_i). Similarly, the Sérsic index is less efficient than expected, as the bijective discrimination power of the combinations of $\log(n)$ with $\log(M_*)$ and M_i (but also $u - r$), is low compared to that attained in combination with $\log(r_e)$ and $\log(\mu_*)$. Overall, the combination $(\log(n), \log(r_e))$ has the greatest bijective discrimination power ($P_{\text{bij}} = 0.529$) closely followed by the combination $(\log(\mu_*), e)$ with $(P_{\text{bij}} = 0.528)$ and the combinations $(\log(r_e), \log(M_*))$, $(\log(r_e), \log(\mu_*))$, and $(\log(n), \log(\mu_*))$ all with $P_{\text{bij}} \approx 0.5$. Amongst these combinations $(\log(n), \log(r_e))$ and $(\log(n), \log(\mu_*))$ have the lowest values of contamination by ellipticals with $P_{\text{cont}} \leq 0.032$, i.e. the lowest values attained by any parameter combination.

Table 2 shows the values for the figures of merit obtained when testing using the *NAIRsample*, using both the independent morphological classifications of Nair & Abraham (2010) and the GALAXY ZOO visual classifications.

Overall, the purity of the selections obtained when testing the parameter combinations using the *NAIRsample* with GALAXY ZOO visual classifications is greater than for the *OPTICALsample* with values of $P_{\text{pure}} \sim 0.8 - 0.9$, indicating, that some of the ‘impurities’ in the selections from the *OPTICALsample* are very likely unreliably classified spirals. On the other hand, the fractional completeness of the selections is of order 0.05 – 0.1 less than for the *OPTICALsample*. An exception to this are the combinations including e , for which the fractional completeness is ~ 0.2 less. This stronger decrease in completeness reflects the bias towards large values of e in the *OPTICALsample* which is not present in the *NAIRsample*. As for the *OPTI-*

⁸ This statement is valid for the combination of UV and optical photometric depths in the dataset used in this work. We caution that for different datasets this may not necessarily be true.

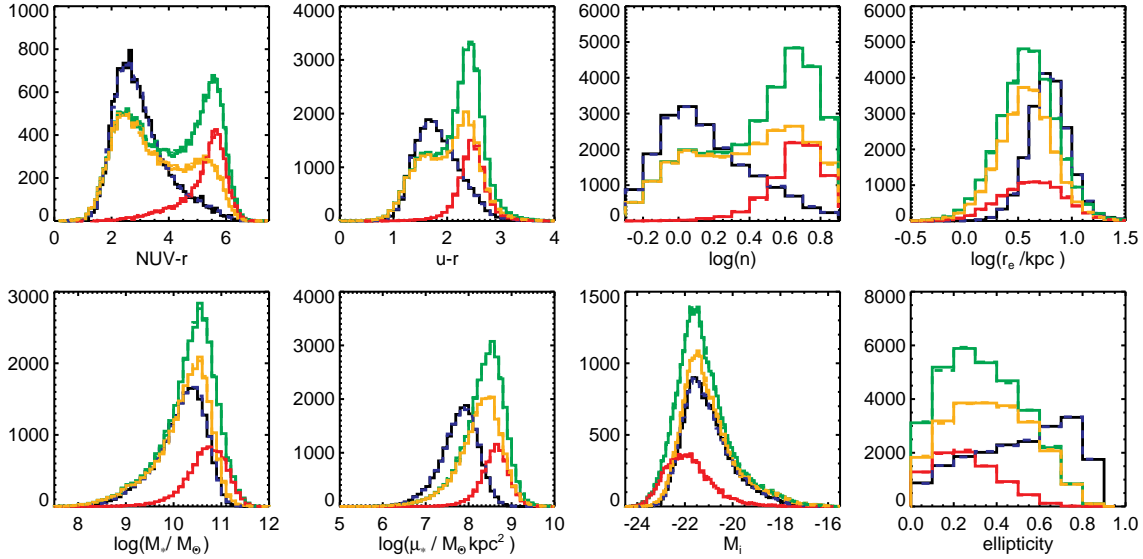


Figure 3. Distribution of the parameters in the entire *OPTICALsample* (dashed) and the calibration sample as defined in Sect. 3.2 for the population of spirals (blue), ellipticals (red), non-spirals (green), and undefined (orange). The distributions of the whole sample and the calibration subsample are nearly indistinguishable as differences are smaller than the line width.

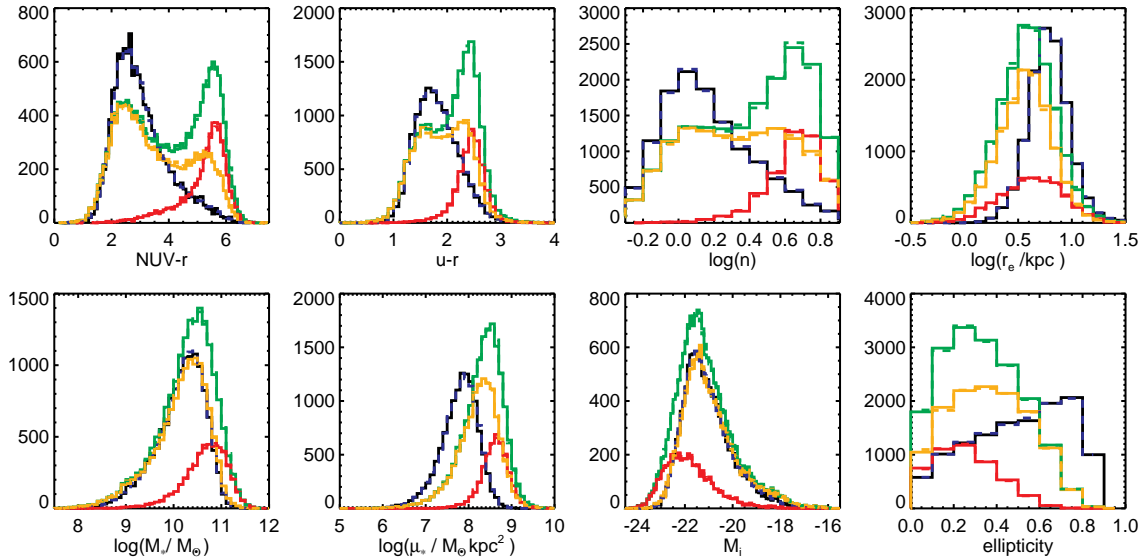


Figure 4. Distribution of the parameters in *NUVsample* (dashed) and *NUV* the calibration sample as defined in Sect. 3.2 (solid) for the population of spirals (blue), ellipticals (red), non-spirals (green), and undefined (orange). The distributions of the whole sample and the calibration sample are nearly indistinguishable.

CALsample, the parameter combination with the greatest bijective discrimination power is $(\log(n), \log(r_e))$. Unlike for the *OPTICALsample*, however, the combination with the second largest value of P_{bij} is $(\log(n), \log(\mu_*))$, which also attains the lowest value of contamination by ellipticals, rather than $(\log(\mu_*), e)$ (likely due to the removal of the ellipticity bias as previously discussed). As for the *OPTICALsample* the 5 combinations with the highest values of P_{bij} ($(\log(n), \log(r_e))$, $(\log(n), \log(\mu_*))$, $(u - r, \log(\mu_*))$,

$(\log(r_e), \log(M_*))$, $(\log(\mu_*), M_i)$) all include either $\log(r_e)$ or $\log(\mu_*)$. Furthermore, $\log(n)$ again leads to very pure and complete selections in combination with $\log(r_e)$ or $\log(\mu_*)$. In addition, its efficiency in combination with other parameters is also increased (e.g., $(\log(n), M_i)$).

Testing using the *NAIRsample* with the independent classifications of Nair & Abraham (2010) leads to very similar results. However, the fractional purity of the selections is even larger, further underscoring the conclusion that a

Table 1. $N_{\text{sel}}, P_{\text{pure}}, P_{\text{comp}}, P_{\text{bij}}, P_{\text{cont}}$ for combinations of two parameters applied to the *OPTICALsample*.

Parameter combination	N_{sel}	P_{pure}	P_{comp}	P_{bij}	P_{cont}
$(u - r, \log(n))$	67436	0.617	0.655	0.404	0.060
$(u - r, \log(r_e))$	57168	0.710	0.639	0.453	0.054
$(u - r, \log(M_*))$	63194	0.580	0.577	0.334	0.084
$(u - r, \log(\mu_*))$	65254	0.690	0.709	0.489	0.054
$(u - r, M_i)$	61275	0.584	0.563	0.329	0.079
$(u - r, e)$	47567	0.719	0.538	0.387	0.042
$(\log(n), \log(r_e))$	64179	0.724	0.731	0.529	0.032
$(\log(n), \log(M_*))$	67304	0.623	0.660	0.412	0.055
$(\log(n), \log(\mu_*))$	67026	0.688	0.726	0.499	0.027
$(\log(n), M_i)$	71707	0.615	0.694	0.427	0.055
$(\log(n), e)$	55547	0.685	0.599	0.410	0.038
$(\log(r_e), \log(M_*))$	63985	0.711	0.716	0.509	0.048
$(\log(r_e), \log(\mu_*))$	61678	0.721	0.700	0.504	0.048
$(\log(r_e), M_i)$	61263	0.699	0.674	0.471	0.071
$(\log(r_e), e)$	44938	0.760	0.538	0.409	0.051
$(\log(M_*), \log(\mu_*))$	60231	0.724	0.686	0.496	0.040
$(\log(M_*), M_i)$	45243	0.578	0.412	0.238	0.069
$(\log(M_*), e)$	34862	0.737	0.405	0.298	0.062
$(\log(\mu_*), M_i)$	65086	0.697	0.714	0.497	0.049
$(\log(\mu_*), e)$	66627	0.710	0.744	0.528	0.035
(M_i, e)	35006	0.730	0.402	0.293	0.072

large contribution to the ‘impurity’ of the selections is due to unreliably classified spirals. which also has amongst the lowest contamination by ellipticals. The combinations with the highest bijective discrimination power again include either $\log(r_e)$, $\log(\mu_*)$, and/or $\log(n)$, supporting the previous findings.

Overall, the parameters $\log(\mu_*)$, $\log(r_e)$, and $\log(n)$ appear to be most efficient at selecting pure and complete samples of spirals.

4.1.2 Three parameter cells applied to optical samples

While the performance of selections using only two parameters is already encouraging, it seems likely that the purity and completeness, and hence the bijective discrimination power, as well as the fractional contamination, can be improved by using more information in the selection, i.e. by using a third parameter.

Tables 3 and 4 show the figures of merit achieved when testing using the *OPTICALsample* and the *NAIRsample*, respectively, for all 35 unique combinations of three parameters drawn from the suite applicable to optical samples.

Testing the performance of different combinations of three parameters using the *OPTICALsample*, we find that both the purity and completeness attained are greater, on average, than for combinations of two parameters, as shown in Table 3. In most cases, the use of additional information in the form of a third parameter leads to a simultaneous increase in purity and completeness. In some cases, however, the deprojection along the additional third axis can lead to the inclusion of more parameter space, causing an increase of completeness at the cost of a decrease in purity or, vice versa, to the exclusion of parameter space, increasing purity at the expense of completeness (e.g., $(\log(r_e), \log(M_*))$

with $P_{\text{pure}} = 0.711$ & $P_{\text{comp}} = 0.716$ and $(\log(r_e), \log(M_*), M_i)$ with $P_{\text{pure}} = 0.707$ & $P_{\text{comp}} = 0.739$, respectively $(\log(n), M_i)$ with $P_{\text{pure}} = 0.615$ & $P_{\text{comp}} = 0.694$ and $(\log(n), M_i, e)$ with $P_{\text{pure}} = 0.708$ & $P_{\text{comp}} = 0.641$).

As for the combinations of two parameters, combinations of three parameters including e attain high values of purity (13/15 with $P_{\text{pure}} \geq 0.7$, and 6/15 with $P_{\text{pure}} \geq 0.75$). Of these combinations those which include two other parameters which efficiently select pure and complete samples of spirals (e.g., $\log(r_e)$ and $\log(\mu_*)$) also attain very high values of completeness ($\gtrsim 0.7$), leading to high values of P_{bij} (of the 10 combinations with the highest values of P_{bij} , the first 6 include e). However, as for the combinations of two parameters, these high values of completeness are partially due to the ellipticity bias of the *OPTICALsample*. We will discuss the performance of these combinations on the basis of tests using the *NAIRsample* below. However, we note that all six combinations with the highest values of P_{bij} include $\log(r_e)$ and/or $\log(\mu_*)$. The remaining four parameter combinations of the 10 with the highest values of P_{bij} are (in descending order) $(\log(n), \log(r_e), M_i)$ with $P_{\text{bij}} = 0.576$, $(\log(n), \log(r_e), \log(\mu_*))$ with $P_{\text{bij}} = 0.572$, $(\log(n), \log(M_*), \log(\mu_*))$ with $P_{\text{bij}} = 0.565$, and $(\log(n), \log(r_e), \log(M_*))$ with $P_{\text{bij}} = 0.564$, all of which also include the parameters $\log(r_e)$ and/or $\log(\mu_*)$ in addition to $\log(n)$, indicating the potential of these parameters to select pure and complete samples of spirals. In addition these four combinations exhibit the lowest contamination by ellipticals with $P_{\text{cont}} \lesssim 0.02$. As for combinations of two parameters, however, $\log(n)$ is only efficient in combination with another efficient parameter. The same is true for the parameter $u - r$ colour. Finally, the parameters M_i , and $\log(M_*)$, are efficient in combination with combinations of $\log(r_e)$, $\log(\mu_*)$, and $\log(n)$.

Testing the performance of three-parameter combinations using the *NAIRsample* with GALAXY ZOO visual classifications (Table 4), we again find again find that the values of P_{pure} and P_{comp} are greater than for combinations of two parameters. Comparison of the values of purity with those obtained for the *OPTICALsample* also again indicate that a fraction of the ‘impurity’ arises from the unreliable classification of spirals.

Of the 10 combinations with the highest values of P_{bij} none include e , indicating that the high values attained for the *OPTICALsample* are, at least partially, due to the ellipticity bias. In descending order, the combinations with the greatest bijective discrimination power are $(\log(n), \log(r_e), \log(\mu_*))$, $(\log(n), \log(M_*), \log(\mu_*))$, $(\log(n), \log(\mu_*), M_i)$, $(\log(n), \log(r_e), M_i)$, and $(\log(n), \log(r_e), \log(M_*))$, supporting the results obtained using the *OPTICALsample*.

Testing using the *NAIRsample* with the independent classifications of Nair & Abraham (2010) again leads to very similar results. In terms of choice of the most effective parameters, the 5 parameter combinations with the greatest values of P_{bij} are the same as found when using the GALAXY ZOO visual classifications, although the combination with the overall greatest bijective discrimination power is $(\log(n), \log(\mu_*), M_i)$ rather than $(\log(n), \log(r_e), \log(\mu_*))$.

Table 2. N_{sel} , P_{pure} , P_{comp} , P_{cont} , and P_{bij} for combinations of two parameters applied to *NAIRsample* using the GALAXY ZOO visual classifications (columns 3-6) and the independent classifications of Nair & Abraham (2010, columns 7-9). In the case of the independent classifications the contamination fraction is taken to be the complement of the purity (i.e. this includes sources with T-type = 99).

Parameter combination	N_{sel}	GALAXY ZOO				Nair & Abraham (2010)		
		P_{pure}	P_{comp}	P_{bij}	P_{cont}	P_{pure}	P_{comp}	P_{bij}
$(u - r, \log(n))$	2104	0.839	0.601	0.505	0.048	0.923	0.575	0.530
$(u - r, \log(r_e))$	1828	0.882	0.549	0.485	0.040	0.9234	0.496	0.458
$(u - r, \log(M_*))$	1856	0.799	0.505	0.403	0.075	0.883	0.481	0.425
$(u - r, \log(\mu_*))$	2053	0.884	0.618	0.546	0.030	0.950	0.572	0.544
$(u - r, M_i)$	1815	0.803	0.496	0.398	0.068	0.888	0.473	0.420
$(u - r, e)$	1111	0.832	0.315	0.262	0.038	0.926	0.302	0.280
$(\log(n), \log(r_e))$	2479	0.821	0.693	0.569	0.086	0.874	0.641	0.560
$(\log(n), \log(M_*))$	2173	0.824	0.609	0.502	0.055	0.904	0.581	0.525
$(\log(n), \log(\mu_*))$	2124	0.873	0.631	0.551	0.023	0.950	0.597	0.567
$(\log(n), M_i)$	2382	0.811	0.657	0.533	0.063	0.894	0.630	0.563
$(\log(n), e)$	1435	0.833	0.407	0.339	0.033	0.929	0.394	0.366
$(\log(r_e), \log(M_*))$	2006	0.893	0.610	0.545	0.026	0.947	0.558	0.528
$(\log(r_e), \log(\mu_*))$	1948	0.901	0.598	0.538	0.024	0.956	0.546	0.523
$(\log(r_e), M_i)$	1868	0.866	0.551	0.477	0.050	0.926	0.507	0.469
$(\log(r_e), e)$	1354	0.792	0.365	0.289	0.091	0.854	0.339	0.290
$(\log(M_*), \log(\mu_*))$	1858	0.906	0.573	0.519	0.021	0.959	0.523	0.502
$(\log(M_*), M_i)$	1351	0.827	0.380	0.314	0.057	0.899	0.356	0.320
$(\log(M_*), e)$	798	0.786	0.213	0.168	0.056	0.905	0.212	0.192
$(\log(\mu_*), M_i)$	2012	0.891	0.610	0.543	0.027	0.953	0.562	0.535
$(\log(\mu_*), e)$	1880	0.874	0.559	0.489	0.023	0.950	0.522	0.497
(M_i, e)	793	0.784	0.212	0.166	0.067	0.898	0.209	0.187

Overall we find that the optimum results in terms of purity and simultaneous completeness for optical samples are obtained by combinations of three parameters including $\log(r_e)$, $\log(\mu_*)$, $\log(n)$, and $\log(M_*)$ or M_i , notably $(\log(n), \log(r_e), \log(\mu_*))$, $(\log(n), \log(r_e), M_i)$, and $(\log(n), \log(\mu_*), M_i)$.

4.2 Application to NUV-preselected samples

Spirals are very often found to be systems with on-going star formation, consequently possessed of a younger stellar population emitting in the UV (FUV and NUV) and displaying blue UV/optical colours. Early-type galaxies on the other hand are generally found to be more quiescent and redder. Where available, the use of UV properties of sources may thus prove efficient in the selection of spiral galaxies. Similarly, a pre-selection on UV emission will enhance the purity of a sample of star-forming spiral galaxies, at the expense of removing UV-faint, quiescent spirals. In the following we investigate the performance of selections using parameters which can be applied to samples pre-selected on the availability of NUV data (the *NUVsample* and *NUVNAIRsample* in this case), i.e. $NUV - r$ colour, $\log(n)$, $\log(r_e)$, $\log(M_*)$, $\log(\mu_*)$, M_i , and e . The figures of merit involving completeness P_{comp} and P_{bij} are given in relation to the NUV preselected samples ($P_{comp,n}$ and $P_{bij,n}$) and to the optical samples for comparison ($P_{comp,o}$ and $P_{bij,o}$).

4.2.1 Two parameter cells applied to the NUV samples

Tables 5 and 6 show the figures of merit for all 21 unique combinations of two parameters applied to the NUV

preselected samples.

Testing using the *NUVsample*, the combinations with the greatest values of $P_{bij,n}$ are $(\log(\mu_*), e)$ with $P_{bij,n} = 0.542$ (although the completeness may be influenced by the ellipticity bias), $(\log(r_e), \log(M_*))$ with $P_{bij,n} = 0.532$, $(\log(n), \log(r_e))$ with $P_{bij,n} = 0.529$, $(\log(r_e), \log(\mu_*))$ with $P_{bij,n} = 0.525$, and $(\log(r_e), M_i)$ with $P_{bij,n} = 0.523$. The parameters $\log(r_e)$ and $\log(\mu_*)$ again result in the most simultaneously pure and complete samples, particularly in combination with $\log(M_*)$, M_i , or $\log(n)$. In particular $\log(\mu_*)$ leads to selections with high purity (4/5 with $P_{pure} \geq 0.7$ and 2/5 with $P_{pure} \geq 0.74$). While the $NUV - r$ colour and Sérsic index are less efficient at selecting pure and complete samples than expected, only attaining values of $P_{pure} \gtrsim 0.6$ in combination with another strongly bimodal parameter, the use of the $NUV - r$ colour does, however, predominantly lead to samples with high completeness ($\gtrsim 0.68$), even in combination with $\log(M_*)$ and M_i .

Making use of the *NUVNAIRsample* with GALAXY ZOO visual classifications we find that the combinations with the greatest bijective discrimination power are $(NUV - r, \log(r_e))$ with $P_{bij,n} = 0.624$, $(NUV - r, \log(M_*))$ with $P_{bij,n} = 0.612$ and $(NUV - r, M_i)$ with $P_{bij,n} = 0.608$, followed by $(\log(n), \log(r_e))$ with $P_{bij,n} = 0.568$ and $(\log(n), \log(\mu_*))$ with $P_{bij,n} = 0.567$. The use of $NUV - r$ and a marginally efficient parameter applied to the NUV preselected sample leads to highly complete samples ($P_{comp,n} \sim 0.74$), while $NUV - r$ in combination with efficient parameters leads to pure samples (e.g. $(NUV - r, \log(\mu_*))$ with $P_{pure} = 0.888$). Combinations with $\log(\mu_*)$ all result in very pure samples with $P_{pure} > 0.87$,

Table 3. N_{sel} , P_{pure} , P_{comp} , P_{bij} , and P_{cont} for combinations of three parameters applied to the *OPTICAL* sample.

Parameter combination	N_{sel}	P_{pure}	P_{comp}	P_{bij}	P_{cont}
$(u - r, \log(n), \log(r_e))$	65154	0.724	0.743	0.539	0.024
$(u - r, \log(n), \log(M_*))$	69906	0.625	0.688	0.430	0.058
$(u - r, \log(n), \log(\mu_*))$	66453	0.709	0.741	0.526	0.033
$(u - r, \log(n), M_i)$	70880	0.623	0.695	0.433	0.058
$(u - r, \log(n), e)$	60259	0.682	0.647	0.442	0.042
$(u - r, \log(r_e), \log(M_*))$	65727	0.713	0.737	0.525	0.038
$(u - r, \log(r_e), \log(\mu_*))$	63633	0.720	0.721	0.520	0.042
$(u - r, \log(r_e), M_i)$	67015	0.710	0.749	0.532	0.047
$(u - r, \log(r_e), e)$	63993	0.764	0.770	0.588	0.022
$(u - r, \log(M_*), \log(\mu_*))$	62888	0.719	0.712	0.512	0.039
$(u - r, \log(M_*), M_i)$	64714	0.582	0.593	0.345	0.082
$(u - r, \log(M_*), e)$	56811	0.701	0.626	0.439	0.045
$(u - r, \log(\mu_*), M_i)$	62289	0.720	0.706	0.508	0.037
$(u - r, \log(\mu_*), e)$	66140	0.735	0.766	0.563	0.023
$(u - r, M_i, e)$	56083	0.713	0.629	0.449	0.045
$(\log(n), \log(r_e), \log(M_*))$	65708	0.738	0.764	0.564	0.018
$(\log(n), \log(r_e), \log(\mu_*))$	66581	0.739	0.774	0.572	0.017
$(\log(n), \log(r_e), M_i)$	66937	0.740	0.779	0.576	0.021
$(\log(n), \log(r_e), e)$	60988	0.776	0.745	0.577	0.019
$(\log(n), \log(M_*), \log(\mu_*))$	67149	0.731	0.773	0.565	0.019
$(\log(n), \log(M_*), M_i)$	68977	0.624	0.678	0.423	0.052
$(\log(n), \log(M_*), e)$	58955	0.692	0.643	0.445	0.042
$(\log(n), \log(\mu_*), M_i)$	68151	0.716	0.768	0.549	0.018
$(\log(n), \log(\mu_*), e)$	67837	0.715	0.763	0.546	0.020
$(\log(n), M_i, e)$	57541	0.708	0.641	0.454	0.036
$(\log(r_e), \log(M_*), \log(\mu_*))$	63189	0.717	0.713	0.511	0.044
$(\log(r_e), \log(M_*), M_i)$	66491	0.706	0.739	0.521	0.052
$(\log(r_e), \log(M_*), e)$	64608	0.754	0.767	0.579	0.027
$(\log(r_e), \log(\mu_*), M_i)$	66374	0.707	0.739	0.523	0.055
$(\log(r_e), \log(\mu_*), e)$	65079	0.759	0.777	0.590	0.026
$(\log(r_e), M_i, e)$	58887	0.753	0.698	0.525	0.038
$(\log(M_*), \log(\mu_*), M_i)$	63574	0.713	0.713	0.509	0.045
$(\log(M_*), \log(\mu_*), e)$	65408	0.754	0.776	0.585	0.027
$(\log(M_*), M_i, e)$	49084	0.686	0.530	0.363	0.061
$(\log(\mu_*), M_i, e)$	66104	0.745	0.775	0.577	0.033

usually, however, at the cost of completeness.

Using the independent morphological classifications of Nair & Abraham (2010) we obtain very similar results, with the most bijectively powerful combinations including $NUV - r$ with M_i , $\log(M_*)$, or $\log(r_e)$ followed by those combining $\log(n)$, $\log(r_e)$, and $\log(\mu_*)$.

For the bright subsample of Nair & Abraham (2010) $NUV - r$ efficiently selects pure and complete samples of spirals, however, the efficiency of the parameters $\log(M_*)$ and $\log(r_e)$ also remains high.

Overall, the parameters $\log(n)$, $\log(r_e)$, and $\log(\mu_*)$ appear efficient in selecting pure and complete samples of spirals as for optical samples. In addition, the $NUV - r$ colour in combination with NUV preselection is also efficient in this respect.

A comparison of the figures of merit of the selections applied to the NUV pre-selected samples with those of comparable parameter combinations applied to the optical samples indicates that the use of such a preselection enhances the ability of the method to select pure and complete samples of spirals, with $P_{\text{bij},n}$ being, on average, greater than P_{bij} for comparable parameter combinations applied to the optical samples. This is due to the NUV pre-

selection removing non-spiral contaminants, thus enlarging the spiral subvolume by making spirals more dominant and increasing the purity of spiral cells. In many cases both the completeness and the purity of the selections increase (e.g., $(\log(r_e), \log(M_*))$). However, in some cases the increase in completeness is accompanied by a (slight) decrease in the purity, indicating that the enlargement of parameter space is the dominant effect.

Nevertheless, it must be born in mind that these samples are complete with respect to the preselected sample and may be biased against intrinsically UV faint spiral galaxies as well as strongly attenuated spirals seen edge-on if these sources lie below the NUV detection threshold.

4.2.2 Three parameter cells applied to the NUV samples

Application of combinations of three parameters to the NUV preselected samples has much the same effect as for the optical samples, i.e. the purity and completeness, and consequently the bijective discrimination power, increase with respect to selections based on two parameters. The same processes as discussed in Sect. 4.1.2 apply. Tables 7 and 8 show the figures of merit for combinations of three

Table 4. N_{sel} , P_{pure} , P_{comp} , P_{cont} , and P_{bij} for combinations of three parameters applied to *NAIRsample* using the GALAXY ZOO visual classifications (columns 3-6) and the independent classifications of Nair & Abraham (2010, columns 7-9). In the case of the independent classifications the contamination fraction is taken to be the complement of the purity (i.e. this includes sources with T-type = 99).

Parameter combination	GALAXY ZOO					Nair & Abraham (2010)		
	N_{sel}	P_{pure}	P_{comp}	P_{bij}	P_{cont}	P_{pure}	P_{comp}	P_{bij}
$(u - r, \log(n), \log(r_e))$	2339	0.867	0.690	0.598	0.041	0.925	0.640	0.592
$(u - r, \log(n), \log(M_*))$	2280	0.829	0.643	0.533	0.053	0.910	0.614	0.559
$(u - r, \log(n), \log(\mu_*))$	2270	0.872	0.674	0.588	0.033	0.941	0.632	0.595
$(u - r, \log(n), M_i)$	2353	0.826	0.662	0.546	0.052	0.909	0.633	0.576
$(u - r, \log(n), e)$	1627	0.846	0.469	0.396	0.030	0.930	0.448	0.416
$(u - r, \log(r_e), \log(M_*))$	2100	0.897	0.641	0.575	0.020	0.951	0.587	0.558
$(u - r, \log(r_e), \log(\mu_*))$	2068	0.894	0.630	0.563	0.024	0.951	0.577	0.549
$(u - r, \log(r_e), M_i)$	2059	0.888	0.622	0.553	0.030	0.944	0.571	0.538
$(u - r, \log(r_e), e)$	1872	0.888	0.566	0.502	0.017	0.947	0.521	0.493
$(u - r, \log(M_*), \log(\mu_*))$	1995	0.896	0.609	0.546	0.022	0.956	0.560	0.535
$(u - r, \log(M_*), M_i)$	2066	0.809	0.569	0.460	0.071	0.886	0.537	0.476
$(u - r, \log(M_*), e)$	1375	0.834	0.391	0.326	0.038	0.919	0.371	0.341
$(u - r, \log(\mu_*), M_i)$	1992	0.896	0.608	0.545	0.020	0.958	0.560	0.536
$(u - r, \log(\mu_*), e)$	1932	0.893	0.587	0.524	0.019	0.962	0.546	0.525
$(u - r, M_i, e)$	1452	0.842	0.416	0.351	0.035	0.915	0.390	0.356
$(\log(n), \log(r_e), \log(M_*))$	2319	0.881	0.696	0.613	0.024	0.941	0.646	0.608
$(\log(n), \log(r_e), \log(\mu_*))$	2364	0.884	0.712	0.629	0.024	0.945	0.660	0.624
$(\log(n), \log(r_e), M_i)$	2360	0.879	0.706	0.621	0.032	0.935	0.652	0.610
$(\log(n), \log(r_e), e)$	2142	0.867	0.632	0.548	0.045	0.920	0.582	0.536
$(\log(n), \log(M_*), \log(\mu_*))$	2347	0.885	0.707	0.626	0.024	0.946	0.657	0.621
$(\log(n), \log(M_*), M_i)$	2283	0.833	0.647	0.539	0.049	0.908	0.613	0.557
$(\log(n), \log(M_*), e)$	1703	0.847	0.491	0.416	0.039	0.926	0.466	0.432
$(\log(n), \log(\mu_*), M_i)$	2363	0.881	0.709	0.625	0.020	0.950	0.664	0.631
$(\log(n), \log(\mu_*), e)$	1989	0.873	0.591	0.516	0.019	0.953	0.560	0.534
$(\log(n), M_i, e)$	1686	0.856	0.492	0.421	0.035	0.921	0.459	0.422
$(\log(r_e), \log(M_*), \log(\mu_*))$	1983	0.901	0.608	0.548	0.023	0.955	0.556	0.531
$(\log(r_e), \log(M_*), M_i)$	2098	0.884	0.631	0.558	0.032	0.939	0.578	0.543
$(\log(r_e), \log(M_*), e)$	1888	0.895	0.575	0.514	0.019	0.953	0.528	0.504
$(\log(r_e), \log(\mu_*), M_i)$	2091	0.885	0.630	0.557	0.035	0.940	0.577	0.542
$(\log(r_e), \log(\mu_*), e)$	1908	0.899	0.584	0.525	0.018	0.958	0.536	0.514
$(\log(r_e), M_i, e)$	1731	0.870	0.513	0.446	0.034	0.932	0.473	0.441
$(\log(M_*), \log(\mu_*), M_i)$	1980	0.893	0.602	0.538	0.028	0.952	0.552	0.526
$(\log(M_*), \log(\mu_*), e)$	1926	0.899	0.590	0.530	0.017	0.958	0.541	0.518
$(\log(M_*), M_i, e)$	1447	0.838	0.413	0.346	0.048	0.909	0.430	0.391
$(\log(\mu_*), M_i, e)$	1922	0.900	0.589	0.530	0.017	0.957	0.539	0.516

parameters applied to the *NUVsample* and *NUVNAIRsample*.

The combination of three parameters with the highest value of P_{bij} when applied to the *NUVsample* is $(NUV - r, \log(r_e), e)$ with $P_{\text{bij},n} = 0.617$ ($P_{\text{pure}} = 0.777$, $P_{\text{comp},n} = 0.794$). Of the 10 combinations with the greatest bijective discrimination power, the first 7 again include e (and are likely affected by the ellipticity bias). However, all 10 combinations include $\log(r_e)$, $\log(\mu_*)$ and/or $\log(n)$. The three most efficient parameter combinations not including e are $(\log(n), \log(r_e), \log(\mu_*))$ ($P_{\text{pure}} = 0.744$, $P_{\text{comp},n} = 0.780$), $(\log(n), \log(r_e), M_i)$ ($P_{\text{pure}} = 0.749$, $P_{\text{comp},n} = 0.775$), and $(NUV - r, \log(r_e), M_i)$ ($P_{\text{pure}} = 0.731$, $P_{\text{comp},n} = 0.789$). Overall, the use of three parameter combinations applied to the NUV preselected *NUVsample* leads to very complete selections. Of the combinations not including e 18/20 have $P_{\text{comp},n} > 0.7$, 6 of which have $P_{\text{comp},n} > 0.77$. In particular, $NUV - r$ in combination with at least one efficient parameter leads to very complete selections with

$$P_{\text{comp},n} \gtrsim 0.73.$$

Testing the performance of combinations of three parameters using the *NUVNAIRsample* with GALAXY ZOO visual classifications the most bijectively powerful combination is $(NUV - r, \log(r_e), e)$ with $P_{\text{bij},n} = 0.645$ ($P_{\text{pure}} = 0.908$, $P_{\text{comp},n} = 0.711$; this result is not influenced by a bias in the test sample towards large values of e). However, of the ten most efficient combinations, this is the only one including e . The following 5 combinations with the highest values of $P_{\text{bij},n}$ are (in descending order): $(NUV - r, \log(n), \log(r_e))$, $(NUV - r, \log(r_e), M_i)$, $(\log(n), \log(r_e), \log(M_*))$, $(NUV - r, \log(n), \log(M_*))$, and $(NUV - r, \log(n), \log(\mu_*))$. Clearly $NUV - r$ applied in combination with another efficient parameter and NUV preselection leads to very pure and complete selections recovered from the bright subsample. Similar purity, but at the cost of completeness is also achieved by the parameter $\log(\mu_*)$, even without the parameter $NUV - r$ (e.g. $(\log(r_e), \log(M_*), \log(\mu_*))$).

Table 5. Purity, completeness, bijective discrimination power, and contamination for combinations of two parameters applied to *NUVsample*. Completeness and bijective discrimination power are listed w.r.t. the *OPTICALsample* ($P_{\text{comp,o}}$ and $P_{\text{bij,o}}$) and the *NUVsample* ($P_{\text{comp,n}}$ and $P_{\text{bij,n}}$).

Parameter combination	N_{sel}	P_{pure}	$P_{\text{comp,n}}$	$P_{\text{bij,n}}$	P_{cont}	$P_{\text{comp,o}}$	$P_{\text{bij,o}}$
(<i>NUV</i> − <i>r</i> , log(<i>n</i>))	53285	0.603	0.678	0.408	0.069	0.506	0.305
(<i>NUV</i> − <i>r</i> , log(<i>r_e</i>))	46791	0.722	0.713	0.514	0.042	0.532	0.384
(<i>NUV</i> − <i>r</i> , log(<i>M_*</i>))	56682	0.581	0.695	0.404	0.082	0.518	0.301
(<i>NUV</i> − <i>r</i> , log(<i>μ_*</i>))	47516	0.717	0.719	0.516	0.031	0.536	0.385
(<i>NUV</i> − <i>r</i> , <i>M_i</i>)	55825	0.582	0.685	0.399	0.081	0.511	0.298
(<i>NUV</i> − <i>r</i> , <i>e</i>)	40000	0.714	0.603	0.431	0.041	0.450	0.321
(log(<i>n</i>), log(<i>r_e</i>))	46867	0.731	0.723	0.529	0.033	0.540	0.395
(log(<i>n</i>), log(<i>M_*</i>))	53124	0.608	0.681	0.414	0.063	0.508	0.309
(log(<i>n</i>), log(<i>μ_*</i>))	51284	0.688	0.744	0.512	0.032	0.555	0.382
(log(<i>n</i>), <i>M_i</i>)	54617	0.606	0.698	0.423	0.064	0.521	0.315
(log(<i>n</i>), <i>e</i>)	37343	0.705	0.556	0.392	0.044	0.415	0.293
(log(<i>r_e</i>), log(<i>M_*</i>))	47184	0.731	0.727	0.532	0.039	0.543	0.397
(log(<i>r_e</i>), log(<i>μ_*</i>))	45305	0.741	0.708	0.525	0.036	0.529	0.392
(log(<i>r_e</i>), <i>M_i</i>)	49531	0.707	0.739	0.523	0.070	0.552	0.390
(log(<i>r_e</i>), <i>e</i>)	40215	0.734	0.623	0.457	0.083	0.465	0.341
(log(<i>M_*</i>), log(<i>μ_*</i>))	44472	0.742	0.696	0.517	0.032	0.520	0.386
(log(<i>M_*</i>), <i>M_i</i>)	38529	0.567	0.461	0.262	0.097	0.344	0.195
(log(<i>M_*</i>), <i>e</i>)	28449	0.731	0.439	0.321	0.075	0.327	0.239
(log(<i>μ_*</i>), <i>M_i</i>)	47342	0.718	0.717	0.515	0.037	0.535	0.384
(log(<i>μ_*</i>), <i>e</i>)	49323	0.721	0.751	0.542	0.030	0.560	0.404
(<i>M_i</i> , <i>e</i>)	24399	0.767	0.395	0.302	0.061	0.294	0.226

Table 6. Purity, completeness, bijective discrimination power, and contamination for combinations of two parameters applied to *NUVNAIRsample* using the GALAXY ZOO visual classifications (columns 3-8) and the independent classifications of Nair & Abraham (2010, columns 9-13). Completeness and bijective discrimination power are listed w.r.t. the *OPTICALsample* ($P_{\text{comp,o}}$ and $P_{\text{bij,o}}$) and the *NUVsample* ($P_{\text{comp,n}}$ and $P_{\text{bij,n}}$). In the case of the independent classifications the contamination fraction is taken to be the complement of the purity (i.e. this includes sources with T-type = 99).

Parameter combination	N_{sel}	P_{pure}	GALAXY ZOO					Nair & Abraham (2010)				
			$P_{\text{comp,n}}$	$P_{\text{bij,n}}$	P_{cont}	$P_{\text{comp,o}}$	$P_{\text{bij,o}}$	P_{pure}	$P_{\text{comp,n}}$	$P_{\text{bij,n}}$	$P_{\text{comp,o}}$	$P_{\text{bij,o}}$
(<i>NUV</i> − <i>r</i> , log(<i>n</i>))	1551	0.853	0.607	0.518	0.053	0.450	0.384	0.919	0.565	0.519	0.418	0.384
(<i>NUV</i> − <i>r</i> , log(<i>r_e</i>))	1801	0.869	0.719	0.624	0.044	0.533	0.463	0.914	0.650	0.594	0.483	0.441
(<i>NUV</i> − <i>r</i> , log(<i>M_*</i>))	1970	0.822	0.744	0.612	0.064	0.552	0.454	0.895	0.695	0.622	0.517	0.463
(<i>NUV</i> − <i>r</i> , log(<i>μ_*</i>))	1497	0.888	0.611	0.543	0.030	0.453	0.402	0.948	0.560	0.531	0.416	0.394
(<i>NUV</i> − <i>r</i> , <i>M_i</i>)	1950	0.824	0.738	0.608	0.064	0.547	0.451	0.896	0.689	0.617	0.512	0.459
(<i>NUV</i> − <i>r</i> , <i>e</i>)	1127	0.859	0.444	0.382	0.031	0.330	0.283	0.933	0.415	0.387	0.308	0.287
(log(<i>n</i>), log(<i>r_e</i>))	1790	0.831	0.683	0.568	0.084	0.507	0.421	0.879	0.623	0.548	0.461	0.405
(log(<i>n</i>), log(<i>M_*</i>))	1591	0.813	0.594	0.482	0.069	0.440	0.358	0.894	0.564	0.504	0.417	0.373
(log(<i>n</i>), log(<i>μ_*</i>))	1616	0.873	0.648	0.566	0.032	0.480	0.419	0.942	0.603	0.568	0.446	0.421
(log(<i>n</i>), <i>M_i</i>)	1706	0.813	0.637	0.518	0.070	0.472	0.384	0.896	0.606	0.543	0.448	0.402
(log(<i>n</i>), <i>e</i>)	944	0.815	0.353	0.288	0.049	0.262	0.213	0.915	0.342	0.313	0.253	0.232
(log(<i>r_e</i>), log(<i>M_*</i>))	1512	0.900	0.625	0.562	0.026	0.463	0.417	0.950	0.567	0.539	0.421	0.400
(log(<i>r_e</i>), log(<i>μ_*</i>))	1447	0.902	0.599	0.540	0.025	0.444	0.401	0.956	0.546	0.522	0.405	0.388
(log(<i>r_e</i>), <i>M_i</i>)	1630	0.842	0.630	0.531	0.075	0.467	0.394	0.890	0.572	0.509	0.425	0.378
(log(<i>r_e</i>), <i>e</i>)	1488	0.728	0.498	0.363	0.160	0.369	0.269	0.776	0.456	0.354	0.339	0.263
(log(<i>M_*</i>), log(<i>μ_*</i>))	1387	0.906	0.577	0.523	0.021	0.428	0.388	0.960	0.525	0.504	0.390	0.374
(log(<i>M_*</i>), <i>M_i</i>)	1263	0.792	0.459	0.364	0.097	0.340	0.270	0.859	0.428	0.368	0.318	0.273
(log(<i>M_*</i>), <i>e</i>)	728	0.731	0.244	0.178	0.092	0.181	0.132	0.865	0.249	0.215	0.185	0.160
(log(<i>μ_*</i>), <i>M_i</i>)	1488	0.898	0.613	0.551	0.026	0.455	0.408	0.953	0.559	0.533	0.416	0.396
(log(<i>μ_*</i>), <i>e</i>)	1397	0.886	0.568	0.504	0.022	0.422	0.374	0.953	0.525	0.500	0.390	0.372
(<i>M_i</i> , <i>e</i>)	631	0.751	0.218	0.163	0.094	0.161	0.121	0.876	0.218	0.191	0.162	0.142

Testing using the *NUVNAIRsample* with the independent morphological classifications of Nair & Abraham (2010) supports the importance of *NUV* − *r* as a parameter for selecting pure and complete samples of spirals under *NUV* preselection. The combinations with the largest bijective

discrimination power are (*NUV* − *r*, log(*n*), log(*M_{*}*)), (*NUV* − *r*, log(*n*), log(*r_e*)), and (*NUV* − *r*, log(*r_e*), *e*), with the use of *NUV* − *r* leading to very complete samples, as visible in the comparison of (*NUV* − *r*, log(*n*), log(*r_e*)) with

$(\log(n), \log(r_e), \log(\mu_*))$, or $(\log(n), \log(r_e), M_i)$.

To summarize, we find that for NUV preselected samples the use of $NUV - r$ as a parameter leads to very complete, and in the case of the bright subsample of Nair & Abraham (2010) also pure, selections of spiral galaxies. This is particularly the case in combination with $\log(r_e)$ and $\log(n)$, while combinations with $\log(\mu_*)$ are also efficient, but mostly improve the purity of selections at the expense of completeness. A comparison of the figures of merit for comparable parameter combinations applied to the optical and NUV samples shows, as for the combinations of two parameters, that the use of NUV preselection increases both purity and completeness on average. We again note, however, that the values of completeness are with respect to the NUV samples, and will be biased against UV-faint sources (these may be intrinsically UV faint or UV faint due to being seen edge-on and experiencing severe attenuation due to dust).

Overall, the parameters $\log(r_e)$, $\log(\mu_*)$, and $\log(n)$ appear efficient at selecting pure and complete samples of spirals, as for the optical samples. Under NUV preselection however, the $NUV - r$ colour becomes efficient at selecting complete and pure spiral samples, much more so that the $u - r$ colour for the optical samples. The most efficient combinations include $(NUV - r, \log(r_e), e)$, $(NUV - r, \log(n), \log(r_e))$, and $(\log(n), \log(r_e), \log(\mu_*))$.

4.2.3 Effects of NUV selection

As shown in Sect. 4.2.2, the use of NUV preselection results, on average, in samples with greater completeness and often also greater purity for comparable combinations of selection parameters. Under NUV preselection the parameter $NUV - r$ leads to efficient selections of complete samples of spirals, while attaining high values of purity for the bright subsample. As spiral galaxies are often star forming systems, this result is unsurprising. However, as discussed, NUV preselection will bias samples of spirals against intrinsically UV-faint systems, as well as against systems which are UV-faint due to severe attenuation (e.g. on account of being seen edge-on).

Overall, the efficiency of the considered parameter combinations in selecting pure and complete (under the aforementioned caveat) samples is enhanced by NUV preselection, with larger volumes of the parameter space being included in the spiral volume than for the whole sample, as indicated by increases in completeness accompanied by slight reductions in purity when using comparable parameter combinations with and without preselection. In addition, especially for combinations of three parameters, NUV preselection can also lead to an increase in purity accompanied by a decrease in completeness, as regions marginally dominated by spirals in the whole sample are excluded. On average, however, in both cases the value of $P_{\text{bij},n}$ is larger than P_{bij} for a comparable parameter combination applied to the *OPTICALsample*. Thus, depending upon the science goal of the selection, UV information could be a valuable asset in selecting samples of spirals. However, we caution that, in addition to the biases previously dis-

cussed, if the depth of the UV coverage is not such that it matches the depth of the optical data and encompasses the entire (realistic) colour range, UV preselection will strongly suppress the completeness attainable and introduce biases into any selections.

In light of these effects, the greater completeness of using only optical parameters applied to optical samples, as evidenced by the values of $P_{\text{comp},o}$ in, for example, Table 7 and the robustness against bias will likely outweigh the gain in purity achievable by NUV preselection for most applications.

4.3 Investigation of possible biases

Based on the figures of purity, completeness, and bijective discrimination power it is readily apparent that the use of combinations of three parameters generally leads to purer and simultaneously more complete samples of spirals than using only two parameters. Furthermore, the most important parameters appear to be $\log(r_e)$ & $\log(\mu)$, which provide the most efficient selection when complemented by $\log(n)$ and/or M_i . Applying an NUV preselection appears to further improve the attainable purity, and makes $NUV - r$ a further important selection parameter. However, although the purity, completeness, and bijective discrimination power are good indicators of a selection's performance, they provide little information about possible biases in the selections. While the cell-based method allows for a flexible surface of separation, any boundary in parameter space used in classifying objects entails that reliable spirals with strongly outlying values in the selection parameters may be missed, and that the selection may not be fully representative of the actual population of spirals.

In the following we will investigate the potential biases caused by the selection on the basis of four different representative combinations of three parameters ($(u - r, \log(r_e), e)$ resp. $(NUV - r, \log(r_e), e)$, $(\log(n), \log(r_e), \log(\mu_*))$, $(\log(n), \log(r_e), M_i)$, and $(\log(n, \log(M_*), \log(\mu_*))$), chosen to be amongst the most bijectively powerful. We will consider the distributions of the suite of parameters investigated for these selections, as well as consider the the distributions of the H α equivalent width as an independent observable and the T-type classification given by Nair & Abraham (2010) to investigate possible biases in the selections of spiral galaxies. Finally, we will investigate the redshift dependence of the selections of spiral galaxies.

4.3.1 Distributions of the parameter suite

Figs. 5 & 6 show the normalized distributions of all eight parameters in the suite investigated, after selection by four different representative combinations of three parameters ($(u - r, \log(r_e), e)$ resp. $(NUV - r, \log(r_e), e)$ in red, $(\log(n), \log(r_e), \log(\mu_*))$ in green, $(\log(n), \log(r_e), M_i)$ in blue, and $(\log(n, \log(M_*), \log(\mu_*))$ in orange), chosen to be amongst the most bijectively powerful, applied to both the *OPTICALsample* (Fig. 5) and to the *NAIRsample* (Fig. 6). For comparison the parameter's distribution for reliable spirals in the respective sample as defined by GALAXY

Table 7. Purity, completeness, bijective discrimination power, and contamination for combinations of three parameters applied to *NUVsample*. Completeness and bijective discrimination power are listed w.r.t. the *OPTICALsample* ($P_{\text{comp,o}}$ and $P_{\text{bij,o}}$) and the *NUVsample* ($P_{\text{comp,n}}$ and $P_{\text{bij,n}}$).

Parameter combination	N_{sel}	P_{pure}	$P_{\text{comp,n}}$	$P_{\text{bij,n}}$	P_{cont}	$P_{\text{comp,o}}$	$P_{\text{bij,o}}$
$(NUV - r, \log(n), \log(r_e))$	50514	0.726	0.774	0.562	0.028	0.577	0.419
$(NUV - r, \log(n), \log(M_*))$	56380	0.617	0.733	0.452	0.064	0.547	0.337
$(NUV - r, \log(n), \log(\mu_*))$	48707	0.716	0.736	0.527	0.032	0.549	0.39
$(NUV - r, \log(n), M_i)$	56496	0.616	0.734	0.452	0.064	0.548	0.337
$(NUV - r, \log(n), e)$	43708	0.695	0.641	0.445	0.044	0.478	0.332
$(NUV - r, \log(r_e), \log(M_*))$	48885	0.736	0.759	0.559	0.029	0.567	0.417
$(NUV - r, \log(r_e), \log(\mu_*))$	49163	0.737	0.765	0.564	0.029	0.571	0.421
$(NUV - r, \log(r_e), M_i)$	51151	0.731	0.789	0.577	0.033	0.589	0.430
$(NUV - r, \log(r_e), e)$	48396	0.777	0.794	0.617	0.014	0.592	0.460
$(NUV - r, \log(M_*), \log(\mu_*))$	46269	0.746	0.728	0.543	0.029	0.543	0.405
$(NUV - r, \log(M_*), M_i)$	56066	0.582	0.689	0.401	0.085	0.514	0.299
$(NUV - r, \log(M_*), e)$	43874	0.730	0.676	0.493	0.035	0.504	0.368
$(NUV - r, \log(\mu_*), M_i)$	48991	0.730	0.755	0.551	0.030	0.563	0.411
$(NUV - r, \log(\mu_*), e)$	49430	0.748	0.780	0.583	0.015	0.582	0.435
$(NUV - r, M_i, e)$	44092	0.734	0.683	0.501	0.033	0.509	0.374
$(\log(n), \log(r_e), \log(M_*))$	49304	0.744	0.773	0.575	0.020	0.577	0.429
$(\log(n), \log(r_e), \log(\mu_*))$	49665	0.744	0.780	0.580	0.022	0.582	0.433
$(\log(n), \log(r_e), M_i)$	49054	0.749	0.775	0.580	0.023	0.578	0.433
$(\log(n), \log(r_e), e)$	47441	0.765	0.766	0.586	0.029	0.571	0.437
$(\log(n), \log(M_*), \log(\mu_*))$	49945	0.736	0.775	0.571	0.020	0.579	0.426
$(\log(n), \log(M_*), M_i)$	53302	0.611	0.687	0.420	0.062	0.513	0.313
$(\log(n), \log(M_*), e)$	41242	0.702	0.611	0.429	0.044	0.456	0.320
$(\log(n), \log(\mu_*), M_i)$	50378	0.719	0.764	0.550	0.019	0.570	0.410
$(\log(n), \log(\mu_*), e)$	51054	0.715	0.770	0.551	0.026	0.575	0.411
$(\log(n), M_i, e)$	42160	0.705	0.627	0.443	0.046	0.468	0.330
$(\log(r_e), \log(M_*), \log(\mu_*))$	46264	0.738	0.721	0.532	0.033	0.538	0.397
$(\log(r_e), \log(M_*), M_i)$	48838	0.727	0.749	0.545	0.042	0.559	0.407
$(\log(r_e), \log(M_*), e)$	48793	0.764	0.786	0.600	0.028	0.586	0.448
$(\log(r_e), \log(\mu_*), M_i)$	48671	0.729	0.749	0.546	0.045	0.559	0.407
$(\log(r_e), \log(\mu_*), e)$	49571	0.762	0.797	0.607	0.027	0.595	0.453
$(\log(r_e), M_i, e)$	46084	0.757	0.736	0.556	0.043	0.549	0.415
$(\log(M_*), \log(\mu_*), M_i)$	47355	0.729	0.729	0.531	0.039	0.544	0.397
$(\log(M_*), \log(\mu_*), e)$	49250	0.762	0.791	0.603	0.028	0.590	0.450
$(\log(M_*), M_i, e)$	40952	0.698	0.603	0.421	0.065	0.450	0.314
$(\log(\mu_*), M_i, e)$	49331	0.757	0.787	0.596	0.031	0.588	0.445

ZOO is shown as a dash-dotted black line. Finally, the parameter's distribution for reliable spirals as defined by the independent morphological classifications of Nair & Abraham (2010), i.e. in the *NAIRsample*, is shown as a grey dash-dotted line.

Overall, the distributions of the parameters derived from the selections applied to the *OPTICALsample* (Fig. 5) coincide well with that of the GALAXY ZOO defined sample, indicating that the non-parametric method using three parameters is neither heavily influencing the parameter ranges available to the sample, nor is itself introducing large biases. Similarly, the parameter combinations for the selections applied to the *NAIRsample* also agree well with the parameter's distributions as defined by the GALAXY ZOO and Nair & Abraham (2010) visual classifications. Nevertheless, the effect of the individual choice of parameter combinations is visible in the distributions, with this being more pronounced for the application to the *NAIRsample*. For example, all combinations involving $\log(n)$ are biased towards lower values of this parameter than the visually defined samples, while the combination $(u - r, \log(r_e), e)$ traces them with higher fidelity. The discontinuous steep fall-off

towards redder $u - r$ colours of the selection determined by $(u - r, \log(r_e), e)$ (most pronounced in the *NAIRsample*), is also an example of the effects of the discretization.

The largest differences, both between the selections and the visually-defined samples, as well as between the selections themselves, are visible, however, in the distributions of ellipticity. While the distribution of e is more or less flat in the *NAIRsample*, as is to be expected for an unbiased sample, the GALAXY ZOO-defined spiral subsample of the *OPTICALsample* displays a bias towards high values of e . Using e as selection parameter, as in the combination $(u - r, \log(r_e), e)$, gives rise to a bias in the distribution of e for the selected sample as visible in Fig. 6, causing the selection provided by $(u - r, \log(r_e), e)$ to largely coincide with the GALAXY ZOO defined spiral sample for the *OPTICALsample*. This bias may also give rise to the agreement between the $NUV - r$ colour distributions of the GALAXY ZOO defined sample and the $(u - r, \log(r_e), e)$ selection in Fig. 5 (i.e. for the *OPTICALsample*), which extend to redder colours than the other selections, as NUV emission from highly inclined galaxies will be strongly attenuated, more so than in optical bands (e.g., Tuffs et al. 2004). In

Table 8. Purity, completeness, bijective discrimination power, and contamination for combinations of three parameters applied to *NAIRsample* using the GALAXY ZOO visual classifications (columns 3-6) and the independent classifications of Nair & Abraham (2010, columns 7-9). Completeness and bijective discrimination power are listed w.r.t. the *NAIRsample* ($P_{\text{comp,o}}$ and $P_{\text{bij,o}}$) and the *NUVNAIRsample* ($P_{\text{comp,n}}$ and $P_{\text{bij,n}}$). In the case of the independent classifications the contamination fraction is taken to be the complement of the purity (i.e. this includes sources with T-type = 99).

Parameter combination	N_{sel}	P_{pure}	GALAXY ZOO						Nair & Abraham (2010)			
			$P_{\text{comp,n}}$	$P_{\text{bij,n}}$	P_{cont}	$P_{\text{comp,o}}$	$P_{\text{bij,o}}$	P_{pure}	$P_{\text{comp,n}}$	$P_{\text{bij,n}}$	$P_{\text{comp,o}}$	$P_{\text{bij,o}}$
$(NUV - r, \log(n), \log(r_e))$	1879	0.864	0.745	0.644	0.047	0.553	0.477	0.915	0.681	0.623	0.504	0.461
$(NUV - r, \log(n), \log(M_*))$	1934	0.841	0.747	0.628	0.055	0.554	0.466	0.906	0.694	0.629	0.514	0.465
$(NUV - r, \log(n), \log(\mu_*))$	1564	0.878	0.630	0.553	0.033	0.467	0.410	0.943	0.584	0.551	0.432	0.408
$(NUV - r, \log(n), M_i)$	1906	0.839	0.735	0.617	0.055	0.545	0.457	0.902	0.681	0.615	0.504	0.455
$(NUV - r, \log(n), e)$	1299	0.856	0.511	0.437	0.038	0.379	0.324	0.928	0.478	0.443	0.354	0.328
$(NUV - r, \log(r_e), \log(M_*))$	1687	0.893	0.691	0.617	0.027	0.513	0.458	0.942	0.627	0.591	0.466	0.439
$(NUV - r, \log(r_e), \log(\mu_*))$	1713	0.891	0.701	0.624	0.025	0.520	0.463	0.941	0.636	0.599	0.473	0.445
$(NUV - r, \log(r_e), M_i)$	1770	0.884	0.718	0.635	0.034	0.533	0.471	0.928	0.648	0.602	0.482	0.447
$(NUV - r, \log(r_e), e)$	1705	0.908	0.711	0.645	0.014	0.527	0.479	0.956	0.643	0.615	0.478	0.457
$(NUV - r, \log(M_*), \log(\mu_*))$	1594	0.897	0.657	0.589	0.025	0.487	0.437	0.946	0.595	0.563	0.442	0.418
$(NUV - r, \log(M_*), M_i)$	1970	0.815	0.737	0.601	0.069	0.547	0.446	0.887	0.690	0.612	0.512	0.455
$(NUV - r, \log(M_*), e)$	1478	0.884	0.600	0.531	0.020	0.445	0.394	0.941	0.549	0.516	0.408	0.384
$(NUV - r, \log(mu_*), M_i)$	1647	0.888	0.672	0.597	0.029	0.498	0.442	0.943	0.613	0.578	0.455	0.429
$(NUV - r, \log(mu_*), e)$	1494	0.908	0.623	0.566	0.017	0.462	0.420	0.967	0.570	0.551	0.424	0.410
$(NUV - r, M_i, e)$	1467	0.883	0.595	0.526	0.022	0.441	0.390	0.938	0.543	0.509	0.403	0.378
$(\log(n), \log(r_e), \log(M_*))$	1745	0.886	0.710	0.629	0.028	0.526	0.466	0.940	0.650	0.611	0.481	0.452
$(\log(n), \log(r_e), \log(\mu_*))$	1736	0.885	0.705	0.624	0.028	0.523	0.463	0.940	0.646	0.607	0.478	0.449
$(\log(n), \log(r_e), M_i)$	1757	0.874	0.705	0.617	0.042	0.523	0.457	0.923	0.642	0.593	0.475	0.438
$(\log(n), \log(r_e), e)$	1754	0.831	0.669	0.556	0.078	0.496	0.412	0.884	0.615	0.543	0.455	0.402
$(\log(n), \log(M_*), \log(\mu_*))$	1698	0.894	0.697	0.623	0.025	0.517	0.462	0.948	0.638	0.605	0.472	0.448
$(\log(n), \log(M_*), M_i)$	1695	0.820	0.638	0.523	0.069	0.473	0.388	0.895	0.601	0.538	0.445	0.398
$(\log(n), \log(M_*), e)$	1189	0.834	0.455	0.380	0.049	0.338	0.282	0.918	0.432	0.396	0.320	0.293
$(\log(n), \log(\mu_*), M_i)$	1694	0.888	0.691	0.614	0.021	0.512	0.455	0.950	0.638	0.606	0.472	0.449
$(\log(n), \log(\mu_*), e)$	1545	0.869	0.617	0.536	0.029	0.457	0.397	0.939	0.575	0.540	0.425	0.400
$(\log(n), M_i, e)$	1307	0.828	0.497	0.411	0.060	0.368	0.305	0.896	0.464	0.416	0.343	0.308
$(\log(r_e), \log(M_*), \log(\mu_*))$	1465	0.903	0.607	0.549	0.024	0.450	0.407	0.954	0.552	0.526	0.410	0.391
$(\log(r_e), \log(M_*), M_i)$	1567	0.886	0.637	0.564	0.036	0.473	0.419	0.936	0.579	0.542	0.430	0.403
$(\log(r_e), \log(M_*), e)$	1528	0.889	0.624	0.554	0.026	0.462	0.411	0.944	0.569	0.537	0.423	0.399
$(\log(r_e), \log(\mu_*), M_i)$	1567	0.880	0.633	0.557	0.041	0.470	0.413	0.934	0.577	0.539	0.429	0.400
$(\log(r_e), \log(\mu_*), e)$	1536	0.896	0.632	0.566	0.022	0.469	0.420	0.951	0.577	0.548	0.428	0.407
$(\log(r_e), M_i, e)$	1450	0.870	0.579	0.504	0.044	0.430	0.374	0.916	0.524	0.480	0.389	0.357
$(\log(M_*), \log(\mu_*), M_i)$	1516	0.888	0.618	0.549	0.032	0.458	0.407	0.942	0.563	0.531	0.419	0.394
$(\log(M_*), \log(\mu_*), e)$	1556	0.894	0.639	0.571	0.021	0.474	0.423	0.951	0.584	0.555	0.434	0.413
$(\log(M_*), M_i, e)$	1154	0.792	0.420	0.332	0.074	0.311	0.246	0.885	0.403	0.356	0.299	0.265
$(\log(\mu_*), M_i, e)$	1548	0.897	0.637	0.571	0.023	0.473	0.424	0.946	0.578	0.547	0.429	0.406

contrast to the selection using $(u - r, \log(r_e), e)$, the other investigated parameter combinations show distributions which are more or less flat in e , also justifying the use of the GALAXY ZOO sample as a calibration sample.

Comparison of the distribution of the parameters in the selections applied to the *OPTICALsample* with those of the galaxies classified as spirals in the *NAIRsample* using the classifications of Nair & Abraham (2010), shows a systematic difference in the distributions of the parameters between these samples. Overall, the spiral galaxies in the *NAIRsample* are more weighted towards redder $NUV - r$ and $u - r$ colours, as well as towards larger values of $\log(M_*)$ and $\log(\mu_*)$, and brighter i -band absolute magnitudes. Furthermore, the distributions of $\log(n)$ and $\log(r_e)$ are weighted towards larger values of n and lower values of r_e , respectively. The observable differences are largely consistent with the bright *NAIRsample* (g' -band $\text{mag} \leq 16$) being more weighted towards large spirals which, on average, are more massive and redder than lower mass

spiral galaxies. Furthermore, they often also have more dominant bulges, increasing the values of n and decreasing those of r_e , while simultaneously decreasing the value of e , in agreement with the observed distributions. However, the differences may also be due, in part, to the fact that the cell-based selection misses regions of parameter space which are sparsely populated by spirals and in which they do not represent the dominant galaxy population. Nevertheless, Fig. 6 shows that the selections using combinations of three parameters trained on the GALAXY ZOO visual classifications of the *OPTICALsample* perform well at recovering the *NAIRsample*.

Fig. 7 shows the parameter distributions for the combinations applied to the *NUVsample* (we make use of $(NUV - r, \log(r_e), e)$ instead of $(u - r, \log(r_e), e)$). The results of applying the combinations to the *NUVsample* are nearly identical to those obtained for the *OPTICALsample*. However, the use of NUV preselection does bias the selected

galaxy populations towards bluer objects as can be seen in the shift of the distributions of the $u - r$ and to lesser extent the $NUV - r$ colour, between Figs. 5 & 7. The use of NUV preselection and $NUV - r$ colour also slightly lessens the bias against sources with low values of e selected using the combination $(NUV - r, \log(r_e), e)$, rendering the distribution in e of this selection flatter than that of the GALAXY ZOO defined sample. The overall similarity to the results obtained for the optical samples show that the requirement of an NUV detection itself is only mildly influencing the selections.

4.3.2 T-type and H α equivalent width as independent observables

Although the agreement between the parameter distributions of the visually defined samples and the selections is very good, the fact that a bias towards bluer $u - r$ and $NUV - r$ colours is discernible, and that the selections slightly favour lower values of $\log(n)$ and $\log(\mu_*)$ and higher values of $\log(r_e)$, raises the possibility that the selections may nevertheless be biased against a subclass of spirals.

T-type distributions of the *NAIRsample*

In order to investigate to what extent such a bias may be present, we first make use of the distributions of the T-type classifications of Nair & Abraham (2010). Fig. 8 shows the normalized distributions of the T-type values for the four selections, compared with the distributions of the visually classified spiral samples (GALAXY ZOO: black, Nair & Abraham (2010):grey). The distribution of the T-types of galaxies classified as spirals by the selection is shown in green, while the magenta line shows the T-type distributions of the GALAXY ZOO defined reliable spirals located in spiral cells following the selection. For the *NAIRsample* the GALAXY ZOO classifications (black solid line) appear moderately biased against early type spirals (mainly against Sa, and less against Sa/b). The selections based on the combinations of three parameters (green line) display a similar, but more pronounced bias, favoring spiral galaxies of type Sa/b, Sb and later, underscoring by the stronger bias against early type spirals of GALAXY ZOO spirals in spiral cells (magenta line). Overall, the parameter based selections recover relatively more earlier type spirals than the GALAXY ZOO classifications, in line with the findings that a large fraction of the 'impurity' arises from spiral galaxies which fail to meet the $P_{CS,DB} \geq 0.7$ requirement. All combinations considered display very similar performance in terms of the relative fractions of galaxy types recovered, although the bias against Sa/b galaxies of the selections using the parameters colour, effective radius and ellipticity is slightly less pronounced than for the other parameter combinations which involve more structural information (the use of structural information may be more sensitive to the presence of a prominent bulge in early-type spirals).

T-type distributions of the *NUVNAIRsample*

Fig. 9 shows the resultant distributions of T-types for the

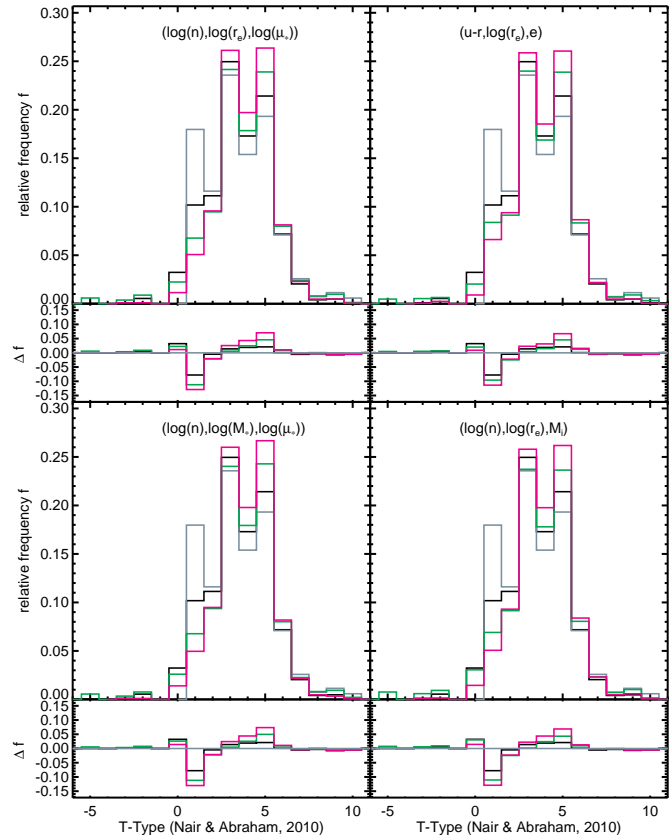


Figure 8. Distribution of T-types for galaxies in the *NAIRsample* classified as spirals based on the classifications of Nair & Abraham (2010) (gray), GALAXY ZOO (black), and the parameter combination listed top left (green). The T-type distribution of galaxies with $P_{CS,DB} \geq 0.7$ located in cells associated with spiral galaxies is shown in magenta. The inset panel below each distribution shows the distribution of the difference in relative frequency for this galaxy type relative to those of the Nair & Abraham (2010) classifications.

selections applied to the *NUVNAIRsample* (using $NUV - r$ rather than $u - r$). Overall, the results are very similar, with both the GALAXY ZOO classified spirals and the spirals selected by the parameter combinations being more weighted towards later type galaxies than the classifications of Nair & Abraham (2010). We note the fact that the *NUVNAIRsample* is more weighted towards earlier type spirals than the *NAIRsample*.

H α Equivalent Width Distribution of the *NAIRsample* & *NUVNAIRsample*

A similar investigation of the possible bias against subclasses of spiral galaxies for the *OPTICALsample*, respectively for the *NUVsample*, is not possible, as these lack independent visual classifications and T-Types. However, to at least gain a qualitative insight into the possible biases for these larger samples, we make use of the distributions of H α equivalent width (EQW), an observable used neither in our classification nor in that supplied by GALAXY ZOO.

Based on H α EQW, galaxies are often divided into two main populations, 'line-emitting' galaxies (i.e. galaxies with

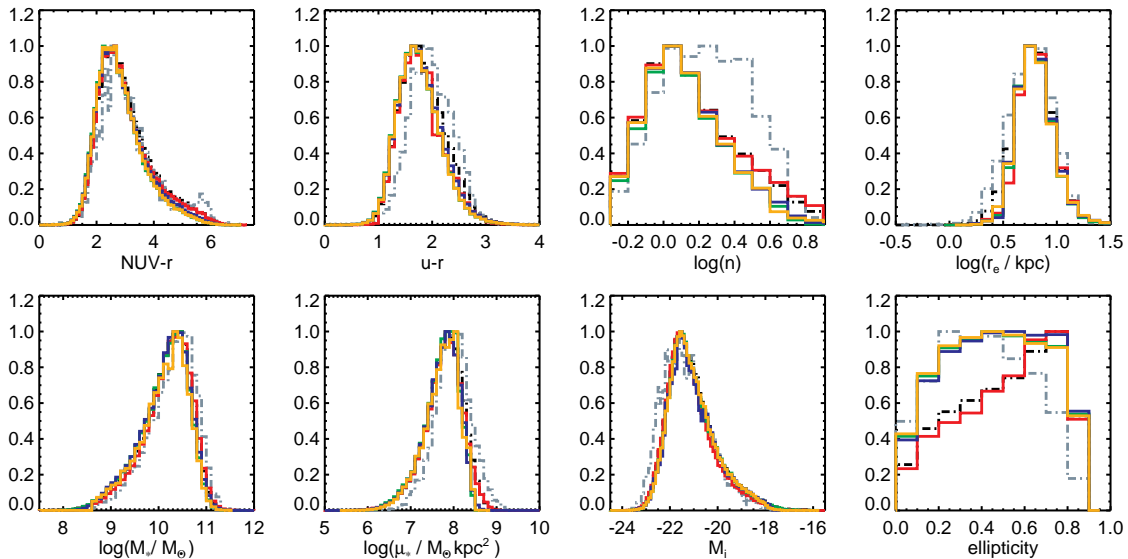


Figure 5. Normalized distribution of the suite of 8 parameters as recovered for all GALAXY ZOO reliable spirals in the *OPTICALsample* (black dashed) and the selections defined using $(u-r, \log(r_e), c)$ (red), $(\log(n), \log(r_e), \log(\mu_*))$ (green), $(\log(n), \log(r_e), M_i)$ (blue), and $(\log(n), \log(M_*), \log(\mu_*))$ (orange), applied to the *OPTICALsample*. The parameter distribution of spirals as defined by the classifications of Nair & Abraham (2010) in the *NAIRsample* is shown as a grey dash-dotted line.

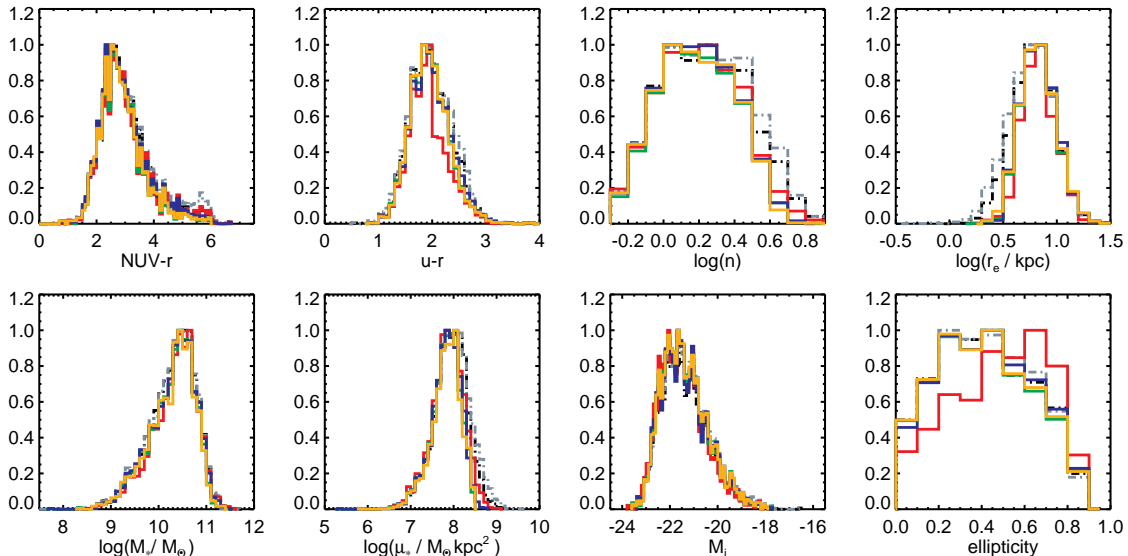


Figure 6. As Fig. 5 but for the *NAIRsample*.

non-negligible Balmer line emission, usually actively star forming) and passive galaxies (very little/no line emission, usually quiescent). In general, spirals tend to exhibit $H\alpha$ line emission (although a non-negligible fraction has very small $H\alpha$ EQWs indicative of passive systems), while early-type spirals are predominantly passive. Similarly, earlier type spirals often have smaller values of $H\alpha$ EQW than later types (see e.g., Robotham et al. 2013. for a detailed discussion).

Figs. 10 & 11 show the distributions of $H\alpha$ EQW for

the *NAIRsample* and *NUVNAIRsample*, respectively. The distribution of the samples defined using the classifications of Nair & Abraham (2010) is again shown in gray, with that of the sample defined by GALAXY ZOO in black. In both cases the GALAXY ZOO defined sample is weighted more towards intermediate values of $H\alpha$ EQW with respect to the classifications of Nair & Abraham (2010), showing evidence of a bias against low values of $H\alpha$ EQW as well as, to a lesser extent, against the highest values. The distributions of $H\alpha$ EQW of the samples defined by the

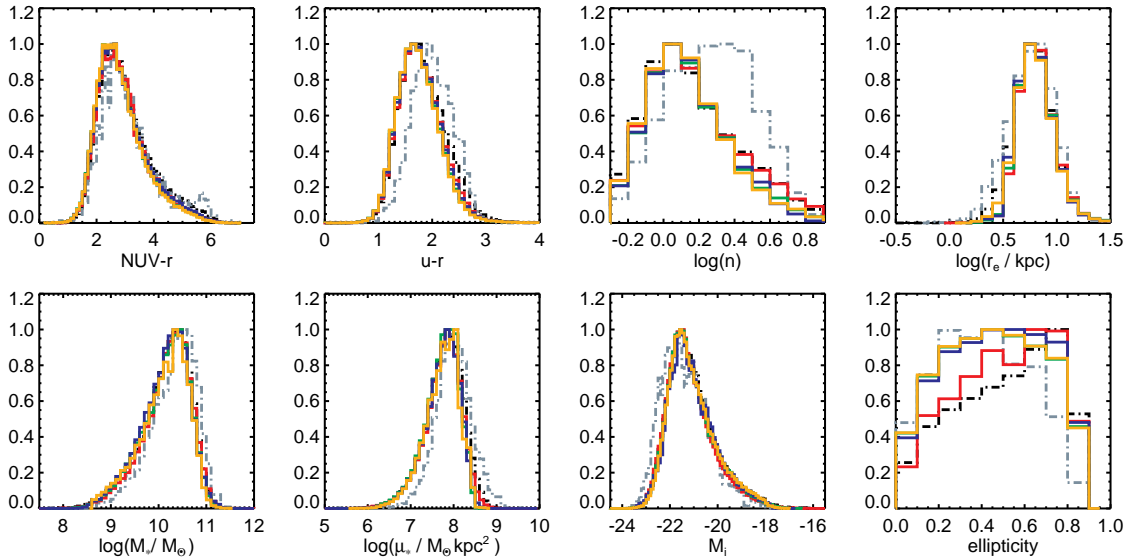


Figure 7. Normalized distribution of the suite of 8 parameters as recovered for all GALAXY ZOO reliable spirals in the *NUVsample* (black dashed) and the selections defined using $(NUV - r, \log(r_e), e)$ (red), $(\log(n), \log(r_e), \log(\mu_*))$ (green), $(\log(n), \log(r_e), M_i)$ (blue), and $(\log(n), \log(M_*), \log(\mu_*))$ (orange), applied to the *NUVsample*. The parameter distribution of spirals as defined by the classifications of Nair & Abraham (2010) in the *NUVNAIRsample* is shown as a grey dash-dotted line.

selections (green) all display a similar, yet more pronounced bias against low values of H α EQW. The selections, with the exception of $(u - r, \log(r_e), e)$, all also appear weighted against the highest values of H α EQW. These biases against low values of H α EQW may be considered to be consistent with the distributions of the T-types in the samples, with the selections favoring later type spirals.

In summary, we find that the GALAXY ZOO classifications display a simultaneous mild bias against early type spirals and systems with low values of H α EQW for the *NAIRsample* and *NUVNAIRsample*, and that this bias is slightly more pronounced for the parameter combination based selections.

H α Equivalent Width Distribution of the *Optical-sample* & *NUVsample*

Bearing this mild simultaneous bias in mind, we consider the distributions of H α EQW for parameter combinations as applied to the *OPTICALsample* and the *NUVsample*, shown in Figs. 12 & 13, respectively.

The samples selected by the same parameter combinations as previously applied to the *NAIRsample* display a bias against low values of H α EQW when applied to the *OPTICALsample*, similar to that observed for their application to the *NAIRsample*. Overall, all the considered parameter combinations recover the peak in the H α EQW corresponding to star-forming galaxies well, with high values of H α EQW being only minimally favored with respect to the GALAXY ZOO defined sample. However, all selections display a bias against very low values of H α EQW, least so for the combination $(u - r, \log(r_e), e)$. The general trends in the distributions of H α EQW appear very similar to those identified for the selections applied to the *NAIRsample*, hence we expect that the selections applied to the *OPTICALsample* will also

exhibit a similar bias towards later type spirals.

It is important to note the very good agreement between the H α EQW distributions of all reliable spirals in the *OPTICALsample* (black) and *NUVsample* (gray) shown in the panels of Fig. 13. This indicates that the NUV preselection itself is not introducing a strong bias. Nevertheless, NUV preselection does appear to lead to a slight bias against systems with low H α EQW, favoring high H α EQW systems. As for the *OPTICALsample* the selections applied to the *NUVsample* display a bias against low values of H α EQW, although the bias is reduced under NUV preselection. However, the parameter combinations are slightly more weighted towards high values of H α EQW than for the *OPTICALsample*. Overall, the trends in the H α EQW distributions are similar to those observed in the selections drawn from the *OPTICALsample*, the *NAIRsample*, and the *NUVNAIRsample*. Accordingly, we expect that the parameter based selections will be, to some extent, biased against early type spirals.

4.3.3 Redshift dependence of the spiral fraction

A final avenue of possible bias we address here, is the dependence of the performance of the selection on the distance/redshift of the sources. This is of particular interest, as the parameters with the best performance are largely structural or related parameters, e.g. $\log(n)$, $\log(r_e)$, $\log(\mu_*)$, and as such may depend on the resolution of the images in terms of physical sizes.

Over the time span corresponding to the redshift range of $z = 0 - 0.13$ we do not expect the distribution of galaxy morphologies to evolve in a significant manner (e.g. Bamford et al. 2009), hence the fraction of spirals should be approximately constant. However, as massive

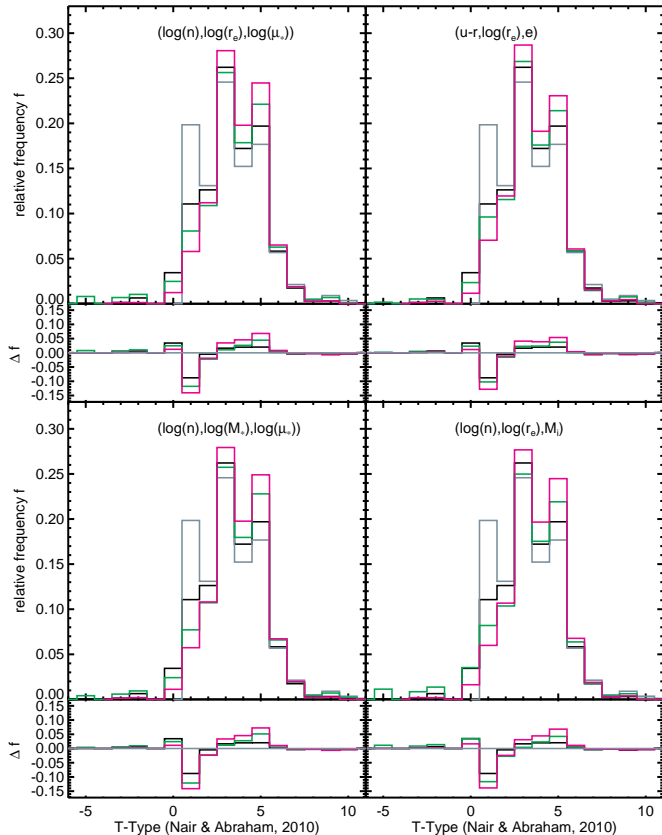


Figure 9. As Fig. 8 but for galaxies in the *NUVN AIR* sample.

bright galaxies are less likely to be spirals than less massive, fainter galaxies, this will only be the case for volume-limited samples. In Fig. 14 we show the fraction of galaxies classified as spirals by the parameter combinations $(u - r, \log(r_e), e)$, resp. $(NUV - r, \log(r_e), e)$ in the case of NUV-preselection, $(\log(n), \log(r_e), \log(\mu_*))$, $(\log(n), \log(r_e), M_i)$, and $(\log(n), \log(M_*), \log(\mu_*))$ for different volume-limited samples of galaxies. At top left we show the spiral fractions as a function of z for a volume-limited subsample of the *NAIR* sample extending to $z = 0.07$ (i.e. $M_g < 16 - D(z = 0.07)$, where $D(z)$ is the distance module and M_g is the absolute magnitude in the g band). We find that the spiral selections recovered by the parameter combinations (with the exception of $(u - r, \log(r_e), e)$) are flat in z , and are in good agreement with the z dependence of the spiral selection for this sample defined by the visual classifications of Nair & Abraham (2010) (black dash-dotted line). The middle left panel shows that the distribution of spirals selected from a volume-limited subsample of the *OPTICAL* sample extending to $z = 0.09$ (i.e. $M_r < 17.7 - D(z = 0.09)$, thus extending to fainter galaxies) is also largely flat in z for the selections not using colour as a parameter, while the bottom left panel shows a similar result for a volume-limited subsample of the *OPTICAL* sample extending to $z = 0.13$ (i.e. $M_r < 17.7 - D(z = 0.13)$, covering the full considered range in z). In the latter two panels, the dash-dotted black line indicates the z dependence of the spiral fraction as defined by the GALAXY ZOO visual classifications. The

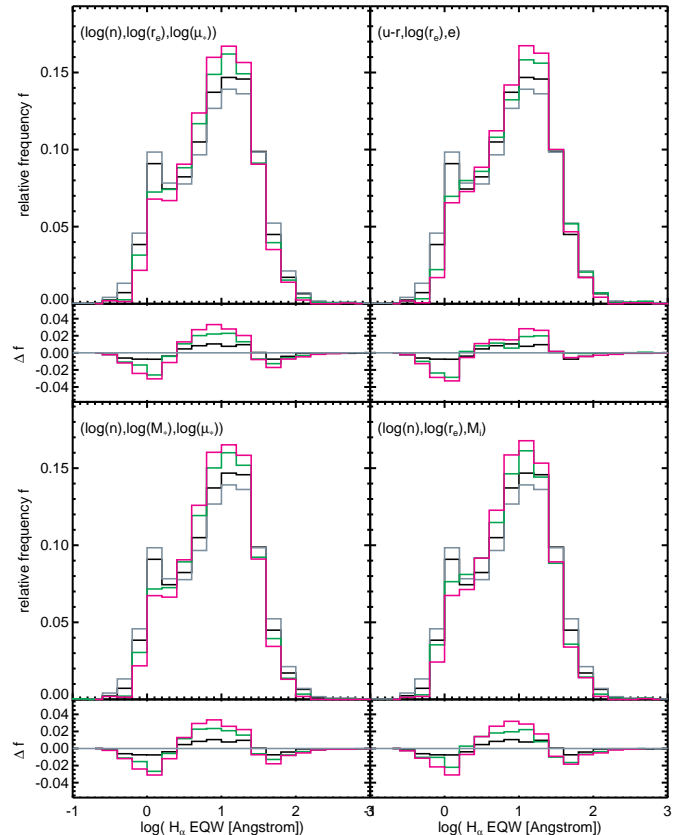


Figure 10. Distribution of $H\alpha$ EQW for galaxies in the *NAIR* sample classified as spirals based on the classifications of Nair & Abraham (2010) (gray), GALAXY ZOO (black), and the parameter combination listed top left (green). The $H\alpha$ EQW distribution of galaxies with $P_{CS, DB} \geq 0.7$ located in cells associated with spiral galaxies is shown in magenta. The inset panel below each distribution shows the distribution of the difference in relative frequency for each bin in $H\alpha$ EQW relative to that of the Nair & Abraham (2010) classifications.

decline in the spiral fraction is largely due to the certainty of the classifications decreasing with increasing z . If the assumption of a constant spiral fraction as a function of z is valid, these results may be seen to imply that for marginally resolved sources, the automatic cell-based non-parametric classification schemes may be superior to the GALAXY ZOO DR1 classifications.

The right hand panels of Fig. 14 show the results of applying the parameter combinations to NUV preselected samples, taking into account the UV sensitivity limits (i.e. with the additional requirement on the samples that $M_{NUV} < 23 - D(z_{sel})$, where z_{sel} is the limiting redshift of the sample). For volume-limited subsample of the *NUVN AIR* sample we find, as for the *NAIR* sample, that the spiral fraction is flat in z . For the other volume-limited samples, although the selections are largely flat in z , there is nevertheless an increase with increasing redshift. Notably, the spiral fraction of selections which only depend on parameters determined at long wavelengths (e.g. $(\log(n), \log(r_e), M_i)$), and which have spiral distributions which are flat in z without the requirement of an NUV

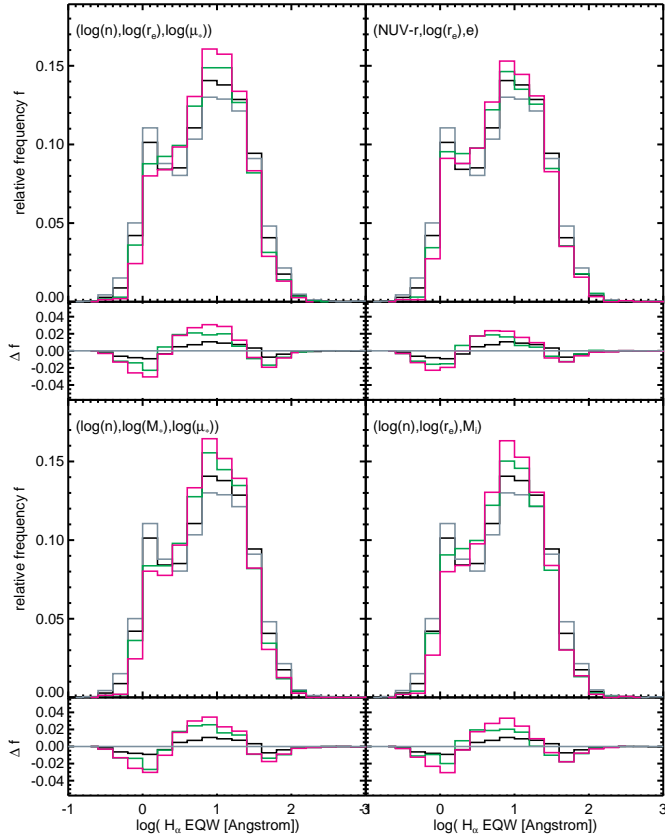


Figure 11. As Fig. 10 but for galaxies in the *NUVNIRsample*.

detection, also display an increase of the spiral fraction with z under NUV preselection. This can most readily be understood in the context of an evolution in the UV properties of the volume-limited samples of spirals considered, with an increasing fraction of spiral galaxies with NUV emission as a function of increasing redshift z . Such a scenario is consistent with the observed decline in star-formation rate density from $z = 1 - 0$ (e.g. Hopkins, McClure-Griffiths, & Gaensler 2008) and the increase in the population of quiescent galaxies in the mass range $M_* \gtrsim 10^{10} M_\odot$ over this redshift range (Moustakas et al. 2013, and references therein). The volume-limited samples considered will be dominated by galaxies in this mass range and be accordingly sensitive to such evolutionary effects.

We note that as the redshift range spans over a Gyr in lookback time, some evolution in the spiral fraction may be expected linked to a slight decline in the fraction of spirals with decreasing z , i.e. we do not expect a perfectly constant fraction of spirals. Nevertheless, the lack of any major dependence on the spiral fraction as a function of redshift, implies that no major redshift dependent biases are introduced into the selection when using combinations of three parameters with the non-parametric cell-based method, and that the method may even prove to be more reliable than visual classifications.

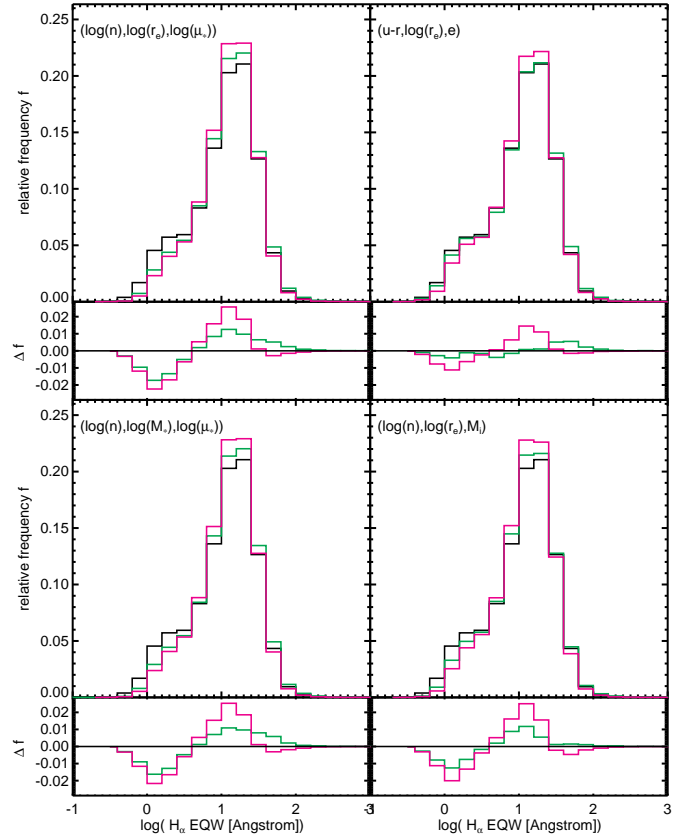


Figure 12. Distribution of $H\alpha$ EQW for galaxies in the *OPTICALsample* classified as spirals by GALAXY ZOO (black), and the parameter combination listed top left (green). The $H\alpha$ EQW distribution of galaxies with $P_{CS,DB} > 0.7$ located in cells associated with spiral galaxies is shown in magenta. The inset panel below each distribution shows the distribution of the difference in relative frequency for each bin in $H\alpha$ EQW relative to that of the GALAXY ZOO classifications.

5 COMPARISON WITH OTHER PROXIES

Using the cell-based method presented in Sect. 3 we have identified combinations of parameters including $\log(r_e)$, $\log(\mu_*)$, $\log(n)$, $\log(M_*)$, and M_i , in particular $(\log(n), \log(r_e), \log(\mu_*))$, $(\log(n), \log(r_e), M_i)$, and $(\log(n), \log(M_*), \log(\mu_*))$, to result in simultaneously pure and complete samples of spirals. These selections appear to be robust against redshift dependent biases, and to be largely unbiased in their parameter distributions, only displaying a slight bias against early type spirals. Accordingly, the cell-based method using these combinations appears well suited to selecting samples of spiral galaxies. In the following we investigate the contribution of the cell-based method to the demonstrable success, and compare its performance to a selection of widely used morphological proxies, as well as to a novel algorithmic approach based on support vector machines (Huertas-Company et al. 2011).

5.1 The Importance of the Cell-based Method

While the use of the parameter combinations in concert with the cell-based method presented in sect. 3 can lead to

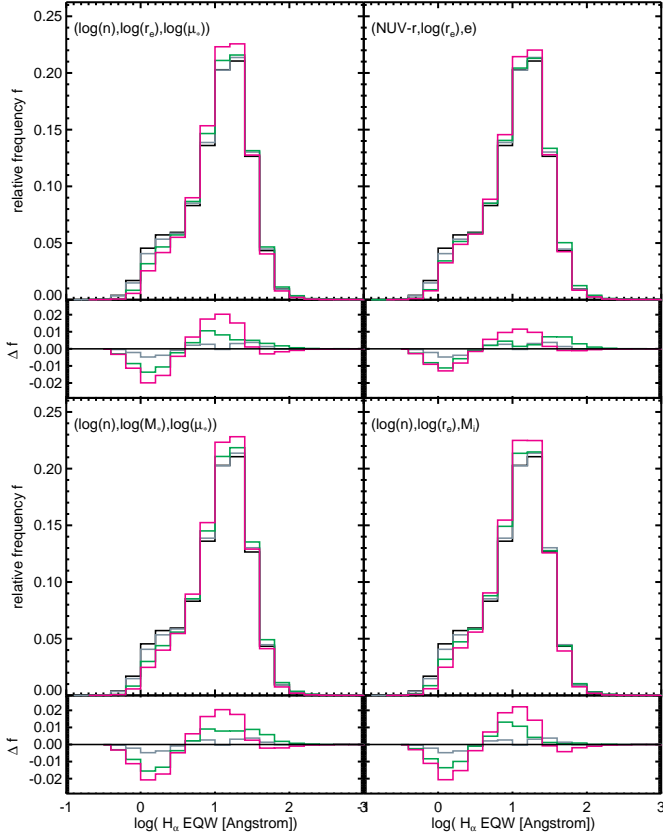


Figure 13. As Fig. 12 but for galaxies in the *NUVsample*.

simultaneously pure and complete samples of spiral galaxies, the use of the cell-based method requires a training sample, ideally of $\gtrsim 30k$ galaxies (cf. Fig. 2) In contrast to this, the advantage of simple hard cuts on parameters is that they require no (or much smaller) such calibration samples. In our investigations we have made use of a suite of parameters including ones traditionally used in the morphological classification of spirals (e.g. n), as well as novel parameters such as μ_* . In order to investigate to what extent the demonstrable success is due to the parameters used, and what the effect of the cell-based algorithm is, we have applied the combinations $(u - r, \log(r_e), e)$, $(\log(n), \log(r_e), \log(\mu_*))$, $(\log(n), \log(r_e), M_i)$, and $(\log(n), \log(M_*), \log(\mu_*))$ to the *OPTICALsample* and the *NAIRsample* using fixed boundaries derived by eye from the parameter distributions shown in Fig. 3. In this context we have chosen to treat galaxies with $u - r \leq 2.1$, $\log(r_e) \leq 0.65$, $e \geq 0.3$, $\log(n) \leq 0.4$, $\log(\mu_*) \leq 8.3$, $\log(M_*) \leq 10.7$, and $M_i \geq -22$ as spirals. The results tabulated in Table 9 show that the bijective discrimination power of the selections using fixed boundaries is much lower than when the same parameter combinations are used with the cell-based method. It is clear that the use of fixed boundaries entails a strong trade-off between purity and completeness. Although the parameter combinations $(u - r, \log(r_e), e)$, $(\log(n), \log(r_e), \log(\mu_*))$, and $(\log(n), \log(r_e), M_i)$ all attain high values of purity (even ~ 0.05 greater than with the cell based method), they, however, are highly incomplete, with completeness values $\sim 0.2 - 0.3$ less than attained with the cell-based method.

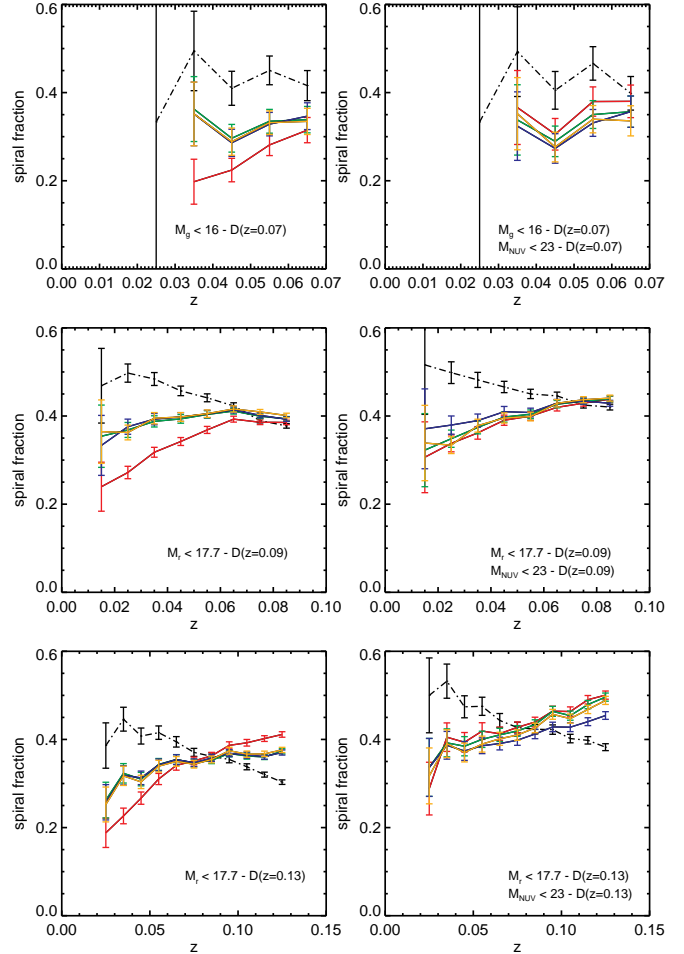


Figure 14. Spiral fraction as a function of redshift z in bins of width 0.01 for selections defined using $(u - r, \log(r_e), e)$ resp. $(NUV - r, \log(r_e), e)$ (red), $(\log(n), \log(r_e), \log(\mu_*))$ (green), $(\log(n), \log(r_e), M_i)$ (blue), and $(\log(n), \log(M_*), \log(\mu_*))$ (orange), respectively. The top left panel shows the results for the combinations applied to a volume-limited subsample of the *NAIRsample* (the selection criteria are indicated in each panel). The redshift dependence of the spiral fraction defined by the classifications of Nair & Abraham (2010) in the considered subsample is shown black as a dash-dotted line. Error bars indicate Poisson $1-\sigma$ uncertainties. The top right panel shows the same, but applied to a subsample of the *NUVNAIRsample* as defined in the panel. The middle and bottom left panels show the redshift dependence of the spiral fraction for the selection applied to two volume-limited subsamples of the *OPTICALsample* with the GALAXY ZOO defined reliable spiral fraction shown as a black dash-dotted line. The middle and bottom right panels show the same for the *NUVsample*.

The parameter combination $(\log(n), \log(M_*), \log(\mu_*))$, on the other hand, attains a completeness only ~ 0.07 less than the cell-based method, but with the purity of the selection reduced by ~ 0.1 . The high values of completeness, attained simultaneously to the high values of purity when making use of the parameter combinations together with the cell-based method, thus appear largely due to the flexibility of the boundaries given by the cell-based method.

Table 9. Purity, completeness, bijective discrimination power, and contamination for the combinations $(u - r, \log(r_e), e)$, $(\log(n), \log(r_e), \log(\mu_*))$, $(\log(n), \log(r_e), M_i)$, and $(\log(n), \log(M_*), \log(\mu_*))$ using fixed boundaries, applied to the *OPTICALsample* (columns 2-5) and the *NAIRsample* using the GALAXY ZOO visual classifications (columns 6-9) as well as the independent classifications of Nair & Abraham (2010, columns 10-12).

Parameter combination	<i>OPTICALsample</i>				<i>NAIRsample</i>						
	P_{pure}	P_{comp}	P_{bij}	P_{cont}	P_{pure}	P_{comp}	P_{bij}	P_{cont}	Nair & Abraham 2010		
$(u - r, \log(r_e), e)$	0.793	0.398	0.316	0.015	0.911	0.257	0.234	0.006	0.961	0.236	0.227
$(\log(n), \log(r_e), \log(\mu_*))$	0.794	0.567	0.450	0.006	0.934	0.487	0.455	0.007	0.976	0.442	0.431
$(\log(n), \log(r_e), M_i)$	0.782	0.507	0.396	0.007	0.922	0.372	0.343	0.013	0.965	0.339	0.327
$(\log(n), \log(M_*), \log(\mu_*))$	0.654	0.700	0.458	0.028	0.861	0.573	0.493	0.023	0.946	0.547	0.517

5.2 Comparison with widely used proxies

Having identified the cell-based method used with combinations of three parameters including $\log(r_e)$, $\log(\mu_*)$, $\log(n)$, $\log(M_*)$, and M_i , in particular $(\log(n), \log(r_e), \log(\mu_*))$, $(\log(n), \log(r_e), M_i)$, and $(\log(n), \log(M_*), \log(\mu_*))$, as a method to select simultaneously pure and complete samples of spirals we compare its performance to that of a selection of widely used morphological proxies, as well as to that of a novel algorithmic approach based on support vector machines (Huertas-Company et al. 2011).

Two well-known proxies for the general morphological type of a galaxy are the concentration index in the r band, defined as $C_r = \frac{R_{90,r}}{R_{50,r}}$ where $R_{90,r}$ and $R_{50,r}$ are the radii within which 90 resp. 50 per cent of the galaxy’s (petrosian) flux are contained, and the Sérsic index n , i.e., the index obtained for the best fit of a Sérsic profile (Sérsic 1968) to the galaxy’s light distribution. Strateva et al. (2001) suggest the use of the concentration index as a proxy for morphological classification with galaxies with $C_r < 2.6$ considered to be late-types/spirals, while Barden et al. (2005) suggest that galaxies with $n < 2.5$ can be considered to be late-types/spirals.

Alternatively, Baldry et al. (2004) have suggested a separation into blue and red galaxies which they equate to late- and early-types, based on a galaxies position in the $u - r$ colour vs. absolute r magnitude diagram, with the separator parameterized by a combination of a constant and a tanh function dependent on the absolute r band magnitude (their Eq. 11).

A different approach, also making use of two parameters, has been adopted by Tempel et al. (2011). They define a subvolume in the two dimensional space spanned by the SDSS parameters f_{dev} (i.e., the fraction of a galaxy’s flux which is fit by the de Vaucouleurs profile (de Vaucouleurs 1948) in the best fit linear combination of a de Vaucouleurs and an exponential profile) and q_{exp} (the axis ratio of the SDSS best fit exponential profile) associated with spiral galaxies and calibrated on visual classifications of SDSS galaxies in the Sloan Great Wall region (Einasto et al. 2010) and GALAXY ZOO.

Recently Huertas-Company et al. (2011) have published a catalogue of morphological classifications of SDSS DR7 spectroscopic galaxies based on support vector machines, which compare well with GALAXY ZOO classifications of the same sample. Similarly to GALAXY ZOO Huertas-Company et al. (2011) assign probabilities to the possible

galaxy classes, so that for the purposes of our comparison we have chosen to treat objects with a probability greater than 70 per cent of being a spiral as a spiral, analogously to our treatment the GALAXY ZOO sample⁹.

Table 10 shows the purity, completeness, and bijective discrimination power for the five morphological proxies discussed above as well as the three parameter combinations applied to the *OPTICALsample* and the *NAIRsample*. All morphological proxies, with the exception of that proposed by Tempel et al. (2011), attain values of completeness similar to, or larger than, that of the cell based method when applied to the *OPTICALsample*, although only the classification of Huertas-Company et al. (2011) achieves a completeness notably exceeding that of the cell-based method ($P_{\text{comp}} = 0.903$). However, these proxies fail to attain samples with a purity greater than 60 per cent when applied to the *OPTICALsample*, much lower than the value of ≈ 75 per cent achieved by the cell-based method, the exception again being the method of Tempel et al. (2011). As a result, the bijective discrimination power of these selections is lower than that achieved by the optimal combinations of three parameters, using the cell-based method, with only the method of Huertas-Company et al. (2011) attaining a comparable value of P_{bij} . However, the contamination by ellipticals introduced by the proxies considered is at least a factor 3 greater than that resulting from the cell based method.

Applied to the brighter *NAIRsample* the purity of the considered proxies increases notably, while the completeness slightly decreases. The purity of the selections resulting from the use of the considered proxies remains significantly lower than that achieved by the parameter combinations, both when using the GALAXY ZOO visual classifications as well as those of Nair & Abraham (2010), as can also be seen in the distributions of the T-types in the samples selected by the considered proxies (Fig. 15). The completeness, on the other hand, is greater than for the parameter based selections, so that the bijective discrimination power of the considered proxies is comparable to that of the parameter based selections when applied to the *NAIRsample*.

As can be seen in Fig. 15, the T-type distributions of the considered proxies display a bias towards later type

⁹ Huertas-Company et al. (2011) provide probabilistic morphological classifications for all but 311 of the sources in our sample

spirals very similar to that of the cell-based selections. However, the bias against Sa and Sa/b galaxies appears to be slightly less pronounced, with the relative frequency of early type galaxies being marginally higher for the samples recovered by the proxies than by the cell-based selections. On the other hand, the T-type distributions in Fig. 15 also show the considerably larger contamination by ellipticals not present in the cell based selections.

Considering the distributions of H α EQW for the samples obtained by these proxies applied to the *NAIRsample* as shown in Fig. 16 one finds that the samples recovered by the proxies (with the exception of the methods of Huertas-Company et al. 2011 and Tempel et al. 2011) display a bias towards sources with large values of H α EQW, considerably more so than the cell-based selections, with $\sim 10\%$ more of the sample consisting of high H α EQW sources than in the samples recovered by the cell-based method. This result is most pronounced for the samples selected by the concentration index, the Sérsic index and the method of Baldry et al. (2004). Similar but more pronounced results are obtained if one considers the distributions of H α EQW for the samples obtained by these proxies applied to the *OPTICALsample*, as shown in Fig. 17. In contrast, the selections based on the method of Tempel et al. (2011) and Huertas-Company et al. (2011) appear to be weighted more towards high *and* low values of H α EQW than the GALAXY ZOO reference and the selections based on the parameter combinations used in concert with the cell-based method.

Overall, we find that the selections resulting from the proxies are similar to, or more biased than, the selections based on the cell-based method, and are clearly more contaminated.

In conclusion, we thus find that for the purpose of selecting a pure, yet nevertheless largely complete, sample of spiral galaxies, not limited to the brightest galaxies, the use of the cell-based method presented in combination with one of the optimal parameter combinations is preferable over the investigated well-established proxies, and at least comparable to the sophisticated approach of Huertas-Company et al. (2011).

6 DISCUSSION

6.1 Choosing a parameter combination

Using the non-parametric cell-based method presented, we have successfully identified several combinations of three parameters which allow for an efficient and rapid selection of pure and simultaneously complete, largely unbiased samples of spiral galaxies. When applied to parent samples not limited to the brightest galaxies, these are superior in performance, in terms of bijective discrimination power and bias (e.g. in H α EQW), to the widely established simple morphological proxies investigated, such as the concentration index C_r , the Sérsic index n , and the division into red and blue galaxies. Furthermore, they are at least comparable in performance to the algorithmic approach using SVMs of Huertas-Company et al. (2011).

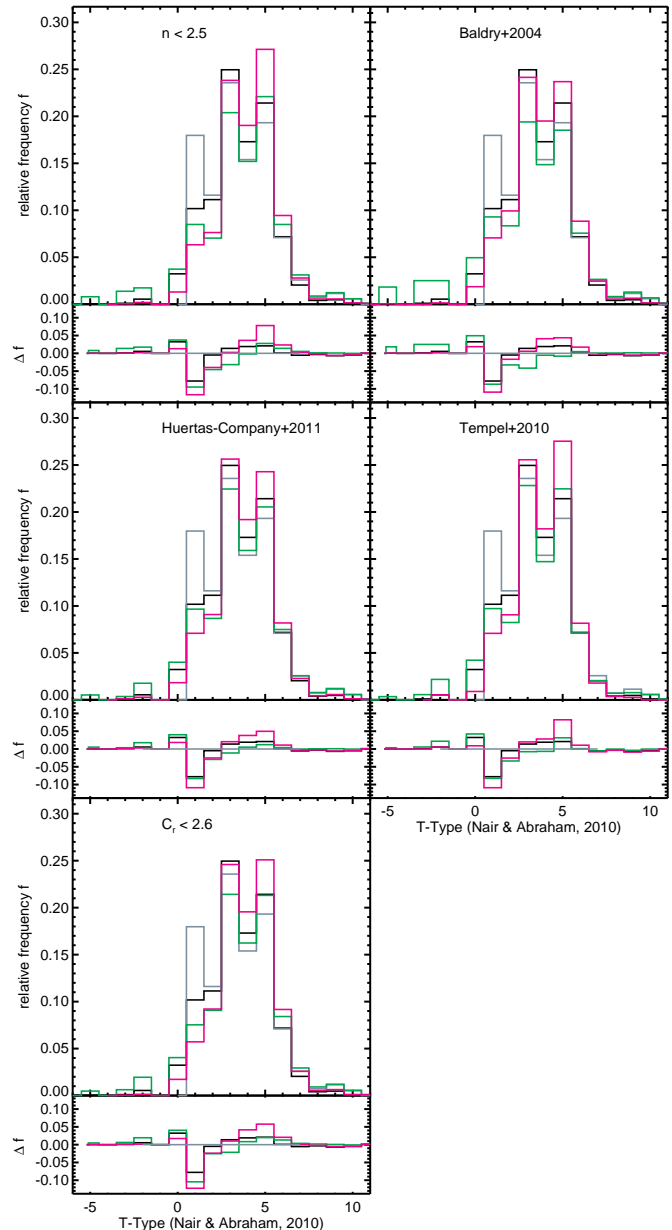


Figure 15. T-type distributions of the discussed selection methods applied to the *NAIRsample* indicated top left in each panel. The distribution of GALAXY ZOO spirals with $P_{CS,DB} > 0.7$ is shown in black. The distribution of sources selected by the method indicated is shown in green, while the the distribution of sources selected by the cell-based method with $P_{CS,DB} > 0.7$ is shown in magenta. The inset panel below each distribution shows the distribution of the difference in relative frequency for galaxy type relative to that of the Nair & Abraham (2010) classifications.

However, depending upon the effort required to obtain a given parameter, either in terms of data processing or acquisition, the ‘cost’ of parameters, and hence of parameter combinations, will vary. For example, a parameter combination including only quantities such as r_e , M_i , $u - r$, and e which can, at least for reasonably resolved sources, often be measured directly by **SExtractor** (Bertin & Arnouts 1996) is ‘cheaper’ than a combination involving parameters which require additional data reduction such

Table 10. Purity, completeness, bijective discrimination power, and contamination for other widely used morphological proxies, applied to the *OPTICALsample* (columns 2-5) and the *NAIRsample* using the GALAXY ZOO visual classifications (columns 6-9) as well as the independent classifications of Nair & Abraham (2010, columns 10-12). The values attained by the combinations $(\log(n), \log(r_e), \log(\mu_*))$, $(\log(n), \log(r_e), M_i)$, and $(\log(n), \log(M_*), \log(\mu_*))$ are shown for comparison.

Method	<i>OPTICALsample</i>				<i>NAIRsample</i>						
	P_{pure}	P_{comp}	P_{bij}	P_{cont}	GALAXY ZOO				NAIR & Abraham 2010		
	P_{pure}	P_{comp}	P_{bij}	P_{cont}	P_{pure}	P_{comp}	P_{bij}	P_{cont}	P_{pure}	P_{comp}	P_{bij}
$(\log(n), \log(r_e), \log(\mu_*))$	0.739	0.774	0.572	0.017	0.884	0.712	0.629	0.024	0.945	0.660	0.624
$(\log(n), \log(r_e), M_i)$	0.740	0.779	0.576	0.021	0.879	0.706	0.621	0.032	0.935	0.652	0.610
$(\log(n), \log(M_*), \log(\mu_*))$	0.731	0.773	0.565	0.019	0.885	0.707	0.626	0.024	0.946	0.657	0.621
Huertas-Company et al., 2011	0.588	0.903	0.531	0.077	0.806	0.836	0.673	0.054	0.898	0.802	0.720
Baldry et al., 2004	0.522	0.802	0.419	0.081	0.745	0.747	0.557	0.115	0.834	0.721	0.601
Tempel et al., 2011	0.648	0.411	0.266	0.078	0.786	0.387	0.304	0.064	0.896	0.380	0.340
$n < 2.5$	0.575	0.805	0.463	0.105	0.780	0.732	0.571	0.079	0.875	0.707	0.619
$C_r < 2.6$	0.547	0.762	0.417	0.105	0.810	0.750	0.608	0.066	0.896	0.715	0.641

as fitting Sérsic profiles using, e.g. GIM2D (Simard et al. 2002) or GALFIT (Peng et al. 2002)¹⁰. Similarly the relative ‘cost’ of additional NUV data is much higher than that of relying solely on optical pass-bands, as it involves the use of additional observational facilities.

Encouragingly, we find that various parameter combinations perform similarly well, allowing for a choice of parameter combination informed by both the envisioned science application as well as the relative ‘expense’ of the parameters used.

Overall, the most important parameters in selecting a sample of spiral galaxies are the effective radius $\log(r_e)$, the stellar mass surface density $\log(\mu_*)$, and the Sérsic index $\log(n)$. These parameters perform especially well in combination with the stellar mass or a tracer thereof (e.g. M_i). We find the combinations $(\log(n), \log(r_e), \log(\mu_*))$, $(\log(n), \log(r_e), M_i)$, and $(\log(n), \log(M_*), \log(\mu_*))$ to be those with the greatest bijective discrimination power when applied to the *OPTICALsample*. These are also amongst the most powerful under NUV preselection, although the combination $(NUV - r, \log(r_e), M_i)$ is comparably powerful. In the latter case, however, the selection appears to be driven by the parameters M_i and, in particular, $\log(r_e)$. In terms of relative ‘expense’ the combinations requiring NUV pre-selection are more ‘expensive’ than those applicable to the whole sample. Although the best-performing combinations all require Sérsic profiles to be fit, the cost is strongly ameliorated by the fact that only single Sérsic profiles are required.

Unsurprisingly, the ellipticity e proves to be an effective parameter, as only spirals seen edge-on appear strongly elliptical. In this sense, it even counters the bias against edge-on spirals, which can be introduced by using UV-optical colours as selection parameters, as dusty edge-on spirals may drop out of a colour selection due to attenuation of their UV emission. However, selections using e as a parameter are strongly biased against any spirals seen

approximately face-on, respectively *not* edge-on. Thus, while the observed ellipticity represents a powerful criterion for selecting a pure sample of spirals and has a low relative cost, it leads to generally less complete samples, which are strongly biased towards edge-on systems.

Although our results indicate that simple structural parameters derived at longer wavelengths are efficient at selecting spirals, the combinations $(NUV - r, \log(r_e), M_i)$, and to a lesser extent $(u - r, \log(n), \log(r_e))$, indicate that UV/optical colours linked to younger stellar populations do provide valuable information for selecting spiral galaxies. As mentioned above, however, use of UV-optical colour as a parameter can lead to biases in the selection. Dust in spirals will cause galaxies seen edge-on to appear very red, hence, the use of a UV-optical colour can bias the selection against these systems. Furthermore UV-optical colour selection can introduce a bias against any spirals which appear intrinsically red due to lack of star formation. This is the case both for the $u - r$ and $NUV - r$ colours. Finally, when using a colour as a parameter (in particular a UV colour) the possibility of different depths of photometry must be accounted for, i.e., the photometry in both bands must be deep enough to ensure that the entire range of colour normally attributed to the galaxy population is covered over the entire redshift range of the sample. Failure to do so will give rise to both additional incompleteness, as well as a colour bias in the resulting sample.

Depending on the science application for which the sample is intended, and on the availability of data different combinations may be optimal in selecting spiral galaxies. For example, using the combination $(\log(n), \log(r_e), M_i)$ would be appropriate to obtain a selection of spiral galaxies for a project aiming at investigating the total star formation rates of a large sample of spiral galaxies as derived from the UV. Such a selection would avoid a bias against quiescent systems, as would be introduced by using a NUV preselection or a UV-optical colour, while also guarding against any orientation biases which could arise if e was used as a selection parameter. Accordingly such a sample would be largely unbiased with respect to star formation characteristics. Another suitable combination for such an application would be $(\log(n), \log(r_e), \log(\mu_*))$, which is

¹⁰ Where high resolution imaging is available these codes themselves present a different method of automatic morphological classification, as they can perform multiple component fits which can be used to determine the morphological type of a galaxy. However, the requirements on resolution are severe and fitting multiple components is often not justified (Simard et al. 2011).

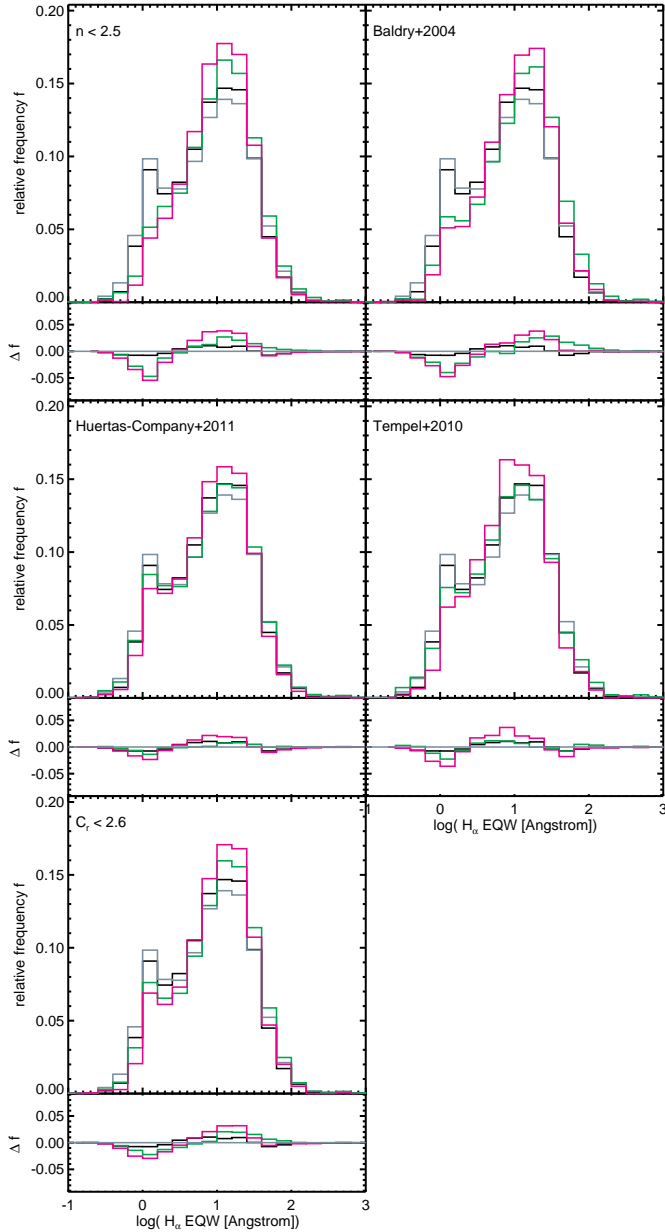


Figure 16. H_α EQW distributions of the discussed selection methods indicated top left in each panel applied to the *NAIRsample*. The distribution of GALAXY ZOO spirals with $P_{CS,DB} > 0.7$ is shown in black. The distribution of sources selected by the method indicated is shown in green, while the the distribution of sources selected by the method with $P_{CS,DB} > 0.7$ is shown in magenta. The inset panel below each distribution shows the distribution of the difference in relative frequency for each bin in H_α EQW relative to that of the Nair & Abraham (2010) classifications.

also largely independent of UV-optical colours¹¹

¹¹ The stellar mass estimate used in deriving μ_* does depend on an optical color, i.e the $g-i$ colour, however, this colour is linked mainly to intermediate age and old stellar populations. Given photometry of sufficient depth, the $g-i$ colour does not present a direct selection criterion but is only used in calculating the stellar mass, such that M_* and μ_* can be considered unbiased in terms

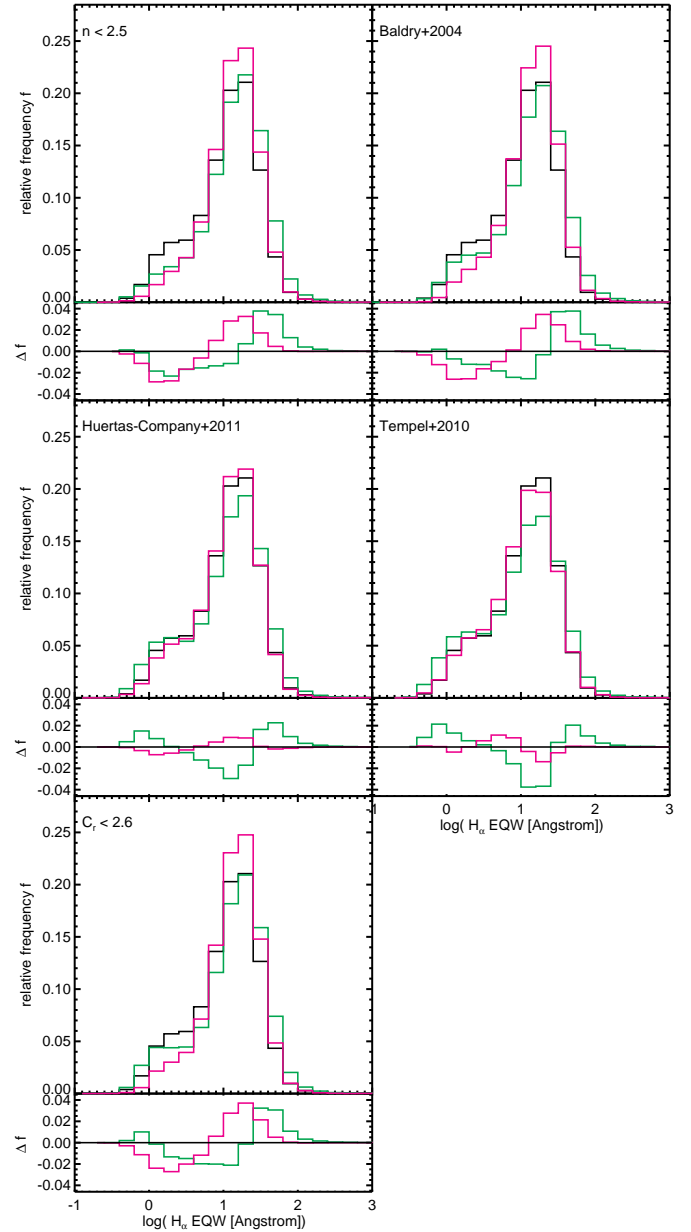


Figure 17. H_α EQW distributions of the discussed selection methods indicated top left in each panel applied to the *OPTICALsample*. The distribution of GALAXY ZOO spirals with $P_{CS,DB} > 0.7$ is shown in black. The distribution of sources selected by the method indicated is shown in green, while the the distribution of sources selected by the method with $P_{CS,DB} > 0.7$ is shown in magenta. The inset panel below each distribution shows the distribution of the difference in relative frequency for each bin in H_α EQW relative to that of the GALAXY ZOO classifications.

Conversely, however, a sample which required the greatest achievable purity should include both NUV preselection and e as a parameter. Thus, the selection can and should be adapted to the science case at hand, although the lack

of star-formation properties. Further more the stellar mass M_* derived in this manner is largely independent of dust attenuation (Bell & de Jong 2001; Nicol et al. 2011; Taylor et al. 2011).

of requirement of UV data allows the method to be easily applied to very large samples with minimum requirements on wavelength coverage.

6.2 The physical basis for optical proxies

As discussed in Sect. 6.1, we find that the most important parameters in selecting spirals are the effective radius $\log(r_e)$, the stellar mass surface density $\log(\mu_*)$, and the Sérsic index $\log(n)$ in combination with the stellar mass or a tracer thereof (e.g. M_i). In addition e leads to very pure if incomplete selections. All these properties are derived in pass-bands normally associated with older stellar populations (g , r , and i), rather than with recent star formation. The success achieved by using parameters not obviously directly related to the young stellar population is remarkable and implies that the spiral and non-spiral population are more or less distinct in these parameters. While the success of e bases on the appearance in projection of spiral galaxies, that of $\log(r_e)$ and $\log(\mu_*)$, on the other hand, entails that the radial extent and in particular the ratio of mass to size of the old stellar population is distinctly different in spirals and ellipticals. Rotationally supported systems (i.e. spirals) appear to be significantly more extended than pressure supported systems (i.e. spheroidals/ellipticals) at a given stellar mass¹².

This is consistent with the notion that the stellar populations evolve via distinct evolutionary tracks for disks and spheroids, with the evolution of present day spirals thought to involve a smooth infall of gas and inside-out star formation, with merger activity restricted to minor mergers.

In contrast, ellipticals are thought to be the products of major mergers in which angular momentum is redistributed making the central system more compact (e.g., Bournaud, Jog, & Combes 2007, and references therein).

In light of our results we emphasize that parameters linked to the old stellar population of galaxies, normally not employed in the classification of spirals, may provide valuable information on the morphology of a galaxy. In particular the stellar mass surface density and/or the radial extent (together with another parameter, e.g. M_i) may be powerful due to the physically motivated characterization parameters.

6.3 Applicability of the method to other surveys

We have shown the cell-based method to work well for SDSS galaxies, in particular a subset of the SDSS spectroscopic sample. Hence we expect the method to be applicable to samples of similar depth and similar angular resolution, and thus be applicable to upcoming surveys similar to SDSS, e.g. SKYMAPPER (The Skymapper Southern Sky Survey; Keller et al. 2007). Many upcoming surveys (DES, VST

ATLAS, KiDS, and GAMA (Galaxy And Mass Assembly; Driver et al. 2011), as well as SDSS itself, however, extend to greater photometric depths than the sample used here.

To answer the question of how applicable the method is to other, deeper surveys we have used a sample consisting of the 50k r -band brightest galaxies in the *OPTICALsample* (i.e. $m_r < 16.48$) as a calibration sample and have subsequently classified the faintest 50k galaxies ($m_r > 17.24$) using the parameter combinations $(\log(n), \log(r_e), \log(\mu_*))$, $(\log(n), \log(r_e), M_i)$, and $(\log(n), \log(M_*), \log(\mu_*))$. The results are shown in Table 11, where we have included the results obtained using the calibration sample employed in sect. 4, as well as the results obtained using the widely used proxies discussed in sect. 5 for comparison. Using the bright subsample to classify the faint subsample we find that the selections are very complete, yet appear to be less pure than when classifying the entire *OPTICALsample*. However, this is largely due to a decrease in the certainty of the GALAXY ZOO classifications for sources which appear fainter as they predominantly lie at greater redshifts and are smaller and less resolved. This is underscored by the very low values of contamination achieved for the different combinations. The performance of the cell-based method remains easily superior to that of the simple proxies, achieving much greater purity and similar completeness. These results suggest that galaxy samples extending faintwards of the SDSS spectroscopic limit can also be classified using the method presented (cf. also Sect. 4.3.3).

Penultimately, the increased angular resolution and sensitivity of the upcoming surveys with respect to SDSS may allow the method to be extended to sources at higher redshifts than the current very local sample. A somewhat similar approach defining subspaces associated with early- and late-type galaxies using $U - V$ and $V - J$ restframe colours, calibrated using HST ACS imaging, has recently been proposed by Patel et al. (2012) for galaxies at $z \sim 0.9$. Our proposed method may also be helpful in selecting spirals at higher z , especially selections using parameters linked to the older stellar populations, as they would be more robust against the increasing occurrence of bursts of star formation at higher redshifts. Such a use of structural parameters would, however, demand imaging with spatial resolution similar to that attained by SDSS at low redshifts for large samples of galaxies, which may not be available until Euclid.

Finally we note that, due to the evolution of structural and photometric parameters, it will, in general, be necessary to recalibrate the method at higher z , and for new data sets with very different imaging/photometry (angular resolution/filters). In such a case a subset of the new data with visual classifications will be required as a training set for the cell-based method.

At this point we emphasize that the use of the parameter space discretizations supplied in Appendix A depends on the compatibility of the parameters with those used in this work. When using the discretizations provided, the reader is advised to check for any possible systematic offsets between his/her data and the data used in this work.

¹² This size dichotomy can be boosted further by the presence of dust in the disks, which can increase the apparent size of disks relative to the intrinsic size (Möllenhoff, Popescu, & Tuffs 2006; Pastrav et al. 2013a)

Table 11. Purity, completeness, bijective discrimination power, and contamination for the combinations $(\log(n), \log(r_e), \log(\mu_*))$, $(\log(n), \log(r_e), M_i)$, and $(\log(n), \log(M_*), \log(\mu_*))$ and the proxies discussed in sect. 5 applied to the faintest 50k galaxies in the *OPTICALsample*, i.e $m_r > 17.24$. The results are presented for calibrations of the cell based method using the brightest 50k galaxies in the *OPTICALsample* ($m_r < 16.48$), as well as for the calibration sample used in sect. 4. As no calibration is required for the proxies discussed in sect. 5 the results are only listed once.

Method	bright cal				all cal			
	P_{pure}	P_{comp}	P_{bij}	P_{cont}	P_{pure}	P_{comp}	P_{bij}	P_{cont}
$(\log(n), \log(r_e), \log(\mu_*))$	0.596	0.860	0.513	0.009	0.657	0.787	0.517	0.005
$(\log(n), \log(r_e), M_i)$	0.607	0.861	0.523	0.009	0.664	0.799	0.530	0.006
$(\log(n), \log(M_*), \log(\mu_*))$	0.602	0.844	0.508	0.009	0.647	0.781	0.506	0.006
Huertas-Company et al., 2011	0.477	0.934	0.446	0.078				
Baldry et al., 2004	0.434	0.825	0.358	0.098				
Tempel et al., 2011	0.549	0.551	0.302	0.071				
$n < 2.5$	0.478	0.866	0.414	0.066				
$C_r < 2.6$	0.432	0.808	0.349	0.112				

6.4 Applicability of the method to the selection of elliptical galaxies

The cell-based method presented here could, in principle, be adapted to identifying reliable samples of elliptical galaxies in an analogous fashion to that described for the identification of spirals. A certain population of the cells, dependent upon the requirements imposed, will not be assignable to either the spiral or the elliptical subvolume and will remain undefined. However, it is by no means clear, that the parameter combinations which perform best at selecting a pure and complete population of spirals will do the same for ellipticals. As our focus has been to identify a method of reliably selecting spirals, we do not further discuss the selection of ellipticals. We note, however, that it would be straight-forward to implement and optimize such a method. We have also supplied the elliptical fractions and relative errors for the three discretizations supplied in appendix A.

6.5 Application to checks of probabilistic parametric methods

The use of parametric methods, such as linear discriminant analysis for example, in classifying galaxies is attractive, as these methods are capable of assigning a probabilistic classification to the morphology of a galaxy, rather than a binary one such as that presented here, which will suffer from contamination due to quantization effects. Furthermore, as also discussed in section 3, calibrating the cell based method requires substantial samples of galaxies with visual classifications, while the training sets for parametric methods can be smaller. However, the applicability of such a parametric method depends on the probability distributions of galaxy properties conforming to the assumed parameterization, which may not be the case. Obviously, a strength of the non-parametric method presented in this work is that it removes such biases arising from assumptions about the correct parameterization.

We suggest, that the non-parametric method presented here can also be used to investigate the performance of parametric methods. If the results of both approaches are in reasonable agreement it may be possible to confidently em-

ploy the parametric method to selecting samples, relaxing the required size of a putative calibration sample. A further investigation into the performance of multi-parameter morphological classifications using linear discriminant analysis and the cell-based method presented here as a comparison will be presented in a companion paper (Robotham et al., in prep.).

7 APPLICATION TO THE STELLAR MASS - SPECIFIC STAR FORMATION RATE RELATION FOR SPIRAL GALAXIES

As an application of the cell-based technique for selecting spiral galaxies we use it to rederive the empirical scaling relation between the specific star-formation rate and the stellar mass (the $\psi_* - M_*$ relation) for this class of objects. Previous derivations of the $\psi_* - M_*$ relation have used galaxy samples sensitive to star formation properties in their definition, thus potentially biasing the obtained results. A further factor influencing the derivation of the $\psi_* - M_*$ relation is the attenuation of stellar emission from the galaxy due to its dust content, which introduces a large component of scatter, as well as potentially of bias, into the relation. Here we capitalize on the selection of a relatively pure sample of galaxies of known disk-like geometry, by applying a radiation transfer technique to correct for the attenuation of stellar emission by dust, utilizing the geometrical information (effective radii & axis ratio) of each galaxy. To this end, we utilize the method of Grootes et al. (2013), who have presented a method to obtain highly accurate radiation transfer based attenuation corrections on an object-by-object basis, using only broadband optical photometric observables not directly linked to star formation, in particular the stellar mass surface density. The method of Grootes et al. (2013), however, critically relies on the underlying radiation transfer model of Popescu et al. (2011) being applicable to the galaxies considered, and thus requires a clean sample of galaxies with disk geometry not hosting AGN.

7.1 The intrinsic ψ_* – M_* relation for morphologically-selected spiral galaxies in the local universe

Starting from the *OPTICALsample* we define a sample of spirals using the cell-based method and the parameter combination $(\log(n), \log(r_e), M_i)$ and impose a redshift limit of $z = 0.05$. As shown by (e.g. Taylor et al. 2011), the SDSS with a limiting depth of $r_{petro,0} = 17.77$ is $\gtrsim 80\%$ complete for $M_* \gtrsim 10^{9.5} M_\odot$ to this redshift. The sample considered thus represents a volume-limited sample for this mass range. The sample is further limited to objects with an NUV detection as well as those for which there is no UV counterpart to the SDSS galaxy in the preliminary GCAT MSC (Seibert et al., 2013 in prep.), excluding ambiguous multiple matches which would require flux redistribution. For the sources lacking an NUV counterpart, 3σ upper limits have been calculated. Finally, objects defined as AGN following the prescription of (Kewley et al. 2006) using the ratios of [NII] to H α and [OIII] to H β have been excluded. This results in a total of 9885 galaxies, 536 of which have no counterpart in the preliminary GCAT MSC. A visual inspection of a random selection of these non-detected sources finds that a large fraction ($\sim 50\%$) of these non-detections lie in the vicinity of bright stars or at the very edge of GALEX tiles, so may actually have an NUV counterpart. In the following, we therefore proceed by considering two samples: i) the entire selected sample of spiral galaxies, treating all nondetections as real non-detections, and ii) only the subset of spirals with an NUV counterpart, implicitly assuming that all non-detections actually possess an NUV counterpart, and can thus be discarded. By comparing the $\psi_* - M_*$ relation for the two samples, we will show that the effect of the NUV non-detections is negligible on the derivation of the $\psi_* - M_*$ relation.

For all spiral galaxies, we have corrected the observed UV photometry (detections and upper limits) for the effects of attenuation by dust using the radiation-transfer based method presented in Grootes et al. (2013), and have derived values of ψ_* from the de-attenuated UV photometry using the conversion factors given in Kennicutt (1998), scaled from a Salpeter (1955) IMF to a Chabrier (2003) IMF as in Treyer et al. (2007) and Salim et al. (2007). The required stellar masses have been derived as detailed in Sect. 2. Inclinations (required for the attenuation corrections alongside the effective radii) have been derived from the observed ellipticity as $i = \arccos(1 - e)$ and subsequently corrected for the effects of finite disk thickness as detailed in Sect. 3 of Driver et al. (2007), using an assumed intrinsic ratio of scale-height to semi-major axis of 0.12.

Fig. 18 shows the values of ψ_* as a function of M_* before and after correction for dust attenuation (middle and top panel, respectively), with the median in bins of 0.1 dex in M_* shown as large filled circles with the errorbars indicating the interquartile range in logarithmic scatter in each bin. Without attenuation corrections, the $\psi_* - M_*$ relation displays a mean logarithmic scatter¹³ of 0.70 dex (0.63 dex considering only NUV-detected sources) for the

volume-limited sample. A pure power-law fit to the median distribution of the uncorrected sample finds an index of $\gamma \approx -0.8$, but also shows that a pure power-law is only marginally suited to describing the distribution.

After applying attenuation corrections, we find that the mean logarithmic scatter is reduced to 0.48 dex (0.43 dex considering only NUV-detected sources). In addition to this large reduction in scatter, we find that the median $\psi_* - M_*$ relation for the volume-limited corrected sample is well represented by a pure power-law with an index of $\gamma \approx -0.5$ over the entire range in M_* , and that this power-law also provides a good parameterization of the relation at least down to $M_* = 10^9 M_\odot$. The exact value of the power-law index found using a linear regression analysis of the binwise median of ψ_* as shown in Fig. 18 is $\gamma = -0.50 \pm 0.12$. The quoted error has been derived using the interquartile scatter in each bin and represents a conservative estimate of the accuracy. There is no evidence for a break in the power-law over the full range of M_* considered, despite the use of a sample incorporating red, quiescent spirals not considered in previous studies.

Both for the corrected and uncorrected samples the median $\psi_* - M_*$ relation is largely invariant between the whole sample, and the subsample considering only NUV-detected galaxies, indicating that the true distribution of NUV detections and upper limits would provide similar results.

As the selection of spiral galaxies is purely morphologically based, the sample is capable of including very red and potentially passive spiral galaxies and should have a low contamination rate by ellipticals ($\sim 2\%$, see Sect. 4). However, one might expect the small number of ellipticals misclassified as spirals to have low values of ψ_* , which might affect the $\psi_* - M_*$ relation. To investigate to what extent the visible population of passive spirals is in fact a population of misclassified ellipticals, we have visually inspected a random sample of galaxies with NUV detections, $M_* \gtrsim 10^{9.5} M_\odot$, and $\log(\psi_*/\text{yr}^{-1}) \leq -11$ after correction for dust. Fifteen randomly selected such galaxies are shown in Fig. 19. All but two galaxies (top right panel and middle panel of second row) are clearly disk dominated spirals, showing that the large majority of the considered population appear to be disk-like galaxies. This serves as further validation of the cell-based selection technique, and implies that the derived $\psi_* - M_*$ relation is not biased by a large contamination of elliptical galaxies.

Conversely, even for the combination $(\log(n), \log(r_e), M_i)$ a slight bias against early type spirals remains, which could potentially affect the $\psi_* - M_*$ relation, in particular if a large fraction of the massive, red spiral population were missed by the cell-based selection method. To investigate this potential effect we begin by considering the early-type spirals in the *NAIRsample* (i.e. T-type > 3). We find 32% of the early-type spirals recovered from the *NAIRsample* using the cell-based method to be red ($u - r > 2.2$) and massive ($M_* > 10^{10.5} M_\odot$), compared to 38% red and massive galaxies amongst the

¹³ The mean logarithmic scatter is calculated as the difference between the quartiles of the distribution in ψ_* , averaged over 15

equal sized bins in M_* spanning $10^{9.5} M_\odot \leq M_* \leq 10^{11} M_\odot$, and weighted by the number of galaxies in each bin.

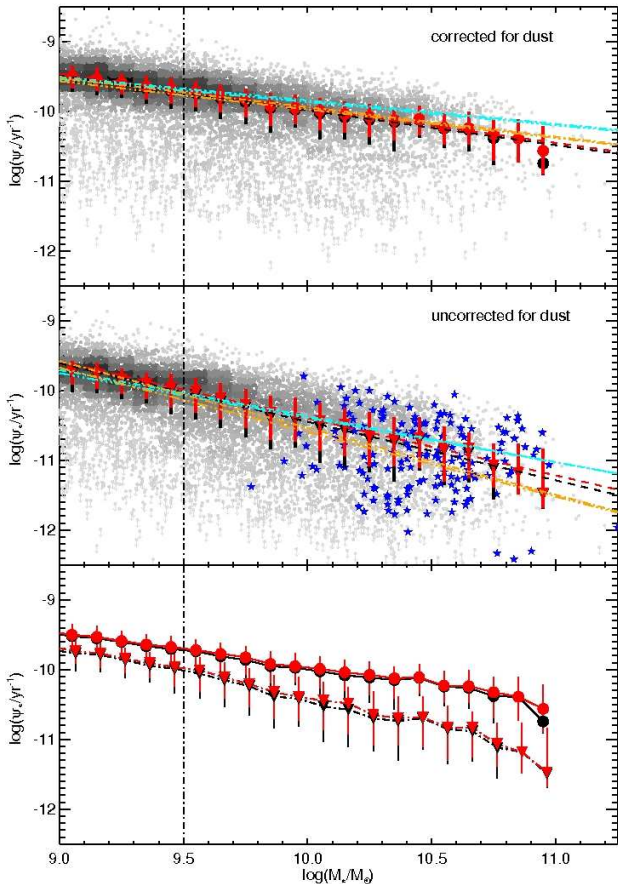


Figure 18. Specific star formation rate (ψ_*) versus stellar mass (M_*) for a sample of spiral galaxies selected using the cell-based method and the parameter combination $(\log(n), \log(r_e), M_i)$ and not hosting an AGN following the prescription of Kewley et al. (2006), with $z \leq 0.05$. Individual sources are plotted as filled circles with the grayscale color indicating the relative source density at their position in the $\psi_* - M_*$ plane. Values of ψ_* have been derived from NUV photometry as described in Sect. 7.1. Galaxies without an NUV counterpart in the GCAT MSC (Seibert et al., 2013 in prep.) are shown as $3\text{-}\sigma$ upper limits. The limiting stellar mass of $M_* \geq 10^{9.5} M_\odot$ above which the sample can be considered volume limited is indicated by a vertical dash-dotted line. The median value in bins of 0.1 dex in M_* is shown as large filled circles, with errorbars depicting the interquartile range in each bin. The medians and scatter for the whole sample are shown in black, while those of the sample considering only sources with NUV counterparts are shown in red. The top panel shows the distribution and median relations after radiation transfer based attenuation corrections following Grootes et al. (2013) have been applied, while the middle panel shows the uncorrected distribution and median relations. The black and red dashed lines in the top and middle panels show power-law fits to the median relation in the mass range $10^{9.5} M_\odot \leq M_* \leq 10^{11} M_\odot$, corresponding to the volume-limited sample. The bottom panel shows the corrected (circles) and uncorrected (stars) relations to facilitate a direct comparison of the slope and scatter before and after correction for dust attenuation. Spirals found to host an AGN following the prescription of Kewley et al. (2006) are shown by blue stars in the middle panel. The relations found using the prescription of Baldry et al. (2004) and a simple Sérsic index cut are shown in azure and orange respectively, with the dashed line showing the relation as determined from all galaxies considered, and the dash-dotted line indicating the relation as recovered using only the detected sources.

early-type-spirals NOT recovered by the cell-based method, implying that the early-type galaxies not recovered are not strongly weighted more towards massive red objects than those recovered. To judge the impact of the bias against early-type spirals on the $\psi_* - M_*$ relation, however, it is necessary to consider not only the early-type galaxies, but the entire populations of spiral galaxies in the *NAIRsample* recovered, respectively not recovered by the cell-based method. Overall, one finds that for galaxies classified as spirals by Nair & Abraham (2010) and recovered by the cell-based method with the parameter combination $(\log(n), \log(r_e), M_i)$ massive red galaxies constitute 15% of the sample, while massive red galaxies constitute 27% of the spirals not recovered by the cell-based method. This relatively small shift in weight at the massive red end ($\sim 12\%$) combined with the high completeness fraction ($> 65\%$) attained by the cell-based selection implies that the results obtained for the $\psi_* - M_*$ relation for spiral galaxies in the local universe are robust. Thus, although it is possible that the actual $\psi_* - M_*$ relation may still be slightly steeper, this further steepening will be small compared to the steepening to the $\psi_* \propto M_*^{-0.5}$ law found for the cell-based sample.

Finally, Fig. 18 shows the location of spiral galaxies hosting an AGN on the $\psi_* - M_*$ relation. Although the interpretation of the NUV emission of such sources as being indicative of their SFR is by no means secure, since the AGN can also significantly contribute to the NUV emission, we find that the ratio of NUV emission to stellar mass of spiral galaxies hosting optically identified AGN is not readily distinguishable from that of similar galaxies without an AGN. AGN host galaxies do, however, appear to be more massive than $\sim 10^{10} M_\odot$ as a rule, and display a larger scatter. Fig. 21 shows the locations of optically identified AGN in a sample of galaxies with the additional requirement of $H\alpha$ and $H\beta$ lines with $S/N > 3$ as described in Sect. 7.2. The similar distribution to that seen in Fig. 18 implies that the predominance of massive galaxies as AGN hosts is not a result of selection effects in the spectroscopy used.

7.1.1 The effects of sample construction: Comparison with the $\psi_* - M_*$ relations for colour-selected and Sérsic-index selected samples

We have previously argued and demonstrated, that the cell-based method of selecting pure and complete samples of spiral galaxies is capable of including quiescent spirals and is therefore well-suited to investigating the $\psi_* - M_*$ relation for a morphologically defined sample of spiral galaxies. In order to illustrate the effect that the choice of classification method has on the results derived for the $\psi_* - M_*$ relation and demonstrate the necessity of an adequate selection method, Fig. 20 shows the relation for galaxy samples drawn from the *OPTICALsample* and limited to $z \leq 0.05$ selected using the prescription of Baldry et al. (2004) (left) and the Sérsic index (right). Attenuation corrections have been applied using the method of Grootes et al. (2013) as previously described. The derived relations have also been overlaid in Fig. 18 for comparison. For

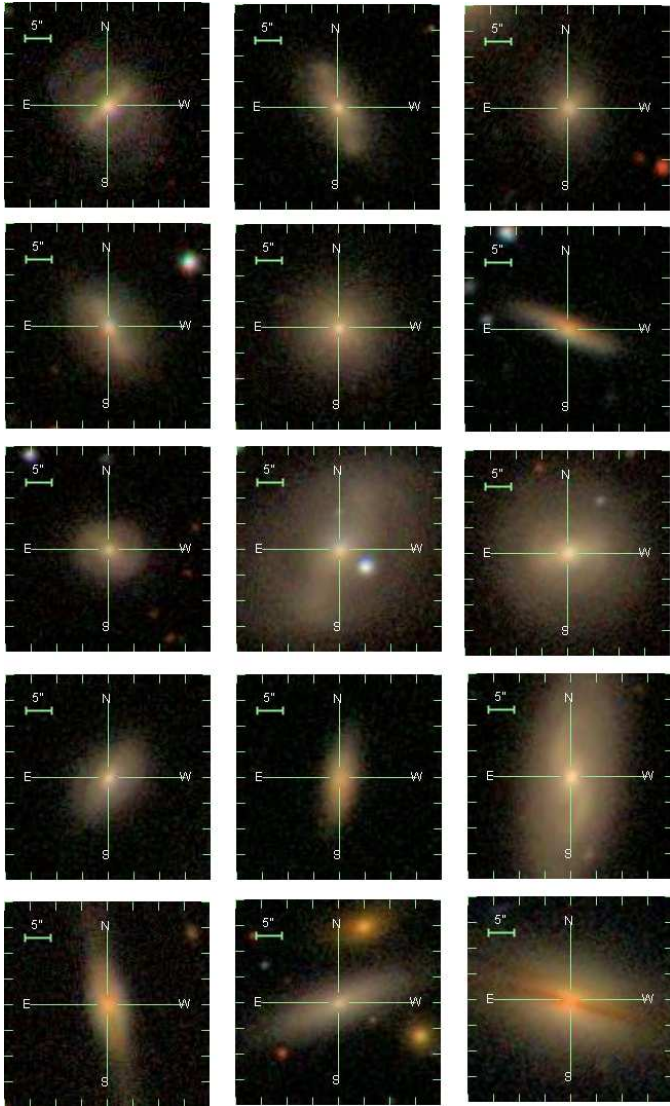


Figure 19. SDSS DR7 5 band images of a random selection of 15 spiral galaxies from the sample considered with an NUV counterpart in the GCAT MSC, $M_* \geq 10^{9.5} M_\odot$, and $\log(\psi_*/M_\odot \text{ kpc}^{-2}) \leq -11$ after attenuation corrections have been applied. All but two of the sources (top right and second row middle) display a disk-like morphology. The images have been retrieved using the SDSS Explore tool.

the sample selected following the method of Baldry et al. (2004) we find a power law index of $\gamma = -0.64 \pm 0.15$ before applying attenuation corrections and an index of $\gamma = -0.33 \pm 0.11$ after applying attenuation corrections. Both before and after correction a single power-law appears to be an adequate representation of the $\psi_* - M_*$ relation for this sample. Considering the scatter in the $\psi_* - M_*$ relation we find that the relation is tight both before and after applying attenuation corrections, with values of 0.52 dex interquartile and 0.40 dex, respectively.

Using the Sérsic index to select a sample of spiral galaxies, we find a power-law index of $\gamma = -0.93 \pm 0.15$ before and $\gamma = -0.41 \pm 0.14$ after applying attenuation corrections. The $\psi_* - M_*$ relation before correction, however,

is not well described by a single power-law. For the sample selected in this manner, the $\psi_* - M_*$ relation displays a scatter of 0.89 dex interquartile before applying attenuation corrections which is reduced to 0.59 dex interquartile by applying attenuation corrections.

For both these sample selection methods - by Sérsic-index and by colour - the power-law indices recovered are indicative of a shallower relation than for the cell-based selection. Given the similarity of the relations at lower stellar masses ($\sim 10^{9.5} M_\odot$) this appears to be largely due to a difference in the samples in the high stellar mass range, with the cell-based selection recovering more quiescent spirals. This is in line with the finding that the samples selected by these widely used proxies are more strongly biased towards sources with large values of $H\alpha$ equivalent width. It is particularly note-worthy that the colour based selection of Baldry et al. (2004) leads to a much shallower slope and a very low scatter, most likely due to the exclusion of quiescent galaxies.

This comparison demonstrates the care necessary in constructing galaxy samples for the purpose of statistical investigations and illustrates the suitability of the cell-based method of morphological classification for the investigation of the star formation properties of morphologically selected samples of spiral galaxies. A further discussion of the effects of sample construction on the $\psi_* - M_*$ relation is given in Sect. 7.3.

7.2 Dependency on attenuation corrections

In deriving the intrinsic $\psi_* - M_*$ relation for spiral galaxies in the local universe we have made use of the prescription for obtaining attenuation corrections given by Grootes et al. (2013) and the radiation transfer model of Popescu et al. (2011), as empirically calibrated on a sample of nearby spirals (see Xilouris et al. 1999; Popescu et al. 2000, 2004; Misiriotis et al. 2001) and incorporating corrections for the effects of dust on the perceived effective radii of disks by Pastrav et al. (2013b). In order to investigate to what extent the results obtained depend on the chosen method of deriving attenuation corrections, we compare the results obtained using the prescription of Calzetti et al. (2000) with those obtained using the method of (Grootes et al. 2013). These two correction methods, while both being empirically based, have a very different basis. Whereas the method of Grootes et al. (2013) is calibrated on a sample of local universe spirals with FIR-UV detections, the method of Calzetti et al. (2000) is calibrated on a sample of distant starburst galaxies, utilizing measurements of emission line fluxes. Furthermore, whereas, by virtue of its radiation transfer treatment, the method of Grootes et al. (2013) does not assume a fixed attenuation law in the UV/optical, this is the case for the method of Calzetti et al. (2000). This is potentially a critical factor when correcting for dust attenuation in spiral galaxies which lie on the transition between optically thick and thin systems, for which one expects a large range in the shape of the attenuation curve. Because of the requirement of emission line fluxes, the comparison must be based on a different sample, this time incorporating galaxies with $H\alpha$ and $H\beta$ line fluxes

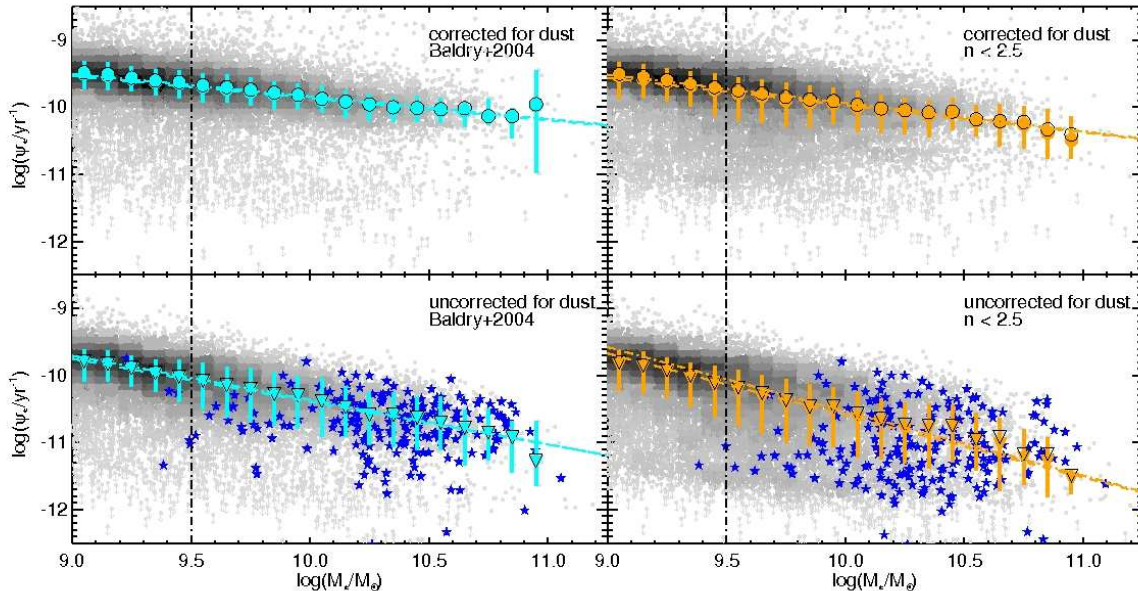


Figure 20. Specific star formation rate (ψ_*) versus stellar mass (M_*) for a sample of spiral galaxies selected using the method of (Baldry et al. 2004) (left top and bottom) and a simple Sérsic index cut (right top and bottom) and not hosting an AGN following the prescription of Kewley et al. (2006), with $z \leq 0.05$. Individual sources are plotted as filled circles with the grayscale color indicating the relative source density at their position in the $\psi_* - M_*$ plane. Values of ψ_* have been derived as previously detailed. Galaxies without an NUV counterpart in the GCAT MSC (Seibert et al., 2013 in prep.) are shown as $3\text{-}\sigma$ upper limits. The median values of ψ_* in bins of 0.1 dex in M_* are shown as large symbols, with errorbars depicting the interquartile range in each bin. The medians and scatter for the whole sample are shown in filled symbols and colour, while the medians of the sample considering only sources with NUV counterparts are shown as black outlines. The top panels show the distribution and median relations after radiation transfer based attenuation corrections following Grootes et al. (2013) have been applied, while the bottom panels show the uncorrected distribution and median relations. The dashed and dash-dotted lines in the top and bottom panels show power-law fits to the median relations in the mass range $10^{9.5} M_\odot \leq M_* \leq 10^{11} M_\odot$, corresponding to the volume-limited samples, with the dashed line showing the relation derived for the entire sample and the dash-dotted line showing the relation as derived only for the detected sources. Spiral galaxies found to host an AGN following the prescription of Kewley et al. (2006) are shown by blue stars in the bottom panels.

measured at $> 3\text{-}\sigma$, which effectively removes the population of red, quiescent galaxies. Thus, we select a sample of spiral galaxies with NUV counterparts, selected using the cell-based method with the parameter combination $(\log(n), \log(r_e), M_i)$, with $z \leq 0.05$, not hosting an AGN, and with $H\alpha$ and $H\beta$ line fluxes measured at $> 3\text{-}\sigma$ as the basis for the following comparison. We emphasize that the requirements on the spectroscopic information serve only to facilitate the comparison with the corrections obtained using the prescription of Calzetti et al. (2000).

Fig. 21 shows the distributions of ψ_* as a function of M_* without corrections for dust (top left) and with corrections obtained using the radiation-transfer based method of Grootes et al. (2013) (bottom left). The $\psi_* - M_*$ relation obtained using the method detailed in Calzetti et al. (2000) for correcting dust attenuation is shown in the top right panel. As in the case for the full sample incorporating red disks, the radiation transfer based corrections lead to a significant tightening of the relation, in this case reducing the mean logarithmic scatter from 0.58 dex to 0.37 dex. This lends confidence that the radiation transfer method also has the ability to predict the correct overall shift in the relation (see also discussion in Grootes et al. 2013, Sects. 5 & 6). By contrast, under the application of the corrections based on the Balmer decrement the scatter remains at 0.49 dex.

Nevertheless, the overall shift in the relation towards larger values of ψ_* by 0.3 dex on average is similar in both cases. This is a remarkable result bearing in mind the very different derivations of these methods and shows that the method of Calzetti et al. (2000) is indeed a very robust technique applicable to star-forming galaxies over a wide range of morphology and redshift.

Both correction methods lead to a similar, shallower dependence of ψ_* on M_* than found for the uncorrected relation, with the slope of the relation obtained using the prescription of Calzetti et al. (2000) being slightly shallower than that of the relation obtained by applying the method of Grootes et al. (2013). The power-law index found under both corrections is close to $\gamma \approx -0.4$. The flattening compared to the power-law index of $\gamma \approx -0.5$ found when applying the corrections of Grootes et al. (2013) to the full sample (as described in Sect. 7.1 and shown in Fig. 18) may be attributed to the exclusion of red, quiescent systems, which tend to be more massive, by the requirement of emission line flux measurements.

The main systematic difference between the two methods for dust corrections is that the relation based on the Calzetti et al. (2000) attenuation corrections shows an indication of a possible break in the power-law at $M_* \approx 10^{10.5} M_\odot$, not found when using the Grootes et al. (2013) attenuation corrections. The fact that the Grootes et al. attenuation

corrections significantly reduce the overall scatter in the relation, may imply that the break is actually not physical in nature, but rather may be an artifact of the application of the Calzetti et al. (2000) corrections to high mass spiral galaxies.

7.3 Comparison of the morphologically defined $\psi_* - M_*$ relation with previous determinations

Previous determinations of the $\psi_* - M_*$ relation have generally necessarily been restricted to galaxy samples encompassing the complete population of galaxies (e.g. Salim et al. 2007; Elbaz et al. 2007; Noeske et al. 2007), or to samples selected on the basis of colour or star-formation activity (e.g. Peng et al. 2010; Whitaker et al. 2012). As such, the $\psi_* - M_*$ relation has been defined in terms of a blue sequence, or more generally a sequence of star-forming galaxies, and has been contrasted with a red sequence, or more generally a sequence of non-star-forming galaxies (Peng et al. 2010, respectively Noeske et al. 2007; Whitaker et al. 2012). However, the more fundamental distinction may be the morphology of the galaxy. This is because, while rotationally supported galaxies can support an extended cold ISM which can support distributed star-formation, any extended ISM in a spheroid must be hot and tenuous if it is in virial equilibrium with the total mass distribution as traced by the stars, in which case it would be expected to be inefficient in forming stars. To constrain processes driving star-formation in galaxies, it is therefore instructive to establish the $\psi_* - M_*$ relation for a pure disk sample.

We have found this relation to be a relatively tight (0.42 dex mean logarithmic interquartile range, corresponding to 0.31 dex $1-\sigma$ for a normal distribution) power-law with an index of $\gamma = -0.5 \pm 0.12$, with no indication of a cut-off at high stellar mass. This result shows that the phenomenon of down-sizing¹⁴ is also exhibited by a morphologically pure sample of disk galaxies, and is not just due to an increasing fraction of spheroids with increasing stellar mass in the general galaxy population.

The lack of an obvious turn-off in the $\psi_* - M_*$ relation for spirals, despite the inclusion of red quiescent spirals, suggests that if a mechanism exists to restrict the growth of spiral galaxies beyond the stellar mass range probed, such a mechanism must be accompanied by an abrupt transformation of galaxy morphology.

As outlined above, previous works addressing the $\psi_* - M_*$ relation have concentrated on the sequence of star-forming galaxies rather than a morphologically defined sample. For example Peng et al. (2010) make use of a $U - B$ color selection (their Eq. 2) akin to that of Baldry et al. (2004) investigated in Sect. 7.1 of this paper, applying it to a sample of SDSS galaxies with star formation rates derived from $H\alpha$ line measurements as provided by Brinchmann et al. (2004). These authors find a power law index of

$\gamma = -0.1$, much shallower than the relation found in this work. Similarly, Whitaker et al. (2012) find that for local universe star-forming galaxies selected using $U - V$ & $V - J$ restframe colors, selecting a blue subset of these galaxies results in a shallow slope similar to that of Peng et al. (2010). However, considering their full sample of star-forming galaxies Whitaker et al. (2012) find a steeper slope of $\gamma \approx -0.4$. Finally, Noeske et al. (2007) find a slope of $\gamma = -0.33 \pm 0.08$ for local universe galaxies with indications of on-going star-formation either in form of $24\mu\text{m}$ emission and/or $H\alpha$ emission.

The fact that these previously determined values of γ are all shallower than the relation found for a morphologically selected sample of spirals presented in this work, can be readily understood. By selecting actively star-forming systems, quiescent galaxies of similar morphology are excluded from the samples. As passive spirals tend to be more massive, on average, this leads to a flattening of the $\psi_* - M_*$ with respect to a morphologically defined, sample, as similarly argued by Whitaker et al. (2012) in the context of the result of Peng et al. (2010). Indeed, for the sample of spirals selected using the cell-based method with the combination $(\log(n), \log(r_e), M_i)$ and the additional requirement of $H\alpha$ and $H\beta$ detections, as used in Sect. 7.2, we find the $\psi_* - M_*$ relation to be well described by a single power-law with an index of $\gamma = -0.39 \pm 0.09$ and a scatter of 0.37 dex interquartile (0.27 dex $1-\sigma$, assuming a normal distribution), very similar to the results for star-forming galaxies as obtained by other authors as previously discussed.

Overall, we thus find that the $\psi_* - M_*$ relation for a morphologically selected sample of spiral galaxies with an index of $\gamma = -0.5$ is moderately steeper than that found for star-forming galaxies ($\gamma = -0.3 \dots -0.4$), likely due to the inclusion of the population of red passive spirals in our analysis. This only moderate increase in slope is not greatly surprising, as the majority of spiral galaxies are found to display star-formation activity.

8 SUMMARY AND OUTLOOK

We have presented a non-parametric cell-based method of selecting robust, pure, complete, and largely unbiased samples of spirals using combinations of three parameters derived from (UV/optical) photometry. We find that the parameters $\log(r_e)$, $\log(\mu_*)$, $\log(n)$, and M_i perform well in selecting simultaneously pure and complete samples, while the use of the ellipticity e leads to pure yet incomplete samples. These parameters, which are linked to older stellar populations, perform at least as well as selections using the $u - r$ colour or the $NUV - r$ colour after NUV preselection. The remarkable success/importance of these seldom utilized parameters is consistent with the expected contrast in the structural properties of rotationally supported systems (spirals) and pressure supported systems (ellipticals), in agreement with different evolutionary tracks for spiral and elliptical galaxies.

For a selection of combinations of three parameters, the cell-based method is superior to a range of (widely used) photometric morphological proxies, and comparable to the

¹⁴ Down-sizing describes the phenomenon that star-formation in the current epoch is biased towards low mass structures, in contrast to the sequence of growth in dark matter structures, which progresses from low mass to high mass

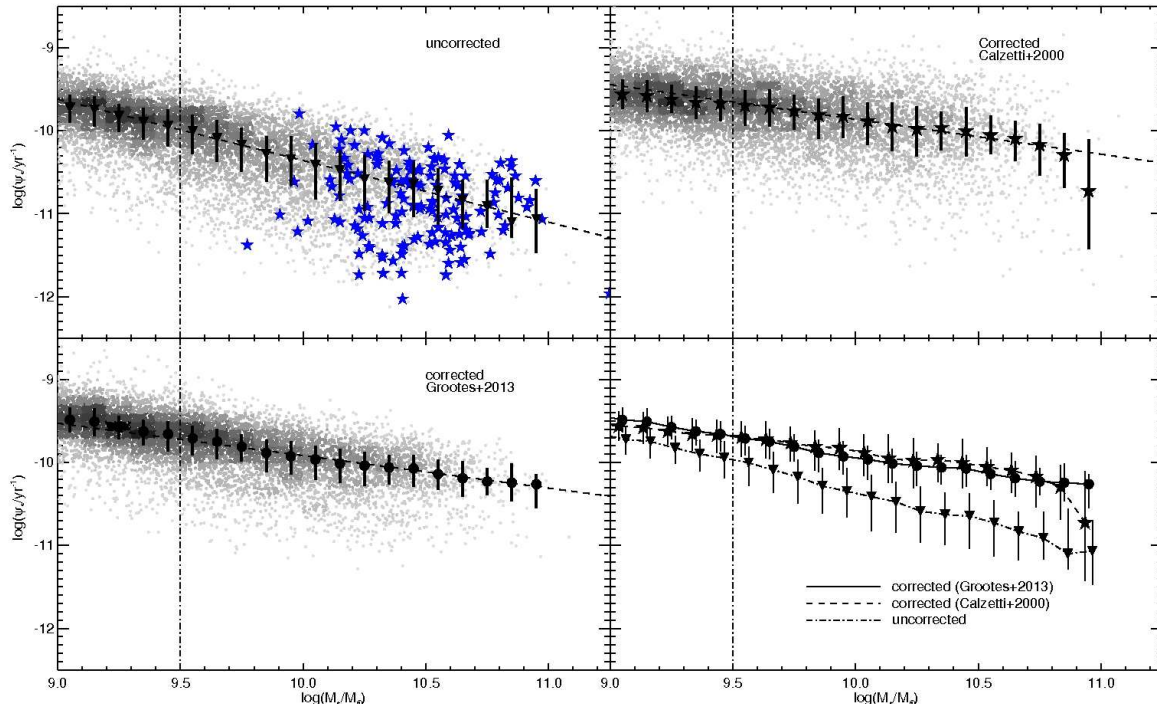


Figure 21. Specific star formation rate ψ_* versus stellar mass M_* for a subsample of spirals galaxies drawn from the *OPTICAL* sample using the cell-based method and the parameter combination $(\log(n), \log(r_e), M_i)$ with $z \leq 0.05$, NUV detections and H α and H β fluxes at $> 3\sigma$, not hosting an AGN. The linear grayscale indicates the relative galaxy density in the $\psi_* - M_*$ plane at the position of the galaxy. The same scale has been applied to all panels. The vertical dashed-dotted line indicates the stellar mass limit above which the sample can be considered complete. The sources are binned in bins of equal size in M_* , with the bars showing the interquartile range and the filled symbols (stars, inverted triangles and circles) showing the median value of ψ_* in each bin. The dashed line in the top panels and the bottom left panel shows a single power-law fit to the binwise median values in the mass range $10^{9.5} M_\odot \leq M_* \leq 10^{11} M_\odot$. The bottom right panel shows the median relations to facilitate comparison. The uncorrected relation is shown as inverted triangles and a dash-dotted line. The relation corrected for dust attenuation following Grootes et al. (2013) is shown as circles and a solid line, while the relation corrected for dust attenuation following Calzetti et al. (2000) is shown as stars and a dashed line. The bin centers have been offset by 0.01 in $\log(M_*)$ for improved legibility. The scatter in the relation due to the scatter in the NUV is significantly reduced for the corrections based on the radiation transfer model, while the Balmer decrement based corrections have no discernible effect on the scatter. In both cases the intrinsic values of ψ_* are shifted upwards w.r.t. the uncorrected values. Spiral galaxies fulfilling the criteria of the sample but hosting an AGN have been overplotted as blue stars in the top left panel.

algorithmic classification approach using support vector machines presented by Huertas-Company et al. (2011) in selecting pure and complete samples of spirals from faint galaxy surveys.

The optimum combinations for use with the method may vary according to the science application for which the sample is being constructed. For application to optically defined galaxy samples comparable in depth or deeper than SDSS we identify the combinations $(\log(n), \log(r_e), \log(\mu_*))$, $(\log(n), \log(r_e), M_i)$, and $(\log(n), \log(M_*), \log(\mu_*))$ to be the most efficient in selecting a sample of spirals balanced between purity and completeness.

While using NUV data can lead to purer samples, it poses the possibility of a bias against UV faint sources and edge-on systems. Furthermore, we caution that making use of UV/optical colours additionally poses stringent requirements on the depths of the samples used in order to provide complete and unbiased samples.

In this paper, we have used the cell-based classification scheme with the parameter combination $(\log(n), \log(r_e), M_i)$ to investigate the specific star-formation rate - stellar mass

$(\psi_* - M_*)$ relation for a purely morphologically defined sample of spiral galaxies. Using this approach which is unbiased in terms of star-formation properties and includes red, quiescent spiral galaxies, we find that the intrinsic, i.e. dust corrected, $\psi_* - M_*$ relation for spiral galaxies can be represented as a single continuous power-law with an index of -0.5 over the mass range $10^{9.5} M_\odot \leq M_* \leq 10^{11} M_\odot$, likely even extending to $10^9 M_\odot \leq M_*$. Despite the inclusion of quiescent galaxies, the relation is also found to be very tight, with a mean interquartile range of 0.4 dex. The lack of a turn-over in the relation over the stellar mass range considered, implies that any mechanism terminating the growth of spiral galaxies beyond this mass range must be accompanied by a rapid morphological transformation.

We supply the cell based division of the parameter space for the combination $(\log(n), \log(r_e), M_i)$, as used in the investigation of the $\psi_* - M_*$ relation, as well as for the combinations $(\log(n), \log(r_e), \log(\mu_*))$ and $(\log(n), \log(M_*), \log(\mu_*))$ in Appendix A, together with a brief instruction on their use.

Immediate future work will focus on using the method presented to test the performance of linear discriminant analysis

using multiple parameters in the morphological classification of galaxies (Robotham et al., in prep.), as well as on defining samples of spirals for use in applications of radiation transfer modelling techniques (Popescu et al. 2011), which critically rely on the existence of the appropriate geometry (in this case spiral disk geometry), to derive self-consistent corrections of the attenuation of UV/optical light by dust in these objects.

ACKNOWLEDGEMENTS

We thank Ted Wyder for his assistance in compiling the sample. Some of the results in this paper have been derived using the HEALPix¹⁵ (Górski et al. 2005) package. Funding for the SDSS and SDSS-II has been provided by the Alfred P. Sloan Foundation, the Participating Institutions, the National Science Foundation, the U.S. Department of Energy, the National Aeronautics and Space Administration, the Japanese Monbukagakusho, the Max Planck Society, and the Higher Education Funding Council for England. The SDSS Web Site is <http://www.sdss.org/>.

The SDSS is managed by the Astrophysical Research Consortium for the Participating Institutions. The Participating Institutions are the American Museum of Natural History, Astrophysical Institute Potsdam, University of Basel, University of Cambridge, Case Western Reserve University, University of Chicago, Drexel University, Fermilab, the Institute for Advanced Study, the Japan Participation Group, Johns Hopkins University, the Joint Institute for Nuclear Astrophysics, the Kavli Institute for Particle Astrophysics and Cosmology, the Korean Scientist Group, the Chinese Academy of Sciences (LAMOST), Los Alamos National Laboratory, the Max-Planck-Institute for Astronomy (MPIA), the Max-Planck-Institute for Astrophysics (MPA), New Mexico State University, Ohio State University, University of Pittsburgh, University of Portsmouth, Princeton University, the United States Naval Observatory, and the University of Washington.

GALEX (Galaxy Evolution Explorer) is a NASA Small Explorer, launched in April 2003. We gratefully acknowledge NASA's support for construction, operation, and science analysis for the GALEX mission, developed in cooperation with the Centre National d'Etudes Spatiales (CNES) of France and the Korean Ministry of Science and Technology.

MWG acknowledges the support of the International Max-Planck Research School in Astronomy and Cosmic Physics Heidelberg (IMPRS-HD) and the Heidelberg Graduate School for Fundamental Physics (HGSFP). We thank the anonymous referee for his/her comments which have helped us improve the paper.

REFERENCES

Abazajian K. N., et al., 2007, *ApJS*, 182, 543
 Abraham R. G., van den Bergh S., Nair P., 2003, *ApJ*, 588, 218
 Adelman-McCarthy J. K., et al., 2006, *ApJS*, 162, 38

Baldry I. K., Glazebrook K., Brinkmann J., Ivezić Ž., Lupton R. H., Nichol R. C., Szalay A. S., 2004, *ApJ*, 600, 681
 Balogh M. L., et al., 2004, *ApJ*, 615, L101
 Bamford S., et al., 2009, *MNRAS*, 393, 1324
 Banerji M., et al., 2010, *MNRAS*, 406, 342
 Barden M., et al., 2005, *ApJ*, 635, 959
 Bell E., de Jong R. S., 2001, *ApJ*, 550, 212
 Bell E., et al., 2004, *ApJ*, 600, L11
 Bernardi M., et al., 2012, *MNRAS*, in press, arXiv:1211.6122
 Bertin E., Arnouts S., 1996, *A&AS*, 112, 393
 Blanton M. R., et al., 2003, *ApJ*, 594, 186
 Blanton M., Roweis S., 2007, *AJ*, 133, 734
 Bournaud F., Jog C. J., Combes F., 2007, *A&A*, 476, 1179
 Brinchmann J., et al., *MNRAS*, 2004, 351, 1151
 Calzetti D., et al., 2000, *ApJ*, 533, 682
 Chabrier G., 2003, *PASP*, 115, 763
 Conselice C. J., 2003, *ApJS*, 147, 1
 de Jong J. T. A., Verdoes Kleijn G. A., Kuijken K. H., Valentijn E. A., 2012, *ExA*, in press, arXiv:1206.1254
 de Vaucouleurs G., 1964, *AnAp*, 11, 247
 Driver S. P., Popescu C. C., Tuffs R. J., Liske J., Graham A. W., Allen P. D., de Propris R., 2007, *MNRAS*, 379, 1022
 Driver S. P., et al., 2011, *MNRAS*, 413, 971
 Driver S. P., et al., 2012, *MNRAS*, 427, 3244
 Einasto M., et al., 2010, *A&A*, 522, 92
 Elbaz D., et al., 2007, *A&A*, 468, 33
 Gini C., 1912, reprinted in *Memorie di Metodologia Statistica*. ed. E. Pizetti & T. Salvemini (1955; Rome: Libreria Eredi Virigilio Veschi)
 Górski K. M., et al., 2005, *ApJ*, 622, 759
 Graham A. W., Driver S. P., Petrosian V., Conselice C. J., Bershady M. A., Crawford S. M., Goto T., 2005, *AJ*, 130, 1535
 Grootes M. W., et al., 2013, *ApJ*, 766, 59
 Hopkins A. M., McClure-Griffiths N. M., Gaensler B. M., 2008, *ApJ*, 682, L13
 Hubble E. P., 1926, *ApJ*, 64, 321
 Huertas-Company M., Rouan D., Tasca L., Soucail G., Le Fèvre O., 2008, *A&A*, 478, 971
 Huertas-Company M., Aguerri J. A. L., Bernardi M., Mei S., Sánchez Almeida J., 2011, *A&A*, 525, 157
 Jogee S., et al., 2004, *ApJ*, 615, L105
 Kauffmann G., et al., 2003, *MNRAS*, 341, 54
 Keller S. C., et al., 2007, *PASA*, 24, 1
 Kelvin L. S., et al., 2012, *MNRAS*, 421, 1007
 Kennicutt R. C., 1998, *ARA&A*, 36, 189
 Kewley L. J., Groves B., Kauffmann G., Heckman T., 2006, *MNRAS*, 372, 961
 Laureijs R., et al., 2011, arXiv:1110.2193v1
 Lintott C. J., et al., 2008, *MNRAS*, 389, 1179
 Lintott C. J., et al., 2011, *MNRAS*, 410, 166
 Lotz J. M., Primack J., Madau P., 2004, *AJ*, 128, 163
 Martin D. C., et al., 2005, *ApJL*, 619, L1
 Morrissey P., et al., 2007, *ApJS*, 173, 682
 Morgan W. W., Keenan P. C., 1973, *ARA&A*, 11, 29
 Misiriotis, A., Popescu, C.C., Tuffs, R.J., & Kylafis, N.D. 2001, *A&A*, 372, 775
 Möllenhoff C., Popescu C. C., Tuffs R. J., 2006, *A&A*, 456, 941
 Moustakas J., et al., 2013, *ApJ*, 767, 50

¹⁵ <http://healpix.jpl.nasa.gov>

Patel S. G., Holden B. D., Kelson D. D., Franx M., van der Wel A., Illingworth G. D., 2012, *ApJ*, 748, L27

Nair P. B., Abraham R. G., 2010, *ApJS*, 186, 427

Nicol M.-H., Meisenheimer K., Wolf C., Tapken C., 2011, *ApJ*, 727, 51

Noeske K. G., et al., 2007, *ApJ*, 660, L43

Pastrav B. A., Popescu C. C., Tuffs R. J., Sansom A., 2013, *A&A*, 553A, 80

Pastrav B. A., Popescu C. C., Tuffs R. J., Sansom A., 2013, *A&A*, 557A, 137

Peng C. Y., Ho L. C., Impey C. D., Rix H.-W., 2002, *AJ*, 124, 266

Peng Y.-j., et al., 2010, *ApJ*, 721, 193

Popescu C. C., Misiriotis A., Kyllafis N. D., Tuffs R. J., Fischera J., 2000, *A&A*, 362, 138

Popescu, C.C., Tuffs, R.J., Kyllafis, N.D., & Madore, B.F. 2004, *A&A* 414, 45

Popescu C. C., Tuffs R. J., Dopita M. A., Fischera J., Kyllafis N. D., Madore B. F., 2011, *A&A*, 527, 109

Ravindranath S., et al., 2004, *ApJ*, 604, L9

Robotham A. S. G., Driver S. P., 2011, *MNRAS*, 413, 2570

Robotham A. S. G., et al., 2013, *MNRAS*, in press, arXiv:1301.7129

Salim S., et al., 2007, *ApJS*, 173, 267

Salpeter E. E., 1955, *ApJ*, 121, 161

Scarlata C., et al., 2007, *ApJS*, 172, 406

Schegel D. J., Finkbeiner D. P., Davis M., 1998, *ApJ*, 500, 525

Sérsic J.-L. ,1968, *Atlas de Galaxias Australes* (Cordoba: Observatorio Astronomico)

Simard L., et al., 2002, *ApJS*, 142, 1

Simard L., Mendel J. T., Patton D. R., Ellison S. L., McConnell A. W., 2011, *ApJS*, 196, 11

Stoughton C., et al., 2002, *AJ*, 123, 485

Strateva I., et al., 2001, *AJ*, 122, 1861

Taylor E. N., et al., 2011, *MNRAS*, 418, 1587

Tempel E., Saar E., Liivamägi L. J., Tamm A., Einasto J., Einasto M., Müller V., 2011, *A&A*, 529, A53

The DES collaboration, 2005, 2005astro.ph.10346T

Treyer M., et al., 2007, *ApJS*, 173, 256

Tuffs R. J., Popescu C. C., Völk H. J., Kyllafis N. D., Dopita M. A., 2004, *A&A*, 419, 821

Whitaker K. E., van Dokkum P. G., Brammer G., Franx M., 2012, *ApJ*, 754, L29

Wyder T., et al., 2007, *ApJS*, 173, 293

Xilouris, E. M., Byun, Y.I., Kyllafis, N. D., Paleologou, E. V., Papamastorakis, J., 1999, *A&A*, 344, 868

York D. G., et al., 2000, *AJ*, 120, 1579

APPENDIX A: CELL DECOMPOSITIONS OF PARAMETER SPACE

We have found the parameter combinations $(\log(n), \log(r_e), M_i)$, $(\log(n), \log(r_e), \log(\mu_*))$, and $(\log(n), \log(M_*), \log(\mu_*))$ to be most efficient in retrieving a simultaneously pure and complete, largely unbiased sample of spiral galaxies when applied to the optically defined galaxy sample used in this work. In addition to the high values of purity and completeness, these selections require a minimal amount of spectral coverage, hence can readily

be applied to various samples of galaxies.

Tab. A1, A2, & A3 provide the decompositions of the parameter space spanned for the combinations $(\log(n), \log(r_e), M_i)$, $(\log(n), \log(r_e), \log(\mu_*))$, and $(\log(n), \log(M_*), \log(\mu_*))$ respectively. These discretizations have been performed using the entire *OPTICALsample* as a calibration sample to maximize the purity and completeness. The full tables are available in the online version of the paper and in machine readable form from the Vizier Service at the CDS¹⁶. Rather than supply a binary classification into spiral and non-spiral cells we supply the spiral fraction and its relative error for each cell, allowing the reader to adapt the classification to his purposes. We do, however note, that the underlying definition of a reliable spiral ($P_{CS,DB} \geq 0.7$) is fixed.

In addition, we have chosen to provide the elliptical fraction for each cell and its relative error, where ellipticals are, analogously to spirals, defined as sources with $P_{EL,DB} \geq 0.7$

We emphasize, that in using the discretizations supplied, it is essential that the reader ensure that there are not significant systematic shifts in the parameters being used between the data used in this work, and the data of the sample to be classified. An initial comparison can be made using Figs. 3 & 4. Similarly, the random uncertainties on the data should not exceed the highest resolution cell dimensions as listed in the tables provided.

The tables supply the front lower left corner of each cell (axis are oriented in a right-hand system), the lengths of the sides in each dimension, the spiral fraction F_{sp} , its relative error $\Delta F_{sp,rel}$, the elliptical fraction F_{el} , its relative error $\Delta F_{el,rel}$, and the resolution level the cell belongs to (1; 1 division per axis, 2; 4 divisions per axis, 3; 8 divisions per axis, 4; 16 divisions per axis). With this information the entire grid can, if desired, be reconstructed. For classifying galaxies the tables can be used as follows:

- select criteria for being a spiral (or elliptical) cell in terms of F_{sp} and $\Delta F_{sp,rel}$ (respectively F_{el} and $\Delta F_{el,rel}$)
- for each source identify the nearest grid point to its forward lower left
 - assign the values of F_{sp} and $\Delta F_{sp,rel}$ from the corresponding cell to the source in question
 - after completion for all sources select those corresponding to the selection criteria determined

¹⁶ Tab. A1, A2, & A3 are available in machine readable form at the CDS via anonymous ftp to cdsarc.u-strasbg.fr (130.79.128.5) or via <http://cdsarc.u-strasbg.fr/>

resolution	corner coordinates			cell dimensions			Spiral fractions		Elliptical fractions	
	$\log(n)$	$\log(r_e)$	M_i	$d\log(n)$	$d\log(r_e)$	dM_i	F_{sp}	$\Delta F_{\text{sp,rel}}$	F_{el}	$\Delta F_{\text{el,rel}}$
2	0.60750	0.00000	-24.5000	0.30250	0.50000	2.25000	0.00000	1.0000e+06	0.61290	2.9136e-01
2	-0.30000	0.50000	-24.5000	0.30250	0.50000	2.25000	0.70213	1.6059e-01	0.02128	7.1459e-01
2	-0.30000	1.00000	-24.5000	0.30250	0.50000	2.25000	0.96875	2.5201e-01	0.00000	1.0000e+06
2	-0.30000	-0.50000	-22.2500	0.30250	0.50000	2.25000	1.00000	1.4142e+00	0.00000	1.0000e+06
3	0.00250	0.50000	-23.3750	0.15125	0.25000	1.12500	0.22222	4.5134e-01	0.03704	1.0184e+00
3	0.15375	0.50000	-23.3750	0.15125	0.25000	1.12500	0.23333	2.9681e-01	0.08333	4.6547e-01
3	0.30500	0.50000	-23.3750	0.15125	0.25000	1.12500	0.09091	3.3029e-01	0.33636	1.9005e-01
3	0.00250	0.75000	-23.3750	0.15125	0.25000	1.12500	0.74375	1.2105e-01	0.00625	1.0031e+00
4	0.22938	0.87500	-23.3750	0.07563	0.12500	0.56250	0.06000	5.9442e-01	0.74000	2.1686e-01
4	0.15375	0.75000	-22.8125	0.07563	0.12500	0.56250	0.01639	7.1288e-01	0.86885	1.3278e-01
4	0.22938	0.75000	-22.8125	0.07563	0.12500	0.56250	0.02564	5.8471e-01	0.86325	1.3582e-01
4	0.15375	0.87500	-22.8125	0.07563	0.12500	0.56250	0.00000	1.0000e+06	0.86441	1.9120e-01

Table A1. Excerpt of cell grid for the combination $(\log(n), \log(r_e), M_i)$. For cells with a spiral(elliptical) population of 0 the relative error is set to 1e6.

resolution	corner coordinates			cell dimensions			Spiral fractions		Elliptical fractions	
	$\log(n)$	$\log(r_e)$	$\log(\mu_*)$	$d\log(n)$	$d\log(r_e)$	$d\log(\mu_*)$	F_{sp}	$\Delta F_{\text{sp,rel}}$	F_{el}	$\Delta F_{\text{el,rel}}$
2	-0.30000	1.00000	6.25000	0.30250	0.50000	1.25000	0.94805	1.6336e-01	0.00000	1.0000e+06
2	-0.30000	-0.50000	7.50000	0.30250	0.50000	1.25000	0.02703	1.0134e+00	0.13514	4.7647e-01
2	0.00250	-0.50000	7.50000	0.30250	0.50000	1.25000	0.01905	7.1381e-01	0.16190	2.6143e-01
2	0.30500	-0.50000	7.50000	0.30250	0.50000	1.25000	0.00000	1.0000e+06	0.11236	3.3352e-01
3	0.30500	0.50000	6.87500	0.15125	0.25000	0.62500	0.58442	1.8764e-01	0.00000	1.0000e+06
3	0.45625	0.50000	6.87500	0.15125	0.25000	0.62500	0.20000	5.4772e-01	0.05000	1.0247e+00
3	0.30500	0.75000	6.87500	0.15125	0.25000	0.62500	0.77778	1.5936e-01	0.01111	1.0055e+00
3	0.45625	0.75000	6.87500	0.15125	0.25000	0.62500	0.58333	2.7458e-01	0.00000	1.0000e+06
4	0.00250	0.50000	7.18750	0.07563	0.12500	0.31250	0.80000	2.0226e-01	0.00000	1.0000e+06
4	0.07813	0.50000	7.18750	0.07563	0.12500	0.31250	0.66176	1.9217e-01	0.01471	1.0073e+00
4	0.00250	0.62500	7.18750	0.07563	0.12500	0.31250	0.68750	2.2613e-01	0.00000	1.0000e+06
4	0.07813	0.62500	7.18750	0.07563	0.12500	0.31250	0.55556	3.2203e-01	0.00000	1.0000e+06

Table A2. Excerpt of cell grid for the combination $(\log(n), \log(r_e), \log(\mu_*))$. For cells with a spiral(elliptical) population of 0 the relative error is set to 1e6.

This paper has been typeset from a $\text{\TeX}/\text{\LaTeX}$ file prepared by the author.

resolution	corner coordinates			cell dimensions			Spiral fractions		Elliptical fractions	
	$\log(n)$	$\log(M_*)$	$\log(\mu_*)$	$d(\log(n))$	$d\log(M_*)$	$d\log(\mu_*)$	F_{sp}	$\Delta F_{\text{sp,rel}}$	F_{el}	$\Delta F_{\text{el,rel}}$
2	0.30500	7.50000	8.75000	0.30250	1.12500	1.25000	0.00000	1.0000e+06	0.00000	1.0000e+06
2	0.60750	7.50000	8.75000	0.30250	1.12500	1.25000	1.00000	1.4142e+00	0.00000	1.0000e+06
2	-0.30000	8.62500	8.75000	0.30250	1.12500	1.25000	0.00000	1.0000e+06	0.00000	1.0000e+06
2	0.00250	8.62500	8.75000	0.30250	1.12500	1.25000	0.00000	1.0000e+06	0.16129	4.8193e-01
3	0.45625	9.75000	6.25000	0.15125	0.56250	0.62500	0.80000	4.7434e-01	0.00000	1.0000e+06
3	0.60750	9.75000	6.25000	0.15125	0.56250	0.62500	0.87500	5.1755e-01	0.00000	1.0000e+06
3	0.75875	9.75000	6.25000	0.15125	0.56250	0.62500	0.81250	3.7339e-01	0.00000	1.0000e+06
3	-0.30000	10.31250	6.25000	0.15125	0.56250	0.62500	0.00000	1.0000e+06	0.00000	1.0000e+06
4	-0.07313	9.18750	6.87500	0.07563	0.28125	0.31250	0.80000	4.7434e-01	0.00000	1.0000e+06
4	-0.14875	9.46875	6.87500	0.07563	0.28125	0.31250	0.80000	2.7386e-01	0.00000	1.0000e+06
4	-0.07313	9.46875	6.87500	0.07563	0.28125	0.31250	0.89286	2.7516e-01	0.00000	1.0000e+06
4	-0.14875	9.18750	7.18750	0.07563	0.28125	0.31250	0.94444	3.3820e-01	0.00000	1.0000e+06

Table A3. Excerpt of cell grid for the combination $(\log(n), \log(M_*), \log(\mu_*))$. For cells with a spiral(elliptical) population of 0 the relative error is set to 1e6.